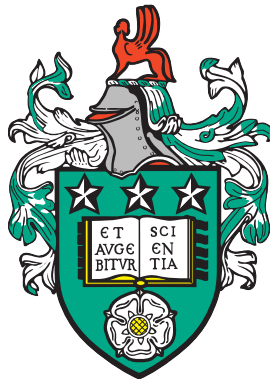# Comparison of Spin Hall Magnetoresistance Temperature Dependence in YIG/Metal Systems

Scott Robert Marmion

School of Physics and Astronomy
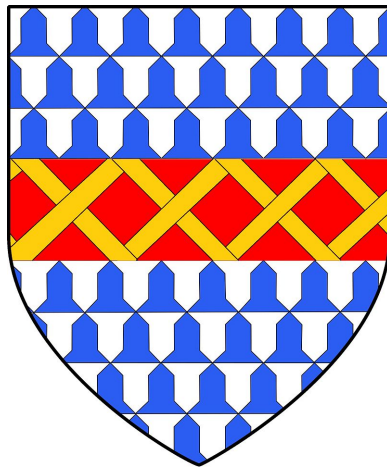
University of Leeds

Submitted in accordance with the requirements for the degree of

Doctor of Philosophy

February 2016

For Dad

Intellectual Property Statement

The candidate confirms that the work submitted is his/her own, except where work which has formed part of jointly authored publications has been included. The contribution of the candidate and the other authors to this work has been explicitly indicated below. The candidate confirms that appropriate credit has been given within the thesis where reference has been made to the work of others.

This copy has been supplied on the understanding that it is copyright material and that no quotation from the thesis may be published without proper acknowledgement.

The right of Scott Marmion to be identified as Author of this work has been asserted by him in accordance with the Copyright, Designs and Patents Act 1988.

Work from the following jointly authored publication is presented in chapter 5:

S. R. Marmion, M. Ali, M. McLaren, D. A. Williams and B. J. Hickey. Temperature dependence of spin Hall magnetoresistance in thin YIG/Pt films, Physical review B, Rapid communications, Vol 89, 2014. **Work attributable to candidate:** Sample growth, measurements, data processing and manuscript preparation. **Work attributable to others:** Matthew McLaren carried out the TEM work. Professor Bryan Hickey, Dr David

Acknowledgements

Abstract

The spin Hall magnetoresistance (SHMR) is a recently discovered effect that occurs in a normal metal (NM) that is in contact with a magnetic material. An insulating magnetic material is ideal as it prevents other magnetic effects by confining the electrons to the NM. To study this a new method for making yttrium iron garnet (YIG) has been developed using sputtering techniques so that devices are quicker and cheaper to produce than by existing liquid phase epitaxy (LPE). The YIG material magnetic properties were extensively characterised up to 280 nm thick. The magnetisation drops below the bulk value in thin samples believed to be caused by a contaminated layer at the substrate interface. As the SHMR is an interface effect the roughness of the films is important and was investigated by X ray reflectivity (XRR) and atomic force microscopy (AFM). The crystal structure was investigated using transmission electron microscopy (TEM). The SHMR is also significantly improved by a factor of 3 after treating YIG with piranha acid before metals are deposited on top.

For SHMR measurements platinum was used first and provided similar results to what is found in the literature. The angular dependence has been measured in a cryostat using four probe resistance measurements with a split pair magnet that allows the sample to be rotated in any direction relative to the applied field. This shows excellent agreement with the theory and was studied for the temperature range of 1.5 K - 300 K. This data has then been fitted using various models for the spin diffusion length and the conclusion reached is that a variation of the Elliot-Yafet mechanism (EY) is the most likely explanation for the observed temperature dependence. The same effect was found to occur in tungsten but with the important difference that it has a negative temperature coefficient of resistivity. This has been successfully fitted with the same spin relaxation models as the platinum. The tungsten is not believed to be in the beta phase, something which if achieved in further work could allow the size of the effect be improved by an order of magnitude up to several percent and so potentially allow the effect to have applications in a device.

Abbreviations

AC	Alternating Current	AFM	Atomic Force Microscopy
AMR	Anisotropic Magnetoresistance	DC	Direct Current
DP	D'yakonov-Perel	EY	Energy Dispersive X-ray Spectroscopy
EY	Elliot-Yafet	FIB	Focused Ion Beam
FM	Ferromagnet	FMR	Ferromagnetic Resonance
FWHM	Full Width Half Maximum	GGG	Gadolinium Gallium Garnet
HAADF	High Angle Annular Dark Field	IPA	Isopropyl Alcohol
ISHE	Inverse Spin Hall Effect	LPE	Liquid Phase Epitaxy
MOKE	Magneto-optical Kerr Effect	MR	Magnetoresistance
NM	Normal Metal	PLD	Pulsed Laser Deposition
RF	Radio Frequency	RMS	Root Mean Square
SEM	Scanning Electron Microscope	SHE	Spin Hall Effect
SHMR	Spin Hall Magnetoresistance	SQUID	Superconducting Quantum Interference Device
SSE	Spin Seebeck Effect	STEM	Scanning Transmission Electron Microcopy
TEM	Transmission Electron Microscopy	UHV	Ultra High Vacuum
VSM	Vibrating Sample Magnetometer	VTI	Variable Temperature Insert
XRD	X-ray Diffraction	XRR	X-ray reflectivity
YAG	Yttrium Aluminium Garnet	YIG	Yttrium Iron Garnet

Common Symbols

B Applied Magnetic Field ($\mu_0 H$)

M Magnetisation

G Spin Mixing Conductance

D Diffusion Constant

d Thickness

θ_{sh} Spin Hall Angle

λ Spin Diffusion Length

e Elementary Charge

m_e Electron Mass

h Planck's Constant

$\hbar$ $h/2\pi$

ρ Resistivity

σ Conductivity

T Temperature

j_s Spin Current

τ_{sf} Spin Relaxation Time

τ_p Momentum Relaxation Time

CONTENTS

CHAPTER 1

Introduction

Spintronics is an active research area of solid state physics that incorporates both the spin and charge of electrons. This is primarily aimed at developing the next generation of computing technology with enhanced speed and efficiency over current hardware. The first electronic computer was designed and build by Thomas Flowers to aid in cryptanalysis during the second world war [1; 2]. This machine, Colossus, used thermionic valves that could be programmed to perform basic logic operations. These valves were subsequently replaced by the first solid state devices, such as the transistor, enabling devices to become smaller and more powerful. The digital revolution that followed continued to develop charge carrier based devices until the 1980s when the first major discoveries were made that involved the spin of the electron signalling the next phase of evolution in electronics. In 1985 it was observed that spin polarised electrons could be injected into a normal metal by passing a charge current through a magnetic material that enabled the spin polarised current itself to be studied more directly [3]. An important effect attributed to spin known as giant magnetoresistance (GMR) was independently discovered by two different groups that soon found widespread applications in the form of spin valves [4; 5]. This effect was widely used in devices such as random access memory (MRAM) and to make read heads for hard disc drives, the result of which has been an exponential increase in electronic data storage capacity. This has now been expanded on to make magnetic tunnel junctions where electrons can tunnel across a thin insulating barrier between two FM layers.

Spin is an intrinsic angular momentum of a fixed quantity possessed by many quantum particles including the electron. Where there is a quantisation axis this momentum has two possible states defined as spin up and spin down. Coupled with the electrons charge this angular momentum provides a magnetic moment that is approximately equal to one Bohr magneton defined by equation 1.1.

$$\mu_B = \frac{e\hbar}{2m_e} \tag{1.1}$$

A spin current is any process by which there is a net change in the spatial distribution of the spin orientation for a group of electrons. This results in a net flow of angular momentum but without the need for a net flow of charge current and hence no Joule heating that results in energy loss [3; 6–9]. Spin currents can also propagate by

collective excitations in a magnetic lattice known as magnons [10–14]. This is analogous to phonons and similarly magnons are caused by thermal excitation of a spin lattice. These magnons reduce the spontaneous magnetisation of a magnetic material as a function of temperature up to the Curie point where the ordered magnetisation is lost [15; 16].

To create spin currents several methods have been developed. They can be generated using ferromagnetic resonance (FMR) where the spin vector of electrons in a ferromagnet are made to precess around an applied magnetic field. The resulting spin current can then be injected into an adjacent material, a process known as spin pumping [17–19]. This is the spintronic equivalent of a battery. When a charge current is passed through a magnetised material the electrons become spin polarised. As this spin polarised current then moves into a NM the spin polarisation relaxes over a spin diffusion length. This is a local injection of a spin current. In a spin valve the spin polarised current can be injected into another FM material where it interacts by the process of spin torque transfer. This exchanges the spin orientation of the current and FM electrons, even to the extent that the magnetisation of the FM can be reversed without an external field applied [20–24].

Spin currents also occur in materials by the spin Hall effect and anomalous spin Hall effect [25; 26]. This is due to a relativistic effect known as the spin orbit interaction. When an electron moves in the electric field of an atomic nucleus, the spin of the electron couples to an effective magnetic field. This interaction requires a correction to the Dirac equation which is spin dependent and results in spin dependent scattering of the electrons. This can give rise to a transverse spin current which is particularly strong in metals with a high atomic number such as platinum and tungsten. This is not limited to metals however and semiconductors including organic materials can be used as active layers in spin valve devices and also exhibit spin related effects [27–32]. Thermal effects have also been investigated and it has been found that temperature gradients can also produce spin currents. One example of this is the spin Seebeck effect that is part of the growing topic of spin caloritronics [33–39].

A recent addition to the known spin based effects is spin Hall magnetoresistance (SHMR) first reported in 2012 [40]. This new effect has been confirmed showing the effect in platinum but controversy has arisen about how to fit the experimental evidence to the theory [41–46]. The work presented in this thesis has been undertaken to gain further insight into this phenomenon and to model the fundamental parameters of spin transport in the materials used. The results will show that the existing effect has been matched in our experiments and new experiments have been done that has added to our knowledge of the effect. From this data a model for spin transport properties in platinum and tungsten is proposed to explain the effect.

1.1   Thesis layout

An introduction to the basic principles of spintronics is presented in chapter 2 and discusses the current state of this field published in the literature. This provides both the background knowledge that this work aims to contribute towards as well as the necessary science that was used to guide this research. There is a number of known spin transport effects that will be reviewed as well as the methods used to measure them. In particular the main focus is on the concept of spin Hall magnetoresistance and discusses the theoretical model that was developed to explain the effect. Crucially the literature provides a mathematical model that the experimental results could be tested against. The key material, YIG, is fundamental to this work and the reasons why this is the case are discussed and its properties will be presented alongside the current methods used to manufacture it.

The techniques that were used to make the materials and to evaluate the quality of them are then discussed in detail in chapter 3. This takes up a considerable amount of the work presented here and throughout subsequent chapters reflecting the many refinements that were made to the processes based on what these tests showed. The techniques used to evaluate the YIG include X-ray diffraction (XRD), X-ray reflectivity (XRR), vibrating sample magnetometry (VSM), Transmission electron microscopy (TEM) and atomic force microscopy (AFM). Feedback from these led to a pioneering new recipe to make the material to a high quality by using sputtering, something which had previously not been very successful. The SHMR measurement techniques are then

described which combine magnetic and cryogenic apparatus to allow the spin transport properties of metals to be studied over a broad range of temperature.

The results from the tests made on the quality and properties of YIG are presented in chapter 4. This will show the data that determined what the optimum conditions that produce the best material. The results of this will also be compared to YIG methods found in the literature to show the success of the new sputtering method. This section also includes experiments done on the metals that are deposited on top and the results of using different treatments on the YIG material. XRR and XRD measurements are presented that gives information on the thicknesses and crystal structure of the YIG.

In chapter 5 the SHMR results are presented. Here it will focus on the work done in platinum wires that is the main material used for studying the effect. The angular rotations are given showing how it matches with theory before the full temperature dependence is given. Also included is the other transport properties of the platinum in particular the effect of thickness on the resistivity. This is done for the different treatments and thicknesses of platinum and show how the experiments evolved to give the expected size of the effect as a result of the improvements made in the sample preparation. SHMR is also measured in platinum with copper and gold spacers inserted which show further confirmation of the results given in the literature. The data is then fitted with the existing theory using several different assumptions that lead to the conclusions drawn from the experiments. Also there is discussion of the problems and other effects that were important to be aware of that affected the measurements including other MR properties of the platinum.

The most original results of this work are in tungsten presented in chapter 6. This material has not been observed to produce the SHMR by any other research group at the time of this thesis and here we find new results to compare with the platinum data in the previous chapter. In particular the tungsten results are in contrast with the platinum resistivity trends and so the differences are discussed and fitted with the same models. The SHMR temperature dependence is fitted with the same models and the resistivity trends allow a more complete understanding of the spin diffusion length temperature dependence. There are still some issues around the tungsten that need to be resolved

and the data for this is given which demonstrates why there is more work still to be done to fully understand the tungsten results.

Chapter 7 brings together the conclusions that have been drawn about all the different aspects of the work from the different results section. These are then critically discussed and compared to conclusions drawn by other groups. The results are still open to some interpretation and so the reasons for this are discussed and suggestions for future work are made. In particular the tungsten data needs more research and opens he possibility not only for a better understanding of the SHMR effect but could also provide the possibility of using it for practical applications.

CHAPTER 2

Theoretical background

2.1 Electrical conductivity

An electric field applied to a conductor causes a charge current to flow that is dependent on the electron mobility. This mobility is subjected to scattering events that can come from several sources. Defects and impurities in a metal are the main source of resistivity at low temperatures as these cause scattering events and give rise to the finite resistivity at 0 K known as the residual resistivity. At higher temperatures electron-electron and electron-phonon scattering add to the residual resistivity. These extra sources of scattering events reduce the mean free path of the electrons. For a NM the resistivity can be generalised to the following form in equation 2.1.

$$\rho = \rho_0 + \alpha T \tag{2.1}$$

As one of the spatial dimensions of a material is reduced, the mean free path of the electron becomes shortened. This can be modelled using the Fuchs-Sondheimer relation approximated numerically by equation 2.2 [47];

$$\frac{\rho}{\rho_0} = 1 + \frac{3}{8}\frac{l_0}{d}(1 - p) \tag{2.2}$$

where ρ_0 is the bulk resistivity, d is the film thickness, l_0 is the electron mean free path in the bulk. A specularity parameter p is included that models the direction the electrons scatter from the surface.

For a disordered metal there are other effects to be considered. The lack of any long range order reduces the charge carrier mobility significantly as well as increasing the residual resistivity significantly [48]. Strong impurities and defects can also result in Anderson localisation. Quantum mechanical treatment of conduction electrons are based on the overlapping of different conduction paths for an electron and a high degree of disorder gives rise interference effects that produce self intersecting paths. When this occurs an electron can be confined to a local region of the material travelling in a circular pattern resulting in a positive correction to the resistivity. The resistivity trends can be used to determine the momentum scattering time temperature dependence. From this we can select an appropriate model for the spin diffusion length.

2.2 Spin currents

A spin current is a phenomenon that is based on the spatial movement of angular momentum. The angular momentum arises from the spin of the electron. This is the fundamental property that takes a similar role as the charge in an electrical current. The definition of a charge current, $\mathbf{j_c}$, is based on the principle of charge conservation. For any system where charge cannot be created or destroyed the charge current density can be written in relation to the time derivative of charge density ρ_q. This law is called the continuity equation of charge given by equation 2.3 [49].

$$\dot{\rho}_q = -\nabla \cdot \mathbf{j_c} \tag{2.3}$$

For a spin current it is angular momentum that takes the analogous role of charge. For many quantum particles including electrons there is an intrinsic angular momentum in addition to its orbital angular momentum. This intrinsic angular momentum of an electron is referred to as its spin. Unlike charge however, spin is not a conserved quantity. Spin can be generated by magnetic processes and are also lost by the process of spin relaxation. Because of this the definition of a spin current needs to be modified to take account of this non-conservation given by equation 2.4 [6].

$$\frac{d\mathbf{M}}{dt} = -\nabla \cdot \mathbf{j_s} + \mathbf{T} \tag{2.4}$$

Here M denotes the magnetisation which is the magnetic moment density from the sum of the electron spins. The spin current density $\mathbf{j_s}$ in this equation provides the definition of a spin current. $\mathbf{T}$ is the relaxation term that can be defined only if the Lagrangian of a system can be defined. Where this is not possible the term can be treated phenomenologically [6]. A basic model for the spin relaxation can be defined by a decay constant τ_{sf} in equation 2.5.

$$\mathbf{T} = -(\mathbf{M} - \mathbf{M_0})/\tau_{sf} \tag{2.5}$$

In a ferromagnet the force acting on conduction electrons is determined by its chemical potential μ which is a spin dependent property. The total angular momentum in a ferromagnet is derived from the sum total of the individual spins that has a finite

value due to the exchange interaction. A spin current can be injected from a ferromagnet into a normal metal by passing a charge current across the interface. The charge current in the FM is spin polarised due to the unequal density of states for the different spin orientations at the Fermi energy. The total charge current is given by the sum of the two spin dependent charge current components $\mathbf{j_c} = j_\uparrow + j_\downarrow$ for up and down spin. The chemical potential and conductivity can then be written in terms of the spin orientation which gives a spin current, $\mathbf{j_s}$, defined by equation 2.6;

$$\mathbf{j_s} = \frac{\hbar}{2e}(j_\uparrow - j_\downarrow) = \frac{\hbar}{2e^2}\nabla(\sigma_\uparrow\mu_\uparrow + \sigma_\downarrow\mu_\downarrow) \tag{2.6}$$

where $\sigma_\uparrow$ ($\sigma_\downarrow$) represents the spin up (spin down) conductivity, and $\mu_\uparrow$ ($\mu_\downarrow$) is the spin up (spin down) chemical potential. The driving force for the charge current is represented by the gradient of the electrochemical potential. The gradient is typically different for the two metals as they have different conductivity and is shown by the dashed line in figure 2.1. As a spin polarised current passes into the NM the chemical potentials for the different spin orientations diverge over a short distance, over which there is spin accumulation in the NM. The spins relax as the NM has a density of states that is spin independent and so the charge current loses its spin polarisation. This is where the non-conservation of spin current occurs over a distance defined by the spin diffusion length.
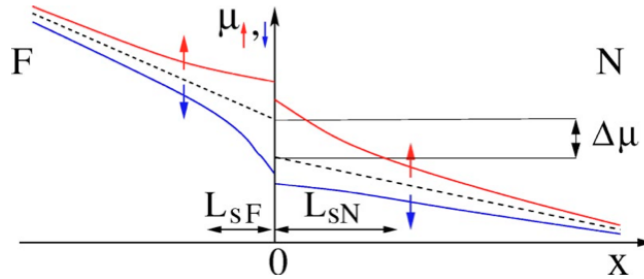
Figure 2.1: Spatial variation of spin dependent chemical potential across a current carrying FM/NM interface. Spin accumulation occurs in the NM due to this spin dependence over a small distance from the interface. Image taken from [50].

The spin polarisation in the FM is represented by the conductivities of the two states being unequal. As the conduction electrons move into the NM the chemical potentials have to be continuous however there can be a small difference in real devices due to

the interface contact resistance. The gap between the dashed line on each side of the interface $\Delta\mu$ is called the spin accumulation voltage representing the loss in potential for the electron as it is no longer in a FM material. In the NM this results in a spin accumulation that dissipates over a length scale that is characterised by L_{sN} called the spin diffusion length. In the FM near the interface the spin current is suppressed due to a back flow of spin polarised electrons induced by the accumulation in the NM also characterised by a spin diffusion length L_{sF}.

2.3 Spin relaxation mechanisms

The spin of an electron is subject to relaxation over a timescale τ_{sf}. The distance the electron travels in this time is the spin diffusion length λ. This length scale is a limiting factor in the use of spintronic devices and so measurement of it is important. It is derived from the spin flip time τ_{sf} and the diffusion constant D. The diffusion of a current is given by the density of electrons, n, and a diffusion constant D in equation 2.7.

$$j_{diffusion} = -eD\nabla n \tag{2.7}$$

The diffusion constant is related to the momentum scattering time τ_p by the relation in equation 2.8 [50].

$$D \propto \tau_p \tag{2.8}$$

The final expression for the spin diffusion length is determined by the product of the diffusion constant and the spin relaxation time in equation 2.9.

$$\lambda = \sqrt{D\tau_{sf}} \tag{2.9}$$

To determine how the spin diffusion length behaves it is necessary to determine how the spin relaxation time varies in relation to the momentum scattering time. For this several mechanisms have been proposed and will now be discussed.

2.3.1 Elliot-Yafet

The first idea that conduction electron spins can relax due to to momentum scattering was proposed by Elliot in 1954 [51]. The lattice ions in a metal induce spin-orbit coupling in the conduction electron wave function with a periodic Bloch state potential that can be written as equation 2.10;

$$\mathbf{V}_{so} = \frac{\hbar}{4m^2c2} \nabla \mathbf{V_{sc}} \times \hat{\mathbf{p}} \cdot \hat{\sigma} \tag{2.10}$$

where $\mathbf{V_{sc}}$ is the scalar periodic lattice potential, $\hat{\mathbf{p}}$ is the linear momentum operator and $\hat{\sigma}$ are the Pauli matrices [50]. Single electron wave functions now become a mixture of Pauli spin-up and spin-down states. As a result the combination of spin-orbit coupling and momentum scattering results in spin relaxation. A further modification to this was made by Yafet to take phonons into account to give the full Elliot-Yafet mechanism [52]. From this model the momentum scattering time, τ_p is proportional to the spin relaxation time τ_s in equation 2.11.

$$\tau_s \propto \tau_p \tag{2.11}$$

As the resistivity of a material is based on the momentum scattering time this gives a prediction of the behaviour for the spin diffusion length as a function of temperature. For a NM the Elliot-Yafet mechanism gives a spin diffusion length inversely proportional to temperature given by equation 2.12.

$$\lambda \propto \frac{1}{T} \tag{2.12}$$

An illustration of this mechanism in action is shown on the left in figure 2.2. In any given system there can be many different contributions to the spin relaxation and so the Elliot-Yafet theory applies to a material where the relaxation is dominated by one cause.

2.3.2 D'akanov Perel

An alternative mechanism of spin relaxation was developed for materials with a lack of Rashba type inversion symmetry [54; 55]. The lack of inversion symmetry comes from momentum spin states that are not degenerate. This mechanism is most commonly
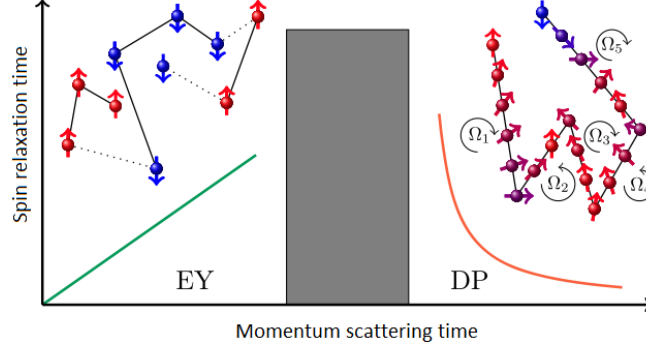
Figure 2.2: Illustration of EY and DP spin relaxation mechanisms with different relations between momentum and spin relaxation time. Taken from [53].

found in semiconductors where two distinct atoms in the Bravais lattice breaks the inversion symmetry. This spin splitting can be described by an intrinsic **k**-dependent magnetic field around which the electron spin precesses. This field is derived from spin-orbit coupling in the band structure and the spin precesses with a Larmor frequency, $\Omega(\mathbf{k})$. The Hamiltonian for this is given by equation 2.13.

$$H(\mathbf{k}) = \frac{1}{2}\hbar\sigma \cdot \mathbf{\Omega}(\mathbf{k}) \tag{2.13}$$

The momentum scattering and momentum dependent scattering lead to spin dephasing. The spin relaxation occurs when the electron is travelling between scattering events as pictured on the right of figure 2.2. The mechanism becomes more effective as the time between scattering events increases. The more frequently it scatters, the less time it spends travelling in any one direction hence the less time it has to dephase resulting in a longer spin relaxation time. The relation between the spin relaxation time and momentum scattering is thus given by equation 2.14 [50].

$$\frac{1}{\tau_s} = \mathbf{\Omega}^2(\mathbf{k})\tau_{sf} \tag{2.14}$$

The most important difference between the EY and the DP mechanisms is their opposite dependence on the momentum scattering time. Strong scattering makes the EY mechanism more effective and the DP processes less effective. This due to the fact that in the EY process the loss of phase occurs only during a collision. In the case of the DP process, spin phases are randomised between collisions, since electrons precess

with different frequencies depending on their momenta. Experimentally we can make a distinction between the two mechanisms by investigating the dependence of their spin diffusion lengths on resistivity. Since the diffusion constant is proportional to τ_p, for the DP mechanism this cancels with the dependence of spin relaxation time. For a degenerate electron system this means that the spin diffusion length should be a constant that is independent of resistivity.

Two other mechanisms have been described but are not relevant to the work in this thesis [50]. The Bir-Aronov-Pikus mechanism is a theory that applies to semiconductors due to its dependence on electron-hole pairs [56]. The other is the Hyperfine-interaction mechanism that is related to the DP mechanism by spin dephasing and is found in quantum dot systems. It has been established that this interaction is too weak to cause effective spin relaxation in metals due to the itinerant nature of the electrons [57].

2.4 Exchange spin current

Spin currents can also be carried in the form of spin waves where neighbouring spins are coupled together and move collectively. In a magnetic material the exchange interaction couples the spin on neighbouring electrons to each other in the same direction that gives rise to the net magnetic moment. This is given by equation 2.15 where the exchange integral J is derived from the overlap of the wave functions of the electrons. The sign if the exchange integral determines wether the coupling between spins are ferromagnetic or antiferromagnetic.

$$E_i = -2J \sum_j \mathbf{s_i} \cdot \mathbf{s_j} \tag{2.15}$$

To understand how a spin current can be carried in an ordered magnetic system we first consider how an individual electron interacts with an applied magnetic field. The magnetic moment of the electron experiences a torque that tries to align it with the direction of the applied field. However as the magnetic moment is created because of the electrons angular momentum the torque causes the moment to precess around the

direction of the applied field in the same manner as a rotating object being acted upon by gravity. This is given by the Landau-Lifshitz equation 2.16 where the time derivative of the magnetisation vector is related to the applied field H and the gyromagnetic ratio γ.

$$\frac{d\mathbf{M}}{dt} = -\gamma\mathbf{M} \times \mathbf{H} \tag{2.16}$$

The angular frequency of the precession is given by the product of the gyromagnetic ratio and the applied field. The moment of the electron is subjected to a damping effect that allows it to relax into its state of lowest energy parallel to the applied field. This is due to interacting with environmental degrees of freedom and lattice vibrations that transfer angular momentum. This relaxation is accounted for by adding the Gilbert term to give the Landau-Lifshitz-Gilbert equation 2.17.

$$\frac{d\mathbf{M}}{dt} = -\gamma\mathbf{M} \times \mathbf{H} + \frac{\alpha}{M}\mathbf{M} \times \frac{d\mathbf{M}}{dt} \tag{2.17}$$

Here α is the Gilbert damping parameter which is found to be very low (-10^{-4}) in YIG allowing spin to be transported over long distances ($>$1mm) [58; 59]. As the spins in a ferromagnet are coupled together by exchange interaction, a disruption to one spin is able to create a wave with the nearby spins in a manner similar to a spring. These can be generated as a result of thermal energy or induced by absorption of microwaves in FMR. For the exchange spin current, collective excitations of the electrons gives rise to a spin wave that carries angular momentum as illustrated in figure 2.3.
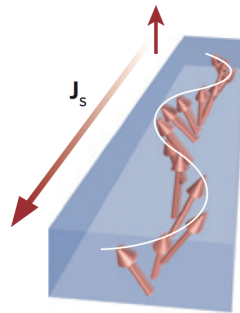

Figure 2.3: Illustration of the collective propagation of exchange coupled spins known as a spin wave. This is the type of spin current found in magnetic insulators. Taken from [60].

It is thermally generated spin waves, known as magnons, that explain the reduction in the saturation magnetisation of a material at finite temperatures as the magnetic order is disrupted. These spin waves can be used to inject a spin current into a normal metal by spin pumping, even when the magnetic material is an insulator like YIG. Spin pumping is the spintronic equivalent of a battery from conventional electronics. The angular momentum carried by a spin wave crosses into a NM where spin accumulation is induced by spin transfer torque. This accumulation is then subject to spin relaxation as has been previously discussed. Injecting a spin current in this manner across a FM/NM interface requires the introduction of a complex spin pumping conductance $A_{\uparrow\downarrow}$. This is the difference between the transmitted ($g_{\uparrow\downarrow}^t$) and reflected ($g_{\uparrow\downarrow}^r$) spin mixing conductances given by equation 2.18 [61; 62].

$$A_{\uparrow\downarrow} = g_{\uparrow\downarrow}^t - g_{\uparrow\downarrow}^r \tag{2.18}$$

These describe the spin current that is transmitted into and reflected back from the normal metal and are related to the contact area. The spin mixing conductance ($G_{\uparrow\downarrow}$) is more generally quoted after being multiplied by the quantum conductance given by equation 2.19.

$$G_{\uparrow\downarrow} = \frac{e^2}{h} g_{\uparrow\downarrow} \tag{2.19}$$

The units of $G_{\uparrow\downarrow}$ are $\Omega^{-1}\mathrm{m}^{-2}$ which is strictly a conductance per unit area however we will keep with the convention in the literature and call this the spin mixing conductance with the symbol G from now. For a magnetic insulator the spin mixing conductance represents the absorption of spin polarisation in a NM by spin torque transfer as conduction electrons cannot pass into the YIG [40].

2.5 Spin Hall effect

The spin Hall effect is a transport property that deflects an electron depending on its spin orientation [26; 54; 55]. This results in spin accumulation at opposing surfaces of a current carrying sample analogous to the classical Hall effect. No magnetic field is needed for the effect and the direction of the spin current is transverse to the direction of the charge current as illustrated in figure 2.4.
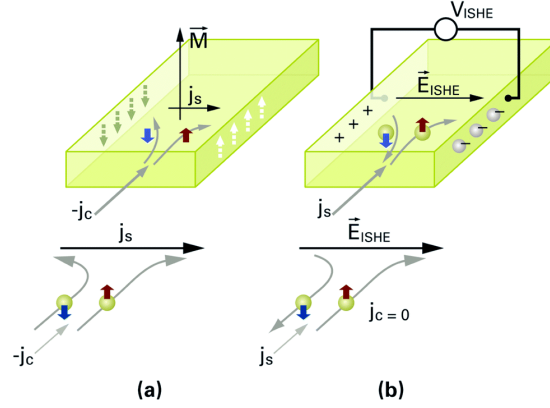
Figure 2.4: Illustration of the spin Hall effect (a), and inverse spin Hall effect (b). The spin current is always transverse to the charge current direction resulting in spin accumulation (a) or charge accumulation (b). Taken from [63].

The motion can be understood intuitively by comparing the SHE to the Magnus effect. This causes a transverse deviation in the flight of an object such as a tennis ball depending on the rotation direction interacting with the air it is travelling through. In the case of the SHE it is the spin orientation that determines the direction of scattering and therefore provides a means of creating a spin current. This spin current can also be controlled as the spin current is proportional to the charge current. It was first observed in semiconductors and subsequently in metals that exhibit high spin-orbit coupling [64; 65]. The concept of the asymmetric splitting of charge carriers is due to relativistic spin-orbit coupling [66]. The measure of this effect is given by the spin Hall angle in equation 2.20. This is the ratio of the spin conductivity, σ_{xy}, and the electrical conductivity σ_{xx}. The subscripts denote the direction of the two currents.

$$\theta_{sh} = \frac{\sigma_{xy}}{\sigma_{xx}} \tag{2.20}$$

There are different mechanisms for the scattering of the electrons based on the spin-orbit coupling that are now discussed. The spin Hall conductivity is determined by the sum of the contributions due to these mechanisms in equation 2.21. The intrinsic mechanism is based on the band structure of a material while the extrinsic mechanisms are additional contributions due to defects and impurities in the material.

$$\sigma_{xy} = \sigma_{xy}^{int} + \sigma_{xy}^{sk} + \sigma_{xy}^{sj} \tag{2.21}$$

2.5.1 Intrinsic mechanism

As an electron passes through a material it can be deflected when it encounters an atomic nucleus. The scattering is based on spin-orbit coupling between the orientation of the electron spin and the orbital angular momentum of the atom. The resulting momentum transfer scatters the electron in a direction that has a component perpendicular to the direction of the incoming electron. The up spins are scattered with higher probability in the opposite direction to down spins. The result of this is a net spin current perpendicular to the charge current. Movement of the spins also causes spin accumulation at the surfaces of the material which can be injected into another at an interface. The intrinsic spin Hall effect occurs in a material that has no defects or impurities [67; 68]. From the Dirac equation the spin-orbit interaction can be modelled as a correction to the Pauli equation of the form in equation 2.22;

$$\mathbf{H_{SO}} = \eta_{so}\sigma \cdot [\mathbf{k} \times \nabla\mathbf{V_{vac}}(\mathbf{r})] \tag{2.22}$$

where $\eta_{so} = (\hbar/2mc)^2$, k= $p/\hbar$ and $\nabla V_{vac}(\mathbf{r})$ is the potential acting on the electron, m is the mass of the electron and c, the speed of light. The spin-orbit Hamiltonian can be modified for a periodic Bloch potential that represents the atoms in a lattice. The potential due to an electric field can be treated as an effective magnetic field resulting from a relativistic treatment in the reference frame of the electron. The interaction of this can be written as equation 2.23:

$$\mathbf{H_{SO,int}} = -\frac{1}{2}\sigma \cdot \mathbf{B(k)} \tag{2.23}$$

where $\mathbf{B(k)}$ is an effective k-dependent magnetic field for the electron band considered and k is the crystal wavevector. The vector of the Pauli matrices is given by σ. The result of this is a spin dependent perturbation on the conduction electron momentum. As the spin-orbit interaction is influenced by the atomic nuclei the intrinsic spin Hall effect is found to be strong in the heavy elements such as platinum and gold.

2.5.2   Extrinsic mechanisms

When the potential of the periodic atoms is disrupted due to either defects or impurities in a crystal structure. This mechanism is an addition to the intrinsic mechanism that is caused by impurities in a metal [69–72]. This can be written in equation 2.24 as a modification to equation 2.23.

$$\mathbf{H_{SO,ext}} = \bar{\eta_{so}}\sigma \cdot [\mathbf{k} \times \nabla V(\mathbf{r})] \tag{2.24}$$

Here $\bar{\eta_{so}}$ can be much higher than for the intrinsic mechanism. When an electron scatters from an impurity the scattering cross section is dependent on the spin state. As a result a different scattering angle is given for spins up and down. This is known as Mott skew scattering. Where the scattering from an impurity involves a momentum transfer $\delta\mathbf{k}$, the conservation of momentum gives a corresponding change in the electron vector given by equation 2.25:

$$\delta\mathbf{r} = \bar{\eta_{so}}[\delta\mathbf{k} \times \sigma] \tag{2.25}$$

where $\delta\mathbf{r}$ is a shift in a direction perpendicular to the charge current. This is known as the the side jump mechanism. The extrinsic mechanisms have been studied in materials like $Cu_{99.5}Bi_{0.5}$ that has a large spin Hall effect in comparison to copper where the intrinsic mechanism is negligibly small [71]. In this the dominant mechanism responsible for the spin Hall effect comes from large bismuth atoms interacting strongly as current passes through copper that has a low intrinsic spin Hall effect.

2.6   Spin Hall magnetoresistance

2.6.1   Theoretical model of SHMR

The basic device for SHMR experiments consists of a NM like platinum deposited on an FM insulator that has a current passed through it. The insulating nature prevents the charge current from entering the FM that would add additional effects as well as complicating the resistivity change due to just the NM. The basic illustration of the different stages involved in SHMR are shown in figure 2.5.
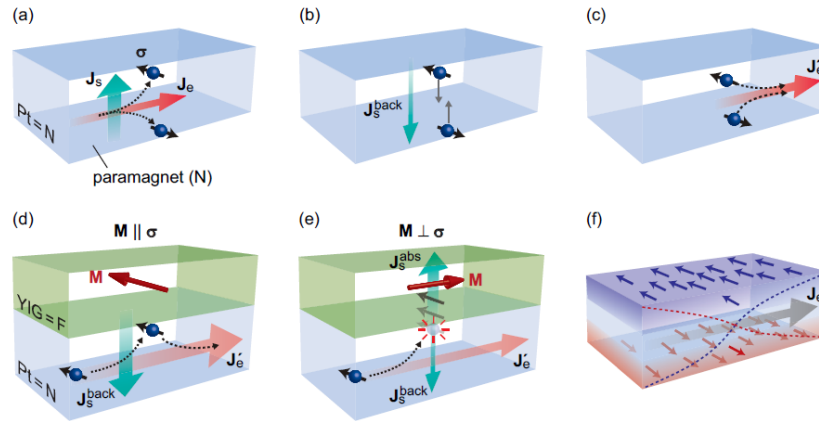
Figure 2.5: Illustration of the SHMR effect shown in stages as a combination of the spin Hall and inverse spin Hall effect. A charge current passing through a metal is subject to the spin Hall effect shown in (a). This deflects electrons perpendicular to the charge current either up or down depending on spin orientation. This spin current in the vertical direction produces a spin polarised metal as shown in (f). As the spin polarised electrons reflect from the metal surfaces and back in the opposite perpendicular direction the Inverse spin Hall effect deflects the electrons, this time in the direction of the charge current (b-c). This results in a momentum change of electrons in the current direction which reduces the resistivity of the NM. If the normal metal has one surface in contact with a magnetic insulator the spin polarised electrons interact with the magnetisation of the FM. When the magnetisation of the FM is aligned parallel or antiparallel to the spin polarisation at the interface the electrons reflect from the interface without spin scattering as indicated in (d). As the magnetisation of the FM is rotated relative to the spin polarisation, the conduction electrons spin interacts with the magnetic moment of the FM and angular momentum is transferred into the FM. The electron in the normal metal is reflected with its spin scattered as show in (e). The net result is that the reflected electrons now get deflected in the opposite direction to the charge current and thus increase the resistivity. Images taken from [40].

To measure the size of the SHMR, resistivity measurements are taken as an applied magnetic field is rotated relative to the direction of the current. The SHMR changes as a function of the angle between the applied field and the electron spin orientation. This is different to many other types of MR where the relevant angle is between the magnetisation and the current direction. This provides a means of distinguishing SHMR from other effects such as AMR. Rotating the magnetisation vector in different orientations are also used to confirm that the effect is not a sum of several different effects with different angular dependence. The angular dependence of the effect is given by equation 2.26 where α is the angle between the magnetisation vector of the FM and the spin polarisation of electrons in the NM.

$$\rho = \rho_0 - \Delta\rho \sin^2 \alpha \tag{2.26}$$

The spin current density is derived from the cross product of the spin accumulation and spin mixing conductance at the NM interface. As both of these quantities are related to the angle of the applied field a $\sin^2$ dependence is predicted.

Theory has been developed that gives the size of the resistivity difference, $\frac{\Delta\rho}{\rho_0}$, given by equation 2.27. This gives a squared dependence on the spin Hall angle, θ_{sh}, as such the effect is expected to be small and so measurements have only been observed in platinum primarily and a small effect has been measured in tantalum. This dependence arises from the spin accumulation and the ISHE both being proportional to the spin Hall angle.

$$\frac{\Delta\rho}{\rho_0} = \theta_{sh}^2 \frac{\lambda}{d} \frac{2\lambda G \tanh^2 \frac{d}{2\lambda}}{\sigma + 2\lambda G \coth \frac{d}{\lambda}} \tag{2.27}$$

Thickness is represented by d and λ is the spin diffusion length. The ratio of these two parameters is the determining factor in where the maximum SHMR resistivity change occurs. This is due to the effect of the spin accumulation and ISHE being limited by the spin diffusion length. For thicknesses considerably beyond this length the ISHE effect no longer contributes to the resistivity. For NM thicknesses below the spin diffusion length the spin accumulation at the interfaces are mixed due to their proximity. G is the spin mixing conductance and σ is the conductivity of the metal. The

comparative size of these are also important for determining the temperature dependence. If the conductivity is sufficiently small in comparison to the rest of the quotient then the spin mixing conductance is effectively cancelled out and so any temperature dependence it may have is not relevant. This is the key equation that the experimental data is to be fitted to in chapter 5 and 6.

2.6.2 Experimental observations of SHMR

The first measurements of the effect were done not by altering the angle but by using magnetic field sweeps. The drawback to this method is that it did not determine the full size of the resistivity change. The incomplete resistivity change does still work however because the magnetic field sweep brings the YIG to saturation. Below which the magnetisation at the interface with the platinum is not in a uniform direction. As the orientation of the magnetisation is not uniform it will not give the same spin scattering as when saturated. Although this does not give the same resistivity change it allows the effect to be compared to the hysteresis loop of the YIG. The saturation points of the magnetisation and the SHMR are found to coincide.

To answer the question about magnetic proximity effects a simple experiment was done. As it is transmitted by exchange interaction, the magnetic proximity is expected to have a short range. This requires the platinum to be in contact with the magnetic material. A copper spacer layer 5 nm thick was grown between the platinum and YIG. This lifts the platinum outside the reach of exchange interaction and so proximity effect is eliminated. Data for this is shown in figure 2.6.

The effect has in the last year been expanded to include several more materials. It has been demonstrated in tungsten, iridium manganese, tantalum and palladium. Palladium is of particular interest as the angular dependence shows that there are in fact two separate effects. All of these works have metals with resistivity that is either not given or follows that of a normal metal. The tungsten data in this thesis is the first that shows the SHMR in a metal that does not follow this trend.
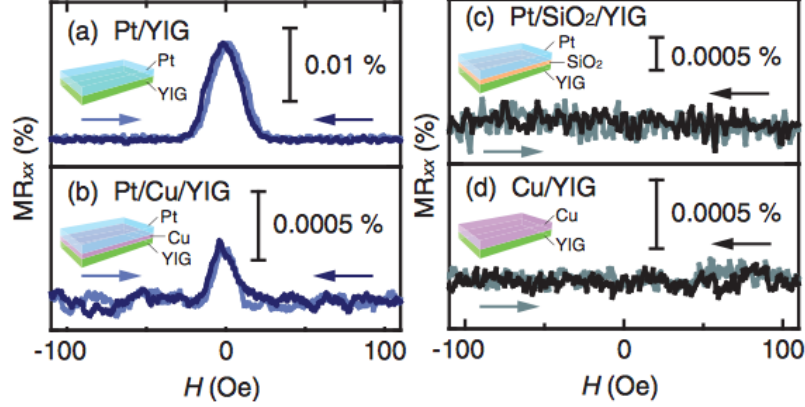
Figure 2.6: Field sweeps showing the SHMR in 12 nm Pt wire with different spacers placed between the metal and YIG. The effect is only present where conduction electrons can reach the YIG interface and not as a result of magnetic proximity. Taken from [40].

2.7   Spin Seebeck effect

The Seebeck effect is a process where a voltage is generated along a conductor that has a temperature gradient across it. This is one of three related aspects of the thermoelectric effect [63]. It has been discovered that a spin voltage can also be generated by a temperature gradient. The effect was first observed in permalloy [36]. One important difference with the SSE is that the effect is also present in insulators [37–39]. This demonstrated that, like SHMR, the spin voltage can be generated by magnons. The effect is measured in two different sample configurations, transverse and longitudinal, as illustrated in figure 2.7.

A spin current generated by a temperature gradient can be detected by injecting it into a material with a large spin Hall angle such as platinum. This spin current produces an electric field in the metal due to the inverse spin Hall effect which can be measured as a voltage given by equation 2.28.

$$\mathbf{E_{ISHE}} = \frac{\theta \rho}{A} (\frac{2e}{\hbar}) \mathbf{J_s} \times \sigma \qquad (2.28)$$

The spin current injected is denoted by $\mathbf{J_s}$, the spin Hall angle given by θ and
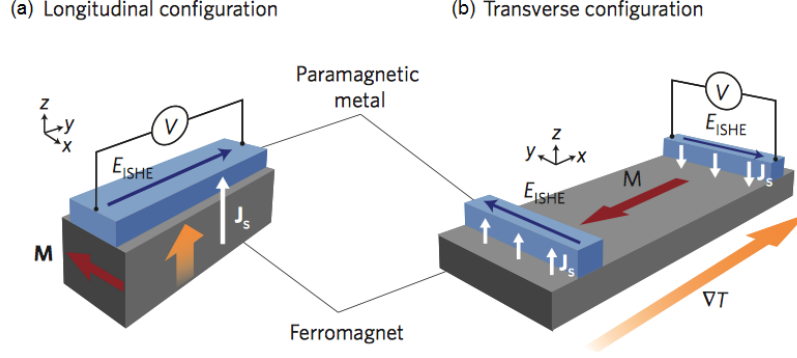
Figure 2.7: Illustration of the spin Seebeck effect in both the longitudinal, (a) and transverse, (b) configuration highlighting the relative orientation of temperature gradient, magnetic field and the resulting electric field. Taken from [63]

the contact area of the metal/YIG interface A. The spin voltage that generates the spin current arises from the difference in the effective magnon temperature T_m^* and the electron temperature T_e^*. These effective temperatures are derived from the fluctuation-dissipation theorem [73–75]. Thermal effects at the interface give rise to fluctuations in the magnetisation. The total spin current given by equation 2.29 is the sum of the fluctuating thermal spin pumping current from FM to NM that is proportional to T_m^* and the Johnson-Nyquist spin current noise from NM to FM which is proportional to T_e^* [6].

$$J_s = 2\alpha^1 k_B (T_m^* - T_e^*) \tag{2.29}$$

Here α^1 represents an effective damping term. The result of this is a thermally induced spin pumping mechanism. The spin current that is injected into the NM then interacts via the inverse spin Hall effect which deflects the electrons in a perpendicular direction. This produces a voltage along the length of the NM which is dependent on the spin current that is injected and the spin Hall angle of the NM. The polarisation of the injected spin is determined by the magnetisation orientation of the FM. As a result the voltage follows a sinusoidal pattern as the magnetisation is rotated. A field sweep gives a voltage that follows the shape of the FM hysteresis loop which confirms that the effect is linked to the YIG and not due to the Nernst-Ettingshausen effect. If this

was the cause then the voltage would vary in proportion to the applied magnetic field and not saturate. This has been researched much more extensively in the longitudinal configuration. YIG is an ideal material to use for this as it eliminates any other conduction effects in the NM. Examples of the transverse SSE data from the literature are shown in figure 2.8.
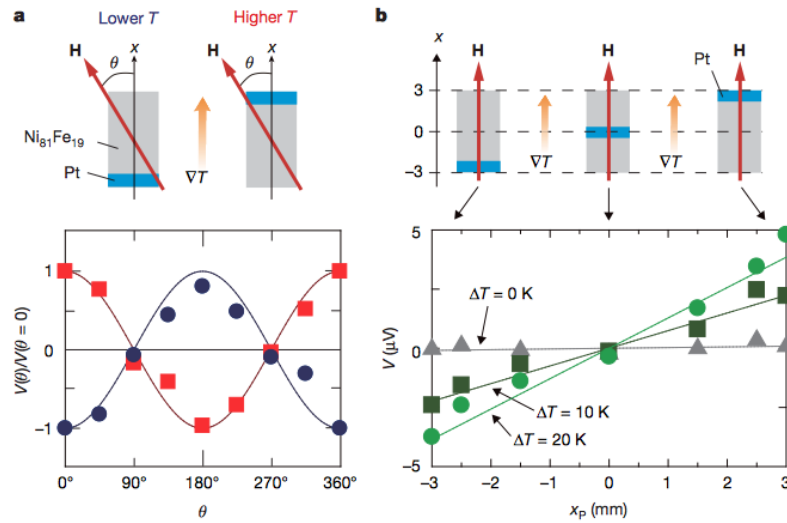
Figure 2.8: Transverse SSE data showing the angular dependency, (a), and as a function of temperature gradient and the position of the wire (b). These results are found to be in agreement with theory. Taken from [76].

2.8 Ferrimagnetic insulators

2.8.1 Garnet crystals

Garnets are a group of minerals which share the same general chemical formula with a range of different elements occupying the different lattice sites. Many of these exist naturally and have been mined since ancient times as gemstones. This continued into modern times and are also used as an abrasive in industry [77; 78]. New garnets can also be made synthetically which have additional useful properties such as magnetism. The garnet structure is shown in figure 2.9 with YIG constituent atoms as an example.

The unit cell is large containing 160 atoms in 3 different sub lattices. The general chemical formula for a garnet is;

$$X_3Y_2(ZO_4)_3$$
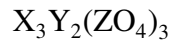
where X,Y and Z can be a range of different elements and O is the oxygen. For YIG the composition is,

$$Y_3Fe_5O_{12}$$

YIG

FeO$_6$ unit   FeO$_4$ YO$_8$
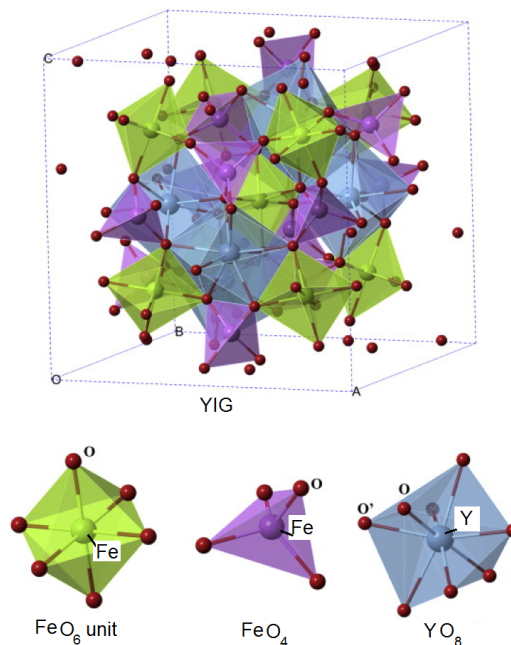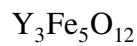
Figure 2.9: Illustration of simple cubic unit cell for the YIG crystal structure. Sub-lattices show the different oxygen bonds to the individual metal ions. The iron has both a tetragonal and octahedral shape and the yttrium is dodecahedral. Images modified from [40].

The unit cell is simple cubic with a lattice constant of 12.376 Å. Inside the unit cell the atomic arrangement is complex as it contains three different types of sub-lattice that lock together. It is the coupling of the iron atoms on the tetragonal and octahedral components that give rise to the materials magnetism.

2.8.2 Magnetic properties

The magnetic property of YIG arises from antiferromagnetic coupling of the iron atoms. This phenomenon is done through the mechanism of superexchange derived from Néel theory [79]. The iron atoms in a garnet structure are separated by a distance greater than a direct exchange interaction can occur. Magnetic coupling is able to reach over a greater distance using an intermediary non-magnetic ion. Instead the superexchange mechanism involves the overlapping of the d orbital wave functions with the p orbitals on the oxygen anions as shown in figure 2.10. This most commonly results in antiferromagnetism and so there would be no net magnetisation. In YIG the different iron sites are not in equal number. For three tetrahedral sites there are two octahedral sites that couple together with opposing moments. This imbalance results in a net magnetic moment known as ferrimagnetism. Each unit cell contains 24 Fe 3+ ions on tetrahedral sites and 16 Fe 3+ ions at the octahedral sites that results in approximately 40 Bohr magnetons per unit cell. As the exchange coupling is transmitted by the overlapping of the wave functions with the oxygen the content in the crystal is vital for magnetisation. Any oxygen depletion or contaminant on the oxygen atom sites will result in the iron moments not being able to couple over a sufficient distance and the magnetisation will be inhibited.
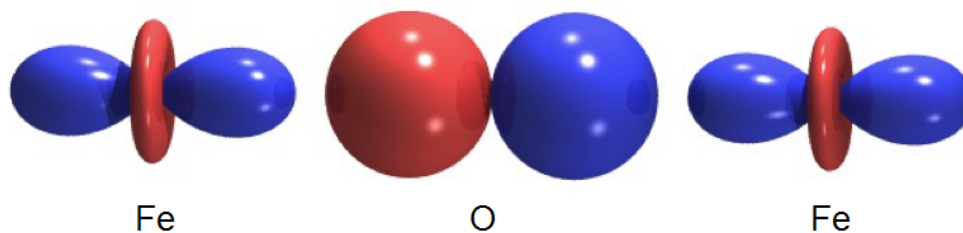

Figure 2.10: Illustration of the wavefunctions in a superexchange mechanism between two iron atoms. The overlapping of the oxygen wave functions leads to coupling between the iron wavefunctions spin orientations. Image taken from [80].

CHAPTER 3

Experimental techniques

3.1 Deposition methods

3.1.1 Substrates

Due to the complex nature of the YIG crystal structure the choice of substrate is important to help the as-sputtered material grow in the correct way. The films can be made epitaxial if the substrate structure and lattice constant matches that of the intended structure of the YIG. It is also important to have a close match between the lattice constants. Differences between the lattice constants induces strain in the films at the interface [81]. The widely accepted choice, both in the literature and in this research, is gadolinium gallium garnet (GGG). GGG has the same garnet crystal structure as YIG with the chemical formula $Gd_3Ga_5O_{12}$ and a lattice constant of 12.383 Å compared to 12.376 Å for YIG [82].

GGG is manufactured by the Czochralski process using a molten flux of the constituent elements and a seed sample [83; 84]. This is similar to how YIG is made by LPE. For consistency the substrates all have the <111> crystal axis pointing out of the plane. The surface is also polished to provide a smooth interface with low surface roughness. This was measured by AFM and found to have an RMS roughness of less than 0.2 nm. The smoothness of the films grown on top is dependent on this. GGG is a strong paramagnet, a property that causes problems for magnetic measurements. The magnetic moments in a thin YIG film are small compared to this large background effect and needs to be subtracted. This becomes very difficult at low temperatures. Paramagnetism follows Curie's law where the magnetisation is inversely proportional to temperature. The moment of a small sample of pure GGG is shown in figure 3.1 indicating the size of the problem. The typical contribution to the total moment of a 100 nm thick YIG film is -10^{-3} EMU. At low temperatures this paramagnetism can produce a signal large enough to overload the lock in amplifier preventing data from being taken. Thermal stability is also critical in this low temperature region.

Yttrium aluminium garnet (YAG) only possesses very weak diamagnetism and so the problems of strong paramagnetism is removed. The lattice constant is 11.953 Å which is considerably different to YIG [85]. This can induce a much greater strain and
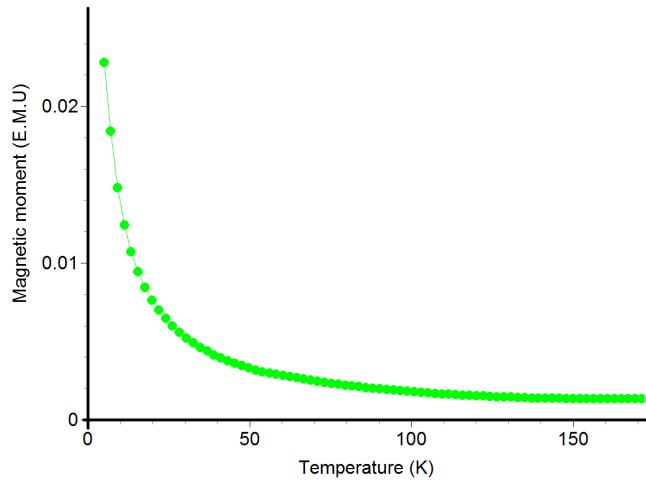
29

Figure 3.1: Magnetic moment vs temperature for a sample of GGG with an applied field of 10 mT. The size of this moment is comparable to the moment of a thin YIG film and can make hysteresis loop measurements difficult at low temperatures.

the propagation of magnons can be affected by this. The surface roughness is also increased and so GGG is the prime substrate used in this work. Silicon was also tested to see if the crystal structure could be made. This was abandoned as the annealing process produces visible cracks in the YIG surface. Due to the different coefficient of thermal expansion between the two materials strain is induced that breaks the continuous YIG film apart. These cracked films do exhibit magnetic behaviour as the annealing creates a polycrystalline form of the material. This does not necessarily prevent spin effects from functioning, but makes theoretical comparison difficult. Silicon was also used for YIG growth calibration rates because it deposits at the same rate as on GGG.

3.1.2 Sputtering systems

The best established method for making YIG samples for research purposes is LPE [86–88]. However this method is both expensive, complicated and unavailable with our current facilities. As research in magnetic insulators is expanding it is desirable to find a more convenient method that can scale up production of large numbers of samples. Magnetron sputtering is a method which is well established and relatively cheap [89; 90]. The basic chamber setup is illustrated in figure 3.2.
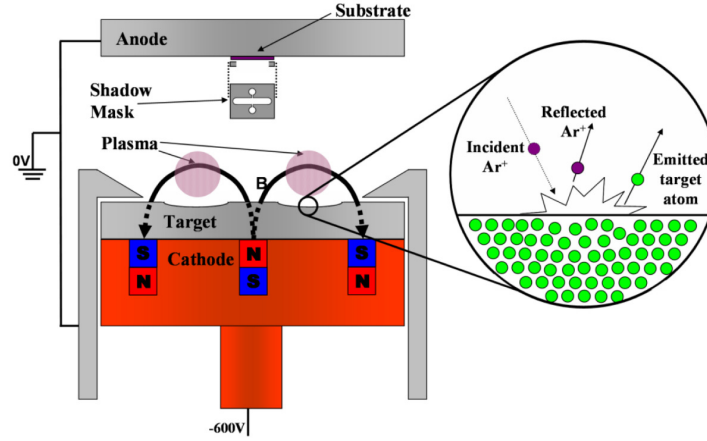
30

Figure 3.2: Schematic of the magnetron sputtering method. The target metal atoms are ejected by collisions from the argon plasma. Two different wheels are used for the sheet and masking growths by shielding parts of the substrate from the emitted atoms emanating from the target. Taken from [91].

Substrates are cleaned with acetone and IPA and mounted onto a wheel that is placed inside the chamber. The chamber space is evacuated by a turbo pump and then a cryopump to produce a UHV atmosphere of the order 10^{-7} Torr. The main residual components are water, nitrogen and oxygen. Water vapour becomes deposited on the sample surface and therefore can contaminate the samples. This water vapour pressure is reduced by passing liquid nitrogen through a shroud inside the chamber. The water molecules then freeze onto the shroud upon contact removing it from the atmosphere. The final base pressure is typically of the order of 10^{-8} Torr. An example of the typical partial pressures is given in table 3.1.

Atmosphere gas	Partial pressure ($\times 10^{-8}$ Torr)
Total	3.52
H_2O	1.54
N_2	1.22
O_2	0.37
CO_2	0.12

Table 3.1: Typical example of gas partial pressures in the chamber before deposition. The remaining contribution to total pressure comes from other inert gases.

A flow of pure argon is introduced into the chamber to provide an atmosphere set to a pressure of several mTorr dependant on the material being grown. This constitutes the working gas and is chosen due to its inert nature. A potential of approximately 600 V is created between the anode and cathode. This ionises the argon gas creating a plasma of high energy ions. A magnetic field is used to channel the ions down onto the surface of the target by the Lorentz force. The target is a disc made of the material which is to be deposited with a high purity. This control of the argon is important to prevent the ions striking any other parts of the gun or its surroundings. This can introduce different metals into the plasma that would contaminate the samples as well as causing damage to the chamber components. As the ions strike the surface at high velocity this transfers momentum into the target material atoms. This momentum is sufficient to enable atoms of the material to be ejected from the surface and into the chamber. A steady plume of the target atoms follow a random walk through the argon atmosphere where some reach the substrate and are deposited on it.

YIG targets consist of a stoichiometric mixture of yttrium and iron oxide powders sintered into a solid polycrystalline disc. Standard DC sputtering cannot be used as the YIG target is electrically insulating. This prevents DC current from flowing between the anode and cathode to complete the circuit. Instead an RF power supply is used as AC current can be transferred across the target acting as a buffer capacitor. The high frequency involved means the wave property of the current becomes a factor in power transfer. A resonant circuit in the power supply is tuned to give impedance matching to prevent power being reflected back to the source. As the different elements of the YIG target have different masses the individual sputter rates will not be equal. The YIG is believed to be deposited as a mixture of the individual elements and not in the garnet structure. Once ejected from the target surface they also have different mean free paths in the atmosphere. Adding oxygen to the argon atmosphere slows the growth rate down and allows the yttrium and iron to be deposited onto the substrate in the correct stoichiometry for YIG. This is due to oxygen build up on the target surface that reduces argon ions colliding with the metal atoms of the target material. Oxygen in this atmosphere also means that the amount sputtered from the target is irrelevant and ensuring that the deposited film is oxygen rich.

To deposit metal wires of a controlled shape and 200 μm wide, nickel masks are placed over the face of the sample. These are mounted onto an inner wheel that moves independently of the sample holder allowing multiple wires to be made on the same sample. These masks are cut in the shape of the wires we wish to make and of known dimensions, important for converting resistance measurements into resistivity.

3.1.3   Additional sample processing

The as-sputtered films are a brown, non-magnetic mixture of iron and yttrium oxides that show no crystal structure from XRD and no magnetism when measured by VSM. The intended crystallisation requires an annealing stage that reorders the atoms into the more energetically favourable garnet structure. This was done in a pure nitrogen atmosphere and a vacuum of 10^{-5} Torr, however both resulted in flawed samples. Significant improvement in the surface roughness and magnetisation was obtained when annealing in open air. To determine what temperature was needed a sample was placed in a weak vacuum of 10^{-2} Torr while carrying out high angle XRD *in-situ*. The temperature was heated to 600°C and a scan taken. Temperature is increased further and the scans repeated. It was found that the peak from the YIG gained intensity until 800°C where it shows little intensity difference from 750°C. This is the final temperature that was adopted for the standard recipe for making the YIG samples used in all the main results in this thesis. To prevent cracks appearing in the YIG the sample was heated at a steady rate of 7°C per minute to 850°C and allowed to cool naturally at a slower rate overnight. The annealing is left for 2 hours at this temperature as leaving it for longer was found to make no further difference. A test was done to see if rapid thermal annealing would produce high quality YIG but this failed. Partially this was because it could only be done in a nitrogen atmosphere without oxygen and also the sample showed marks on the surface that indicated cracks and a rough surface due to the rapid heating.

Samples are then prepared for reloading into the sputtering chamber for metal deposition. Basic cleaning of the YIG surface consisted of washing them in acetone and

IPO before being dried quickly to ensure no residue was left over. This step is to remove any contaminants that have landed on the surface during annealing and handling such as dust and grease. For all samples this process is done last and the samples placed as quickly as possible under UHV. Initial SHMR measurements were much smaller than what had been reported in the literature compared to samples made by LPE. This indicates that the interface of YIG and a metal grown on top has an oxide barrier between it. A more vigorous treatment was used to remove this barrier with piranha acid. This has been shown to improve spin mixing conductance [92]. Piranha acid is particularly aggressive which we used to burn through any possible crust formed on the top layer of the YIG during annealing. This crust can be formed due to imperfections in the stoichiometry and surface effects. The YIG garnet structure will form under annealing at the substrate first using the correct ratio of the elements from the assputtered film. Once one of the metals runs out the remaining material will not be able to crystallise in the correct garnet ratio at the top of the film. A yttrium or iron oxide barrier in a deformed garnet like structure is the most likely to form. The purpose of the piranha acid is to etch through this top layer to leave a pure YIG surface for sputtering metals onto. It is made by mixing pure sulphuric acid with hydrogen peroxide in a ratio of 3:1. The reaction has two different processes that provide etching. First the sulphuric acid is a strong dehydrating agent that reacts particularly strongly with organic material to form water. The reaction with hydrogen peroxide is exothermic that heats the solution to approximately 90°C.

$$H_2SO_4 + H_2O_2 \rightarrow H_2SO_5 + H_2O$$
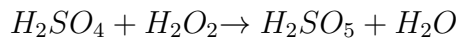
A secondary reaction releases atomic oxygen. This is a highly active oxidising agent which is capable of dissolving even elemental carbon and can attack any metal molecules not properly bonded in the garnet structure. The aggressive nature of this acid is found react with the YIG samples slowly dissolving the material at its surface.

$$H_2SO_4 + H_2O_2 \rightarrow H_3O_5^+ + HSO_4^- + O$$
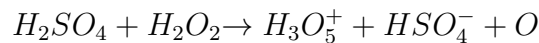
The etching process has been studied by XRR and AFM to confirm the effect it has. XRR shows that this acid treatment is able to dissolve YIG and so allows the top layers to be removed that may include any crust formed during annealing. The etching

rate was variable due to difficulty controlling the temperature of the mixed solution. The rate was found to range between 2 nm and 15 nm per minute. This highlights the strong effect of temperature on the acid reaction rates with a variation of approximately $\pm 5°$C. It was found that the faster etching rate increased the surface roughness and if its too slow it does not remove enough material. The optimum treatment was found to be 1 minute at 87°C removing approximately 5 nm of material. This treatment has now become standard in the preparation of YIG for spintronic research [93–95]

3.2 Sample characterisation

3.2.1 X ray reflectivity

The thicknesses of both YIG and the metals grown on top are measured by X-ray reflectivity (XRR). For the YIG this was done at each stage of the preparation to ensure that the processes worked as expected. An X-ray tube uses a high voltage to accelerate electrons released from a hot cathode towards a copper target at high velocity. Kinetic energy is then transferred to K shell electrons in the copper atoms causing them to be ejected. L and M shell electrons drop to fill this core hole producing an X-ray with an energy corresponding to the difference between the shell levels. Slits are used to collimate the beam and block bremsstrahlung radiation and any other spectral lines except Cu $K_{\alpha 1}$ and Cu $K_{\alpha 2}$. The X rays hit the sample at a low angle of incidence illustrated in figure 3.3. Specular reflection from the two surfaces of a thin film will constructively interfere as described by Bragg's law given in equation 3.1 [96–98].

$$n\lambda = 2d \sin \theta \tag{3.1}$$

Beyond the critical angle, θ_c, the intensity of reflected X-ray beam oscillates producing peaks when the Bragg condition is satisfied for an integer number of total internal reflections. These are known as Kiessig fringes that allow the thickness of the film to be determined from the angles, θ_m, at which they are detected given by equation 3.2.

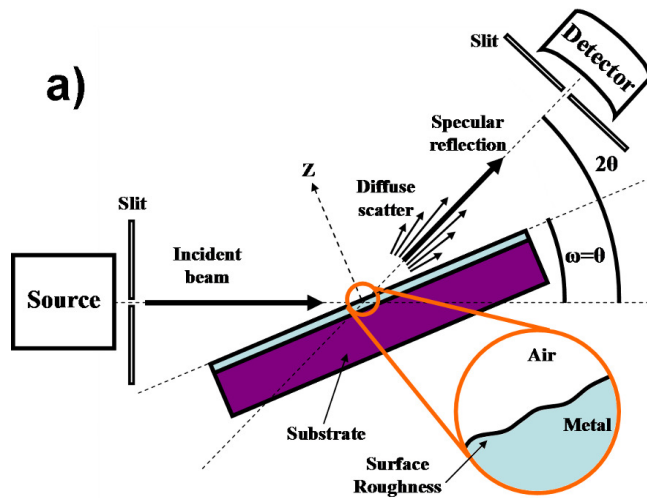$$\lambda = 2d\sqrt{\sin^2 \theta_m - \sin^2 \theta_c} \tag{3.2}$$

Figure 3.3: X-ray reflectivity schematic showing the incidence angle θ that is rotated during scanning and a detector that tracks at twice this angle. The intensity measured by the detector is then plotted as a function of 2θ. Image taken from [91].

As the specular reflection is due to a difference in electron density, this can provide information about the chemical composition of the top surface. A monochromator was also used to filter out the Cu $K_{\alpha 2}$ line and other background wavelengths. This removes the peaks from the other wavelengths and to make the peaks sharper allowing different peaks to be separated. The intensity of the X-rays is reduced considerably so a longer count time is needed.

3.2.2 X ray diffraction

The Bragg condition can also be intuitively applied to a regular pattern of atomic planes in a crystal. Raleigh scattering from these atoms constructively interfere and are detected as a peak in intensity as the sample is moved about the angle θ. The angle that the peaks are measured at allow for the lattice constant to be determined. The intensity and the full width half maximum (FWHM) gives a measure of the epitaxial quality of the crystal. Defects and strains in a crystal cause an increase in the FWHM [99]. Only certain lattice planes produce peaks as some reflections are forbidden by selection rules based on the miller indices [100]. For YIG the best location is the <444> peak which

is found at a 2θ angle of $51.05°$. The similar lattice constant of the YIG and GGG mean that the two peaks are very close together and so for this the monochromator is generally used to make the separation clearer.

3.2.3 Magnetometry

Magnetometry measurements are made on two different systems that use the same basic principle. The vibrating sample magnetometer (VSM) system is shown in figure 3.4. The original design used a vibrating coil around a stationary sample that has since been modified to a stationary coil system [101–103]. The sample to be measured is fixed to a holder that is then lowered into a cryostat with the top of the stick attached to an actuator. This vibrates the sample at 55 Hz with a reference signal from this connected to a lock-in amplifier. Around the VTI there are two pick up coils that have a voltage induced in them as the sample vibrates. This is due to Faraday's law of electromagnetic induction which depends on the size of the magnetic moment of the sample as well as anything else on the stick. This voltage is then detected by the lock-in amplifier which filters out the signal due to the frequency of the vibration provided by the reference source. This requires calibration to relate the voltage induced in the coil to the magnetic moment. This is dependant on the demagnetisation factor of the sample which is based on it's geometry.

A magnetic field of up to 9 T can then be applied in the vertical direction allowing hysteresis loops to be measured by sweeping the field. As the YIG often has a small magnetic moment, particularly when thin, more accurate measurements can be made using a SQUID VSM [104; 105]. This uses the same basic set up as a standard VSM but with the main difference being how the induced EMF is detected. A pair of Josephson junctions as part of a superconducting loop carries a current in the presence of a magnetic field. The application of a magnetic field from a sample induces a screening current in the superconductor that reduces the current in one junction and increases it in the other. This produces a voltage across the junction that can be detected. As the flux enclosed by the superconducting loop must be an integer number of flux quanta, the screening current changes direction each time the flux increases by a half integer.
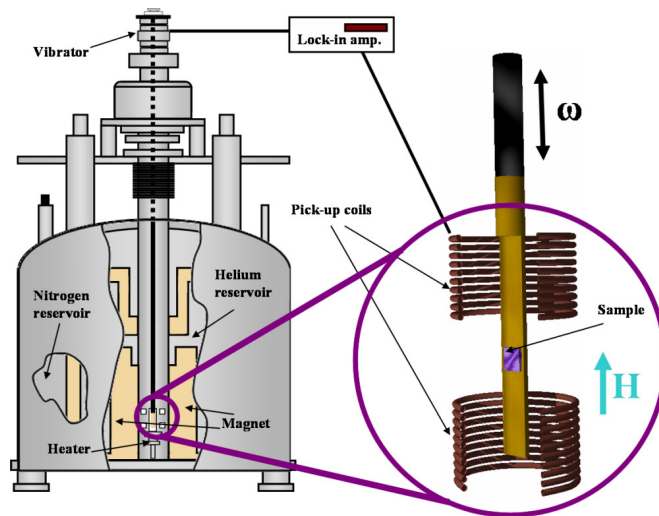
Figure 3.4: Schematic of a vibrating sample magnetometer. Samples are subjected to an applied magnetic field and vibrated. Induced voltage in the two coils is measured which are wound in opposite directions to reduce any background interference. Image taken from [91].

The period of the current reversal in the voltage across the junction can then be used to measure the magnetisation of a sample vibrating inside the loop.

3.2.4 Transmission electron microscopy

Transmission electron microscopy (TEM) is a well established method used to examine a sample in more detail than optical methods allow [106–109]. Diffraction limits the resolution of optical microscopes to several hundred nm. Electron wave-particle duality allows this to be improved to 50 pm with a magnification of up to 10 million times [106]. To be able to use the samples for this technique they need to have the material in the region of interest made thin enough to be transparent to electrons. Two methods can be employed for this. The first involves sandwiching the sample between several layers of silicon secured by an epoxy glue. This stack then has a circular core section drilled out of the side. This is then inserted into a brass tube which is cut into thin sections that are then ground down by friction pads as thin as they can be made without breaking. They are then placed into a vacuum chamber where a beam of argon atoms are fired along a focused path that bores a cone shaped hole through the centre

of the sample. The wedge shaped edge of this hole then contains a region of interest that is thin enough to study. The second method uses a focused ion beam (FIB) preparation. A layer of platinum is placed on top to prevent charge build up from the ion beam which does have to be considered as this platinum needs to be distinguished from the as sputtered platinum used in our samples. This is similar to the final stage of the conventional preparation except that the sample is only cut by a gallium ion beam so a large amount of the sample can be still used for other tests to confirm it is the same as the samples that are used for measuring SHMR. Samples of YIG were made with both platinum and tungsten and also both with and without the piranha acid treatment for comparison.
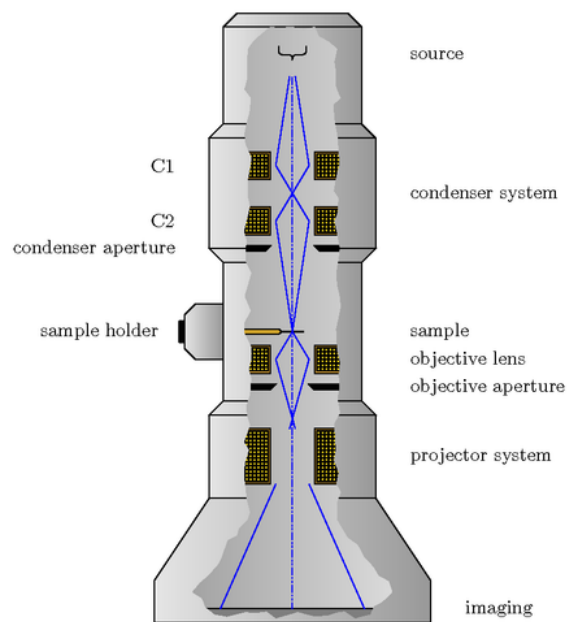

Figure 3.5: Basic schematic of transmission electron microscope. The path of the electrons is shown in blue being focused onto the sample. The scattered electrons are then used to image the atomic structure. Image taken from [110].

The samples were then loaded into the microscope as illustrated in figure 3.5. Here a beam of electrons are produced from a tungsten tip and then channelled by magnetic lenses down onto the sample. As electrons have wave-particle duality they are able

to pass and diffract through the thinnest parts of the sample. The electrons are then detected upon passing through the material and the diffraction patterns produced are used to create a bright field image of the crystal structure.

The microscope used in this work is a Tecnai scanning transmission electron microscope (STEM) which has additional functions from a standard TEM. The incident electron beam is able to be deflected by additional coils that scan the beam over a two dimensional area. Multiple measurements can be done simultaneously so that features can be cross referenced. Energy dispersive X-ray spectroscopy (EDX) is a technique that allows chemical analysis of the sample [111; 112]. The incident electron beam creates characteristic X-ray emission from the atoms of the sample in the same manner as the X-ray source in XRR. Detectors around the sample can measure the different energies emitted to produce a spectrum. This spectrum contains peaks that are a signature of the elements based on the specific atomic energy level transitions which can be analysed. STEM mapping uses EDX moved over an area of the sample allowing the elemental composition to be determined in different regions. This can show possible diffusion between layers and expose any possible contaminant.

High angle annular dark field imaging (HAADF) can be done at the same time as EDX as this detects incoherently scattered electrons that deviate from the main beam. These electrons are highly sensitive to the atomic number of the atoms in the sample. Line scans are taken that show how the chemical composition changes at sites of particular interest such as the boundary between YIG/GGG and YIG/NM. In particular, it will show if iron is getting into the platinum layer from the YIG and thus potentially contaminating it. The HAADF images provide the reference image as to where the line scans are being taken on the sample.

3.2.5 Atomic force microscopy

AFM is a technique used to probe the surface roughness of a sample. To do this a cantilever method is used whereby a tip is lowered onto the surface of the sample to be studied [113–116]. This tip is a sharp point having as little as a single atom at the end and its position is detected by use of a laser beam shown in figure 3.6. In tapping

mode the tip is vibrated at its resonant frequency perpendicular to the surface. As the tip approaches the surface the resonant frequency of this oscillation changes as it interacts with the surface due to electrostatic and Van der Waals forces. The shift in resonant frequency is used to determine the height of the sample surface. The sample is then rocked by a transducer that drags the tip across the sample surface in a line. The tip responds based on the height changes of the surface to avoid crashing into it and damaging the point. Each line is completed and followed by a retrace to confirm the data. It is then moved perpendicular to the line trace direction and a fresh trace is made. This is repeated until a two dimensional map of the surface is made. The scans can cover a square area up to 20 μm, beyond this the linear approximation of the rocking is no longer applicable. To confirm that the selected area is representative of the film, multiple scans on different locations are performed.
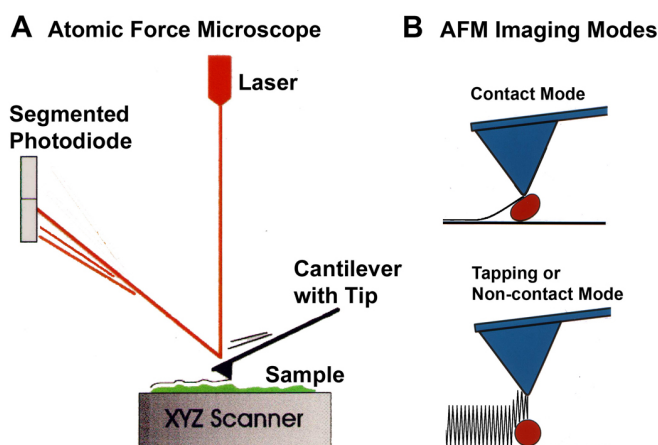

Figure 3.6: Schematic of AFM tip probing a sample surface. Measurements were done using tapping mode to produce a detailed image of the sample surface height and allows roughness to be calculated. Image taken from [117].

3.3 Transport measurements

3.3.1 Basic tests

To determine if a sample exhibits SHMR the simplest way is to measure the resistance of the metal wire as it is rotated in a magnetic field. A basic sample stick is used to

mount the sample in a static field of 80 Oe as hysteresis loops show this applied field is sufficient to saturate the YIG if applied in plane. The sample is then rotated through 360° about α as shown in figure 3.7. This can be done at room temperature where there is a small problem of temperature drift and it is sufficient to observe an angular dependence. This thermal drift can be removed by placing the sample in liquid nitrogen to give a better estimate of the SHMR. The resistance of the wire is measured by using a standard four probe method and a constant current supply [118; 119] illustrated in figure 3.8. By measuring voltages in this way there is no potential drop along the measurement probes and contact resistances are eliminated. The resistivity is then calculated from equation 3.3 using the cross sectional area and length between the voltage probes. The thickness is determined by XRR or using a profilometer. Where multiple wires of different thickness are made on a single YIG sample, XRR cannot be used on them individually and so calibration samples are used. The same material is grown on a similar sample in sheet form or with 4 wires through the mask set.
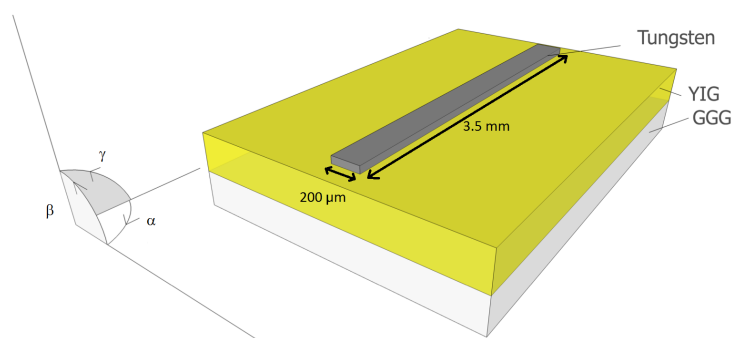

Figure 3.7: Illustration of typical YIG sample on GGG substrate with tungsten wire. The angles indicated define the direction that the sample is rotated about while subjected to an applied magnetic field in a fixed orientation.

These can be measured by XRR and the growth rate extracted allowing the thickness of individual wires to be calculated. The profilometer can be used on thicker wires to confirm that these growth rates are correct. The comparison between the growth rate of sheet material and wires grown through the masks shows them to be near identical.
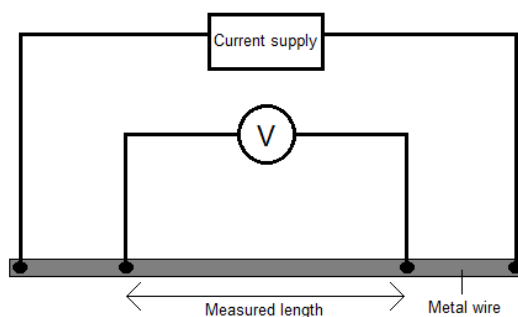
$$\rho = RA/L \tag{3.3}$$

Figure 3.8: Four probe resistance measurement formation. The voltage probes do not carry the applied current eliminating a potential drop along the probes themselves. The potential difference and the known current are then used to calculate resistance measurements that are highly accurate.

Shadowing effects have to be considered when sputtering through a mask. Due to the random walk of the atoms the deposition rate is reduced at the edges of the mask. This would weakly distort the geometry used in equation 3.3 and so the extent of this deviation is checked by using a Dektak profilometer. From this we found that the wire cross section is approximately rectangular and so we can make an accurate approximation of the cross sectional area from the wires width and thickness.

3.3.2 Cryostat measurements

A cryostat is a device that is used to maintain low temperatures around a sample [120; 121]. The basic schematic is illustrated in figure 3.9. The cryostat consists of three main sections. A variable temperature insert (VTI) is placed in the centre that holds the sample stick. A flow of helium gas is let into the bottom and the temperature is controlled by a heater. The operational temperature range is between 1.5 - 300 K and measurements are typically done at a pressure of 5 mbar. Surrounding the VTI is a helium reservoir that maintains low temperatures and provides the gas flow. A liquid nitrogen jacket is placed around the helium storage to reduce the boil off rate in the helium reservoir. A split pair of current coils that generate fields up to 3 T is placed on both sides of the VTI sample space. The coils are kept cold by the liquid helium jacket allowing them to superconduct. This allows a current to be put into them in persistent mode giving a stable applied field without power consumption.
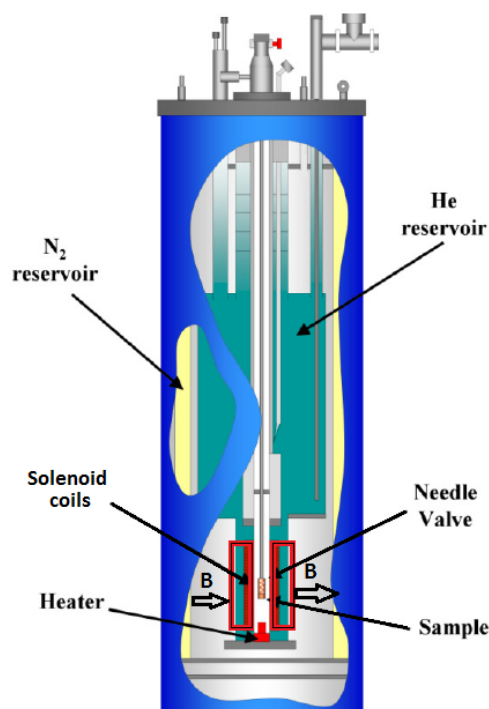
Figure 3.9: Schematic of a cryostat. The stick in the centre is able to rotate about its length with the sample at the end subjected to a horizontally applied field. The sample can be mounted to allow rotation in any orientation. Taken from [91].

Samples are mounted onto a brass head in four point probe configuration. The mounting orientation is chosen based on the measurement being done but cannot be altered *in-situ*. The head is attached to a stick that is lowered into the VTI. The resistance of the sample wires is measured by taking average readings using both forward and reverse currents. This helps eliminate any thermal EMF effects. The sample stick is rotated by a controlled stepper motor attached to the top of the stick outside the cryostat. This is to reduce any Joule heating of the sample during motion. Angular dependence of the SHMR is determined by rotating the stick in a magnetic field sufficient to saturate the magnetisation of the YIG. The rotation is done in small steps operated by a motor and resistance measurements taken at each angle. The temperature had to be kept very stable as any drift alters the resistance of the wire by an amount comparable to the effect being measured. The temperature is detected by a thermometer that is

mounted on the brass head close to the sample mount.

The SHMR temperature profile can be measured by conducting angular rotations at a range of stable temperatures. This is inefficient as the temperature stabilisation is highly time consuming and yields less detailed data. The solution to this is to constantly move between the maximum and minimum resistance angles while the temperature is lowered at a controlled rate. This shall be referred to as the dynamic temperature method and typical data for this is shown in figure 3.10. The green data points are taken with a 90°difference between the orientation of the field relative to the sample from the yellow data points. An interpolation of these two data sets then gives the resistance change that is due to the SHMR by the vertical difference between them at a given temperature. The advantage of this method is that the SHMR can be extrapolated at frequent temperature intervals of less than 1 K across a large overall temperature range in a single experiment. This was confirmed to work by measuring samples by both methods at several different temperatures and they were found to differ from each other by no more than 5%.
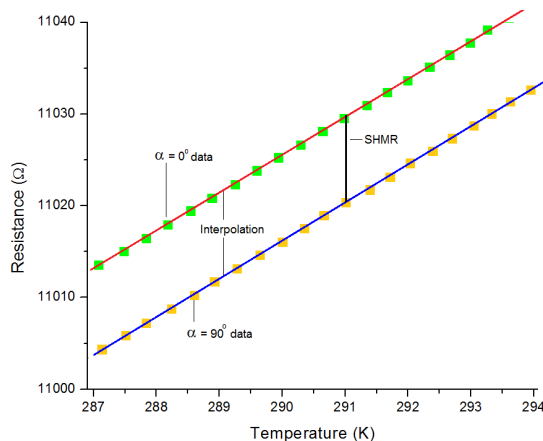
Figure 3.10: Resistance measurements of a platinum wire taken under reducing temperature at two different angles. These angles are 90°apart corresponding to the maximum and minimum SHMR contributions to the resistance. SHMR is determined by the vertical difference between the two linear fits for a given temperature.

A more basic technique was also used to measure the SHMR by subjecting a stationary sample to a variable magnetic field. A magnetic field is applied to the sample with a low angle to the plane of the sample in order to control the magnetisation vector of the YIG as shown in figure 3.11. When the applied field is large the YIG magnetisation will be out of the plane and at low fields the anisotropy of the YIG film will rotate the magnetisation direction into the plane of the sample. The low angle gives a component of the applied field along a fixed direction within the plane of the sample which allows the SHMR to be approximated by the resistivity difference between the low field and high field regions. This method is not as accurate as other methods used because the magnetisation of the YIG is not fully rotated due to the low angle of the sample. This method only provides an estimate of the size of the SHMR and no clear information about its angular dependence.
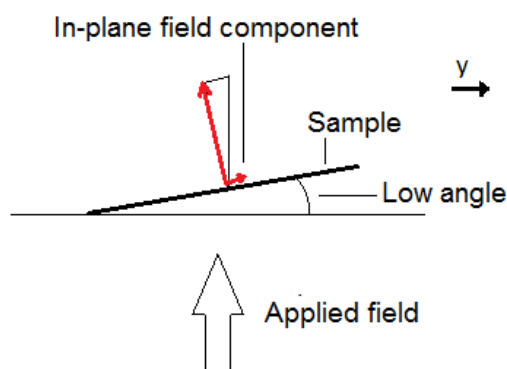

Figure 3.11: Banked sample to approximate rotation of the YIG magnetisation. The low angle allows the YIG magnetisation to rotate into a specific direction in the plane of the film due to the in plane component of the applied field.

CHAPTER 4

YIG sample characterisation

As the garnet structure with the YIG elements does not exist in nature it has to be manufactured using a seed material of a different garnet. The first method developed to make single crystal YIG is by liquid phase epitaxy [86–88]. This is similar to the Czochralski process that GGG and many other substrates are made by. A mixture of ytrrium and iron oxides are added to a flux of boron and lead oxides. This is then heated in a platinum crucible to approximately 800°C where it exists in a liquid state. A garnet structured substrate is then lowered into the liquid flux and stirred as the YIG grows rapidly and in its epitaxial state. To make YIG more economical to grow other methods have been developed. PLD and sputtering methods have been tried with increasing degrees of success. Problems with the quality of these methods were found that needed to be addressed. In particular early sputtering attempts showed that the surface roughness was high and magnetic properties did not match that of the expected bulk values as seen in figure 4.1.
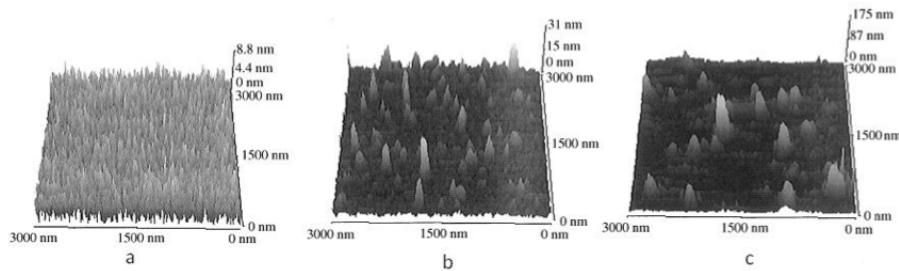

Figure 4.1: Illustration of AFM on early sputtered YIG showing different size and density of asperities on the film surface for annealing temperatures of 900°C, (a), 1000°C, (b), and 1100°C (c). Taken from [122].

In some of these experiments the YIG was annealed *in-situ* and in a weak oxygen atmosphere. Also there was no treatments done on the films before any metals were grown on top. It was later found that acid treatment has been used even on materials made by LPE. Our first publication showed the benefits of annealing in open air allowing the film to absorb oxygen and this step has since been cited in several subsequent papers [123; 124]. Many doped garnet crystals have been made using the basic YIG formula with small substitutions of the elements. This allows for fine tuning of its magnetic and optical properties [125; 126]. It is also used as a band pass filter in spec-

trum analysers due to its narrow absorption bandwidth [127]. Some basic properties of YIG are given in table 4.

Property	Standard value
Density	5.11 g/cm^3
Electrical resistivity	10^{14} $\mu\Omega$cm
Curie temperature	553 K
Magnetisation	142 emu/cc (at 25°C)
Melting point	1555°C

Table 4.1: Fundamental properties of bulk YIG.

4.1 Growth parameters

For YIG to be made consistently the growth parameters need to be carefully defined. The material has to be magnetic with the correct epitaxial crystal structure. As metals are being grown on the top surface, roughness is also important. To obtain the optimum conditions the sputtering power, sputtering atmosphere and annealing conditions were varied. As part of this research and other related projects over 600 samples of YIG were made. A series of YIG samples were made with consistent power of 50 W and 75 W. The oxygen content was varied and XRR used to determine the growth rate.
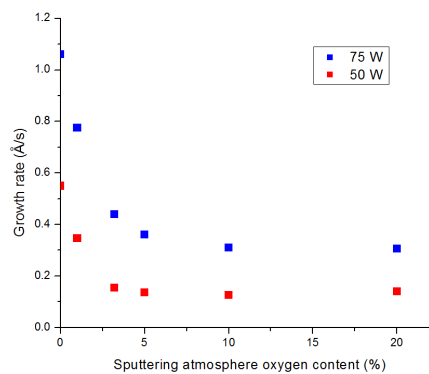

Figure 4.2: Growth rate of YIG as a function of oxygen content in the sputtering atmosphere. Grown at 2.7 mTorr at 75 W (blue), and 2.7 mTorr at 50 W (red) showing a saturation in the growth rate above 5% oxygen content.

Figure 4.2 shows that a small amount of oxygen significantly reduces the growth rate and that further oxygen content has a diminishing effect. From this it can be deduced that the oxygen builds up on the surface of the target which reduces the sputtering rate. This effect becomes saturated above 5%. The oxygen content will also affect the diffusion constant of the different elements in the sputtering atmosphere and increase the initial oxygen content of the film. The surface roughness becomes larger as the growth rate is increased. AFM measurements on samples both before and after annealing found that the post-anneal roughness is dependent on the pre-anneal film surface. This is expected and so a slow growth rate was adopted to reduce the surface roughness. At 50 W and 5% oxygen content the sputtering rate is approximately 0.26 ± 0.01 Å/s. These conditions yield an as-sputtered YIG RMS surface roughness of 0.12 ± 0.01 nm over 100 μm^2. This is the same roughness as the polished GGG substrate surface. Thicknesses were measured on all batches to monitor the stability of this growth rate. In a single batch the rate was found to be consistent within 0.01 Å/s. After a year of use the growth rate began to rapidly increase to as high as 0.40 Å/s. This is due to thinning of the target increasing the sputter rate that was occasionally corrected by changing the power, pressure or replacing the target. No samples that were made with these higher growth rates were used for measuring the SHMR.

4.1.1 Annealing effects

The annealing temperature was determined by XRD. An as-sputtered YIG sample was mounted on the XRD goniometer and under a weak vacuum of 10^{-2} Torr. A high angle XRD scan was taken around the GGG <444> peak. The temperature was then raised to 600°C and the scan then repeated. The data in figure 4.3 show that the YIG peak continues to grow up to 800°C which is the maximum the instrument could operate at. The final lattice constant after annealing from the Cu K$_{\alpha2}$ wavelength is 12.352 ± 0.002 Å compared to a bulk value of 12.376 Å [128]. Before each scan was taken the temperature was allowed to stabilise for 1 hour. This information is in agreement with literature values [129; 130]. To ensure good crystallisation 850°C was used for 2 hours. Twin samples of YIG were used to determine if higher temperatures up to 1000°C and a longer anneal time of 24 hours made a difference. These tests showed

no difference to annealing for 2 hours at 850°C. No peaks corresponding to other iron or yttrium oxides were observed in any samples both before and after annealing.
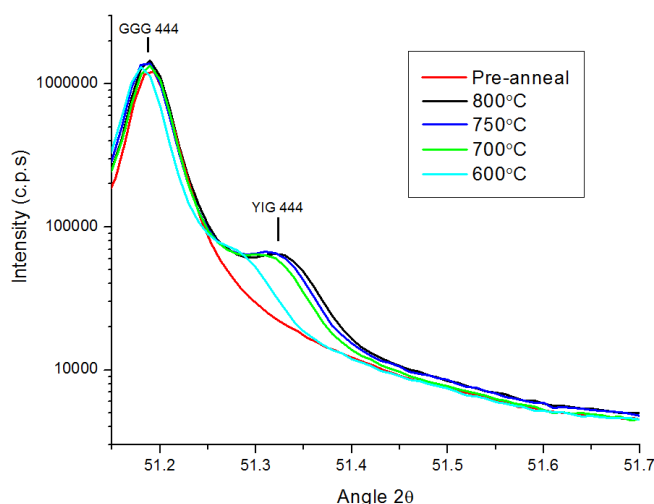

Figure 4.3: X-ray diffraction scans taken as a YIG sample is annealed at different temperatures. The YIG peak grows in intensity until 800°C where it then stops. This determines the temperature needed for strong crystallisation of the YIG.

The annealing atmosphere was also shown to give much smoother surfaces using an oxygen atmosphere. Pure nitrogen and a weak vacuum of 10^{-5} Torr were also tried. These both showed asperities on the surface that are undesirable. For comparison twin pieces of YIG were annealed in both nitrogen and open air. The RMS roughness is much lower using open air, (0.35±0.05 nm), than for nitrogen, (4.8±0.5 nm), and the asperities are no longer present shown in figure 4.4. We believe that the reason for this is that any oxygen deficiency in the as-sputtered films is provided by being annealed in air. During the annealing process the film then absorbs the required oxygen from the atmosphere. The asperities are always present in films annealed in nitrogen or a vacuum and from this it can be concluded that the as sputtered films are oxygen deficient. As a result annealing in air was adopted as the best option for smooth YIG films. The oxygen content of the as sputtered films is believed to be affected by the sputtering atmosphere content but not enough for full garnet crystallisation without additional oxygen from the annealing atmosphere.

(a) Air   (b) Nitrogen

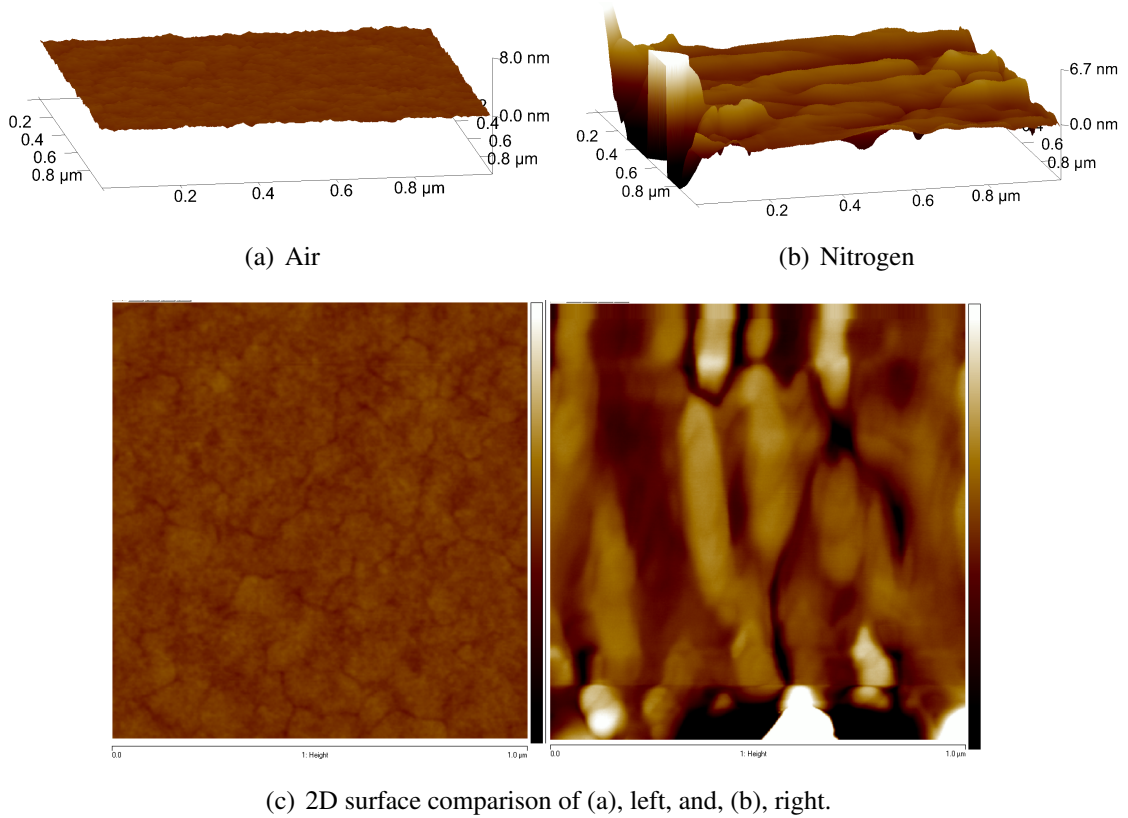(c) 2D surface comparison of (a), left, and, (b), right.

Figure 4.4: AFM on identical YIG on GGG annealed in air (a) and nitrogen (b). The two dimensional images are shown in (c). A clear difference can be seen with the air atmosphere during annealing yielding the smoother surface.

AFM measurements after annealing in nitrogen show how the surface roughness is dependent on the oxygen content used in the sputtering atmosphere. Comparison of these show that the columns are different in figure 4.5. From the plot of the RMS values we see that a 5% oxygen mix provides the smoothest YIG after annealing. This combined with other experiments later determined that this is the optimum condition for the sputtering atmosphere. The annealing atmosphere is what provides the necessary oxygen stoichiometry. However the oxygen in the sputtering atmosphere does provide a much smoother surface before annealing by reducing the deposition rate and balancing the metal stoichiometry. Once all YIG samples were annealed in open air

the AFM images were consistent and no further asperities were seen on the films for samples grown on GGG.

(a) 0% oxygen

(b) 3.2% oxygen

(c) 5% oxygen

(d) 10% oxygen
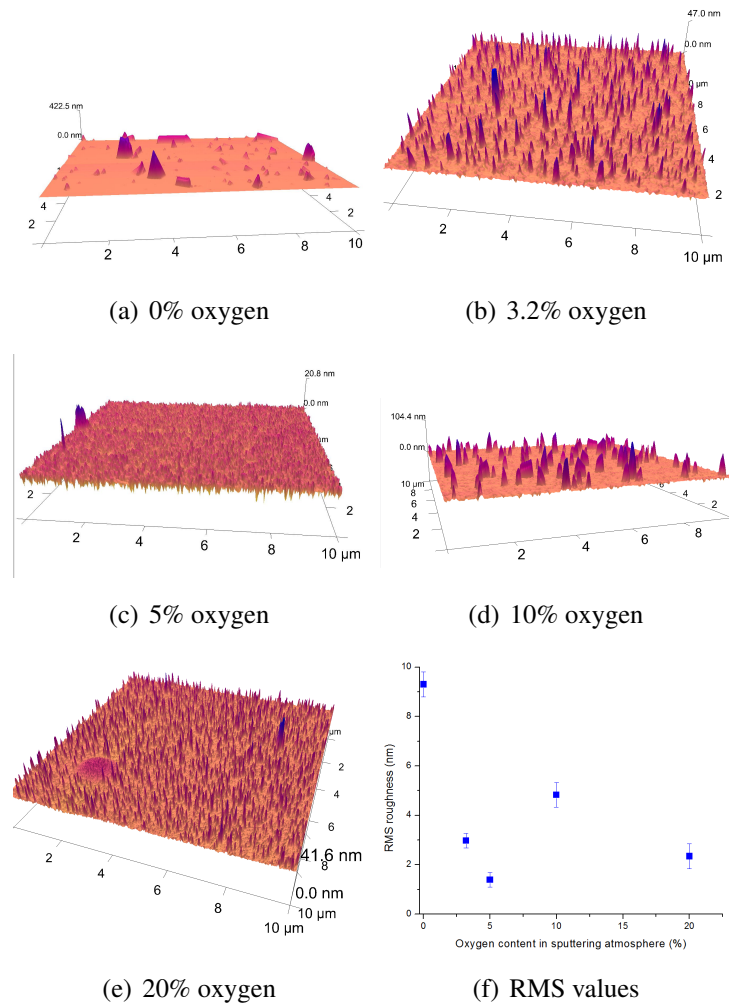
(e) 20% oxygen

(f) RMS values

Figure 4.5: AFM on identical YIG on GGG annealed in nitrogen with a different oxygen content in the sputtering atmosphere. The optimum condition for smooth films is found using 5% oxygen content.

When the YIG target became thinner and the sputter rate increased the films were found to be rougher despite a 5% oxygen content sputter atmosphere. Subsequent annealing in air did not smooth the roughness out. The reason for the increased roughness for 10% is not understood but could have been due to bad sample alignment during

sputtering.

XRD peaks from the GGG substrate are doubled due to the Cu $K_{\alpha1}$ and Cu $K_{\alpha2}$ lines. To separate the YIG and GGG peaks the Cu $K_{\alpha1}$ is the only wavelength used. Figure 4.6 shows that the peaks are much better separated than is seen in figure 4.3. A rocking curve taken aligned to the YIG peak shows a sharp line indicating that the crystal quality is high. As a result the YIG peaks are measured with the monochromator for better comparison.
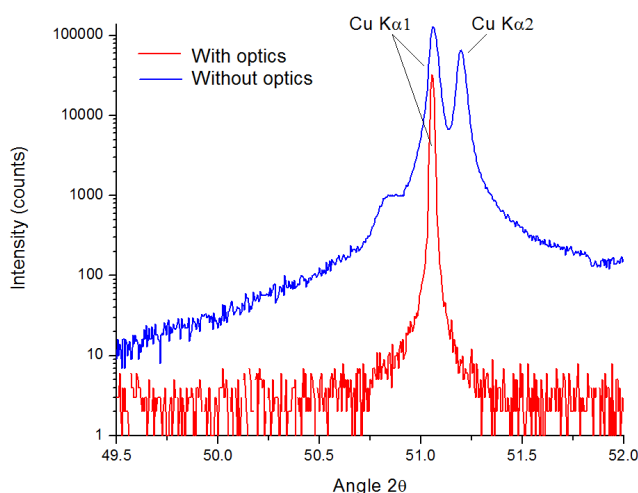

Figure 4.6: High angle XRD scan of blank GGG substrate with, (red), and without, (blue), monochromator. The use of the monochromator makes individual peaks from YIG much easier to distinguish from the GGG.

Several samples were subjected to XRD scans at each stage of the YIG preparation. This demonstrated that the annealing process is necessary for any crystal structure to be formed as seen in figure 4.7. No as-sputtered sample on any substrate was found to have crystal structure detected by XRD. The location of the peak however is not in the expected place for the bulk lattice constant. For all samples prepared on GGG and annealing in air, the YIG peak is at a lower angle than the GGG. This is in contrast to figure 4.3 which was annealed in a vacuum which is closer to the bulk value than in air implying the film is strained.
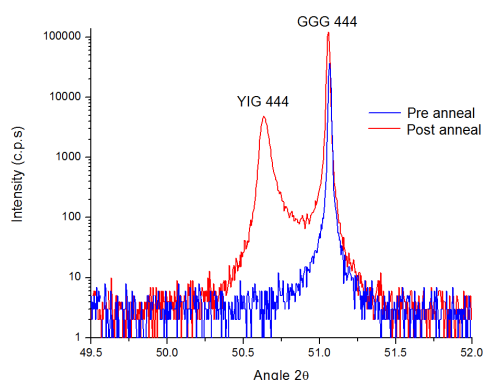
Figure 4.7: High angle XRD scan of YIG film using the monochromator before, (blue), and after annealing (red). The YIG peak can easily be distinguished in the post anneal scan due to the crystallisation of the film.

Another experiment was performed to test the use of rapid thermal annealing. For this a 50 nm piece of YIG on GGG was placed into a sealed heating chamber with a pure nitrogen atmosphere. The temperature was raised to 850°C for 20 seconds. The heating and cooling took 150 seconds each. This sample was compared to a twin annealed at 850°C in open air and the results are shown in figure 4.8.
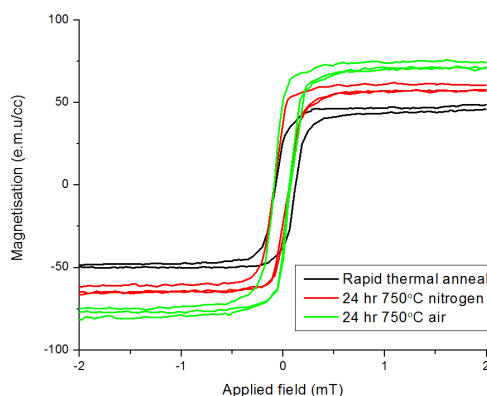

Figure 4.8: In plane hysteresis loops of identically grown YIG after rapid thermal annealing, (black), annealed slowly in open air (green) and annealed slowly in nitrogen (red). Measurements taken at 250 K. All films are below the bulk value for YIG with air giving the closest value.

Hysteresis loops indicate that the YIG has crystallised to form a magnetic material

but with a significantly reduced magnetisation value compared to slow open air anneal and the accepted bulk value of 140 e.m.u/cc. The surface roughness was too high to be able to measure the thickness for rapidly annealed films. Inspecting the surface by eye revealed that the YIG contained small multicoloured regions on the surface. Defects and strains cause a wide range of colours in gems and so the conclusion is that the high speed of the annealing has caused this.

4.1.2   Etching effects

To counter the column growth of the YIG, ion milling was attempted to reduce the surface roughness. The YIG sample was bombarded by 1 kV argon ions at a 55°angle of incidence. This was found to reduce the columns height by two thirds but not completely. As the film thickness is 117±3 nm a reduction of around 50 nm and still not yielding a surface as smooth as those annealed in air is not a practical solution to the problem. To flatten the surface to an acceptable level would remove the entire thickness of the YIG and require a long processing time. Ion milling is also used as an etching process to improve the spin mixing conductance [92]. Pilot experiments on this demonstrated it was not as effective as treating with acid.

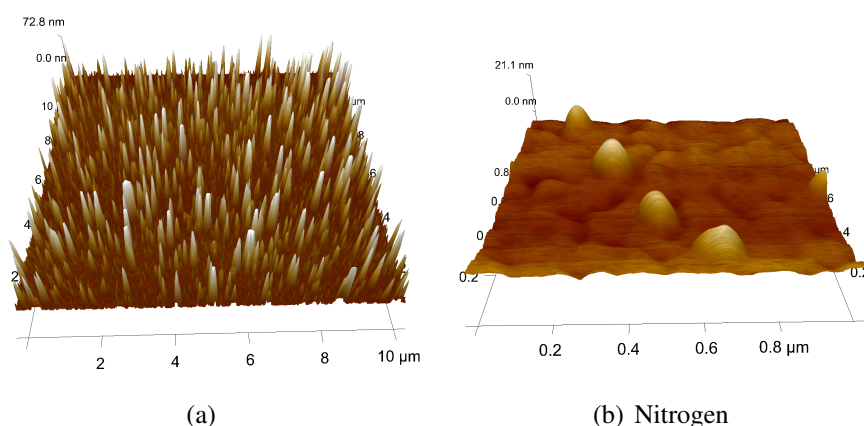(a)   (b) Nitrogen

Figure 4.9: AFM images of YIG sample before, (a), and after ion milling, (b). This shows a clear reduction in the surface roughness yet it does not make the film as smooth as samples made without the column growths.

Piranha etching described in chapter 3 removes a variable amount of material and so the XRR is necessary to know the final sample thickness as calibration rates may not be accurate. In general the hotter the acid the higher the etch rate. The rate of cooling after the sample is inserted cannot be directly controlled with the available facilities. Further complication arises from the different etch rate of the garnet structure and any different material on the untreated surface. A GGG substrate was also treated with the acid before YIG deposition and compared to untreated substrates. No difference was found to occur. XRD measurements are not substantially affected by acid etching of the YIG except an anticipated reduction in the peak intensity that is proportional to the YIG thickness.

XRR measurements were done on several YIG samples at each stage of preparation. Extraction of the YIG thicknesses from figure 4.10 show that the annealing has very little effect on thickness. The critical edge shows little change indicating that the electron density on the surface is similar.
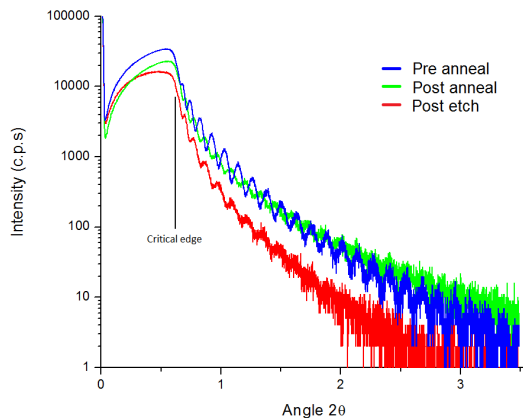

Figure 4.10: Typical example of XRR measurements taken on YIG at each stage of preparation. The Kiessig fringes decay considerably after annealing due to the similarity in electron density across the YIG/GGG interface after crystallisation.

These thicknesses can be measured accurately up to 170 nm. Beyond this thickness, Kiessig fringes are too close together to distinguish. A calibration growth rate is used based on the thickest film that the thickness could be determined to provide an estimate. With the growth rate of 0.26 Å these thicker films take several hours to

grow. This does give considerable time for a small change in sputter rate as a result of pressure variation or heating of the target and substrate. To check the growth rate a second calibration sample is done at the end of the growth.

4.1.3 Silicon substrates

YIG was first attempted to be grown on silicon. Using this substrate, growth rates were established and magnetic insulating YIG films were successfully grown. The annealing process does cause a poor quality YIG film to be formed however. XRD shown in figure 4.11 demonstrates that the YIG is polycrystalline. This is similar to what is seen in the literature for non-garnet substrates [131]. To help promote the growth of epitaxial YIG, a 5 nm thick seed layer of tantalum or copper with lattice constants of 3.310 Å and 3.597 Å respectively was first added to the silicon before YIG deposition. This increased the crystal nature as seen from the intensity of the peaks yet they still show multiple crystal orientations. Magnetometry shows an in-plane coercive field of 45 Oe which is much higher than on GGG. These samples even exhibited visible cracks in the surface.
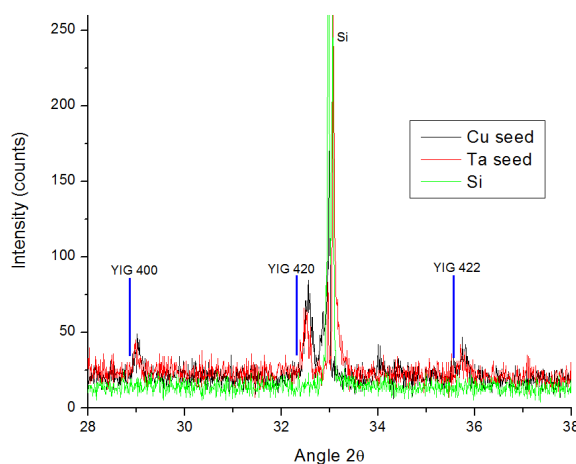

Figure 4.11: XRD of YIG grown on silicon. Also shown with a Ta and Cu seed layer where the peaks attributable to the YIG have a higher intensity indicating a higher degree of crystal ordering.

This is due to the thermal expansion coefficient being considerably different on silicon (2.50×10^{-6} K^{-1}) than YIG (1.04×10^{-5} K^{-1}). The surface roughness is high

(a) SEM image of cracked YIG surface
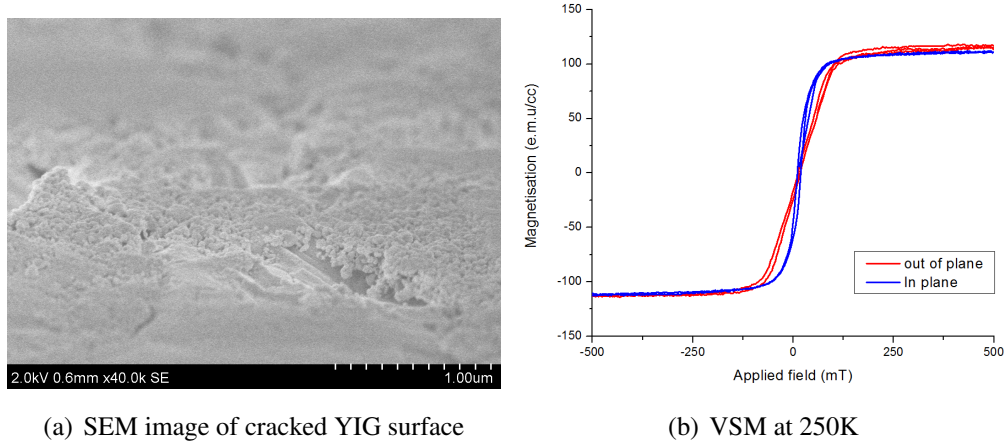

(b) VSM at 250K

Figure 4.12: Properties of YIG grown on silicon after annealing. The magnetic measurements indicate bulk like behaviour however the surface roughness is unacceptably high to use for SHMR experiments.

as a result with XRR measurements unable to measure the thicknesses after annealing. In the event that high quality YIG could be made on silicon the substrate cannot be cleaned with piranha acid. The silicon substrate would be rapidly consumed by the oxidation process in a potentially explosive reaction and so an alternative treatment would need to be employed.

4.1.4 YAG substrates

Several samples were grown on yttrium aluminium garnet (YAG) substrates. These were made alongside twin samples on GGG for comparison. The as-sputtered films were both smooth and of similar thicknesses. These were annealed at 850°C in open air. After annealing the AFM shows a considerable difference in the YIG depending on the substrate. This surface roughness is also confirmed by the XRR where the Kiessig fringes become too faint to distinguish on the YAG substrate samples. Before annealing the RMS roughness on YAG and GGG substrates were 0.08±0.01 nm and 0.12±0.01 nm respectively. Post annealing these values change to 1.1±0.1 nm and 0.37±0.05 nm. The different lattice constant of the YAG (11.953 Å) is considerable and has induced a strain on the YIG due to the mismatching. Magnetometry compar-

isons reveal noticeable differences in the hysteresis loops. The likely polycrystalline nature of the YIG films is the most probable explanation for the wider coercive field.

(a) GGG pre-anneal

(b) YAG pre-anneal

(c) GGG post-anneal

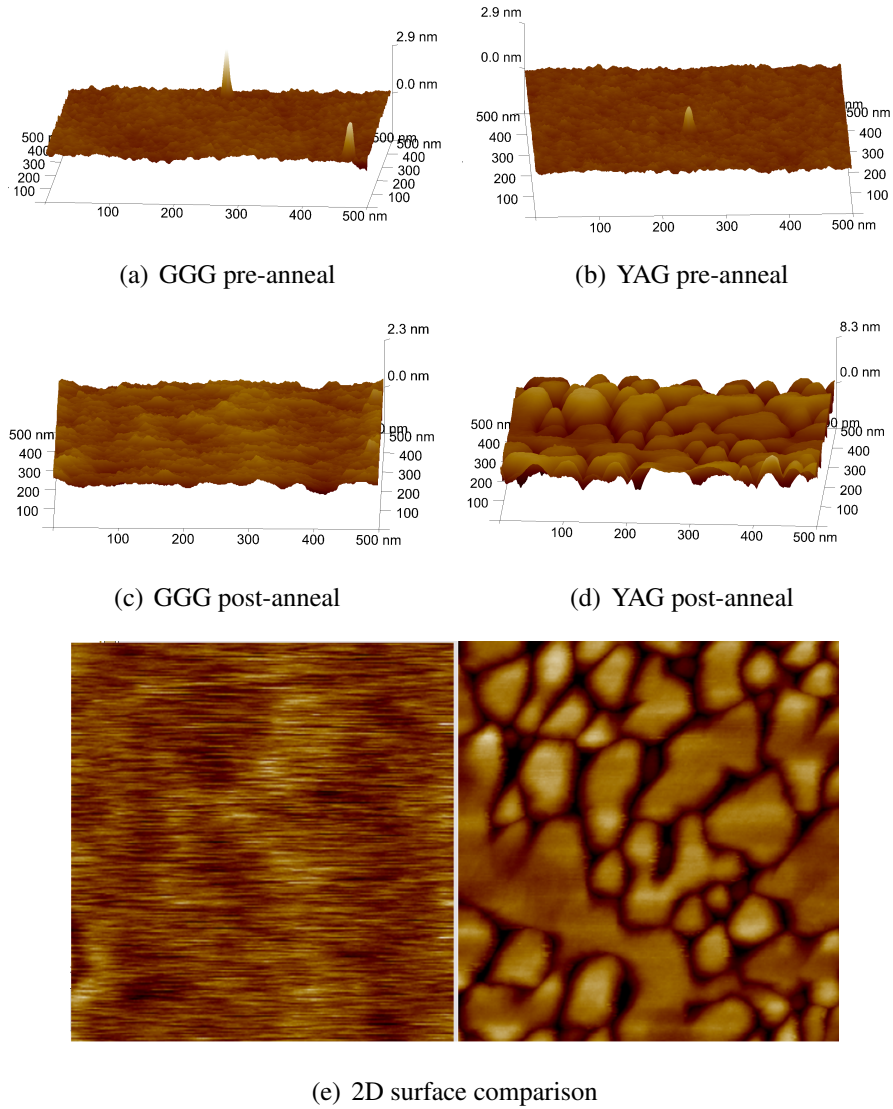(d) YAG post-anneal

(e) 2D surface comparison

Figure 4.13: Comparison of AFM scans on YIG films grown on GGG and YAG substrates. Samples annealed in air with 5% oxygen sputtering atmosphere. The GGG substrate produces the best surface but YAG leaves distinct mounds after annealing.

YAG was not extensively studied due to these differences however it still holds

(a) XRD scan for YIG on YAG post anneal
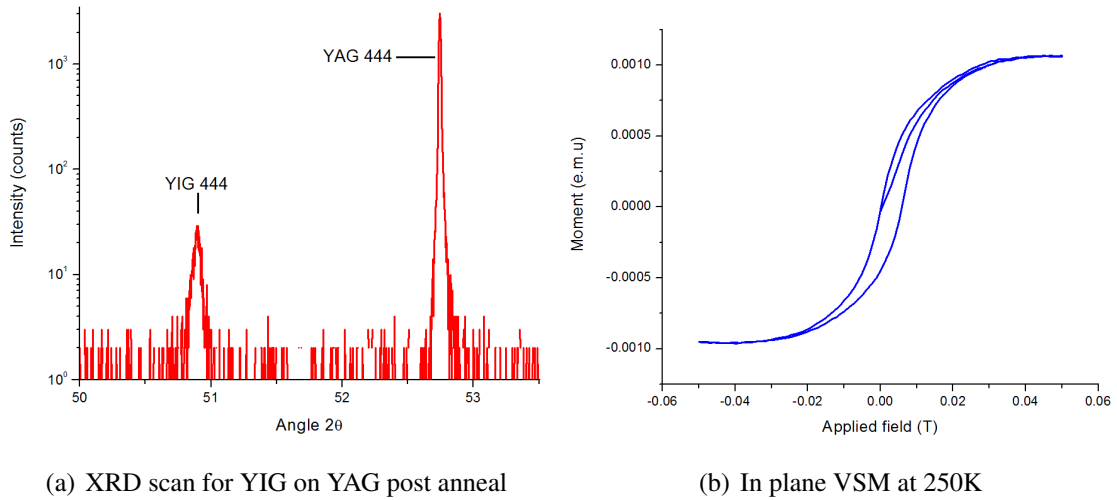
(b) In plane VSM at 250K

Figure 4.14: Properties of YIG grown on YAG after annealing. The crystal properties and magnetic measurements indicate that the film is bulk like with the only negative property being the surface roughness.

some value for research purposes. YAG will also be revisited in chapter 5 as platinum wires were found to show the same SHMR as the twin YIG films on GGG. YIG on YAG has a very different surface as seen in figure 4.13. The as-sputtered material is the same as the GGG. Post annealing a considerable difference is found. Here we see a regular pattern of smooth bubble shaped curves. This indicates that the lattice mismatching is creating columns of crystal structure that are disjointed from each other. XRR data also show a decay in the Kiessig fringes that make the thickness impossible to determine. This is due to the granular features being large on the scale of the X-ray wavelength. Acid etching is likely to open the channels between these features and make them wider and further increasing the roughness. Figure 4.14 shows that the YIG is still magnetic and has crystal structure on the YAG. From this we see that the YIG is still made and that it is only the surface roughness that is the key issue favouring GGG.

In conclusion the GGG is the only suitable substrate to make smooth YIG films. The RMS roughness is found to be low on all thicknesses made and on all samples measured that were prepared by the standard recipe.

4.1.5   Hot growths

A few YIG samples were prepared by sputtering onto a heated substrate. GGG substrates were placed into a different sputtering chamber and heated. A 5% oxygen sputtering atmosphere was used to keep the growth as similar to other samples as possible. The samples were deposited at 500°C up to 650°C. None of these samples showed magnetism before annealing and were found to be too rough for a thickness to be determined by XRR. These samples were then annealed and AFM images were then taken. These samples did exhibit magnetism post anneal, however figure 4.15 shows the YIG has been transformed from a thin film to a series of regular mounds. The height and density of these mounds suggests that all of the YIG material has condensed into these columns. As a result the hot grown YIG was abandoned to pursue the cold growths annealed in air. This method could still hold potential if the surface roughness problem can be resolved which we believe will require a high oxygen content whilst being sputtered onto the heated substrate. If successful this could produce epitaxial YIG as-deposited with a low surface roughness and may not need etching. As a result any metal could then be deposited *in situ* making a complete device in one growth.

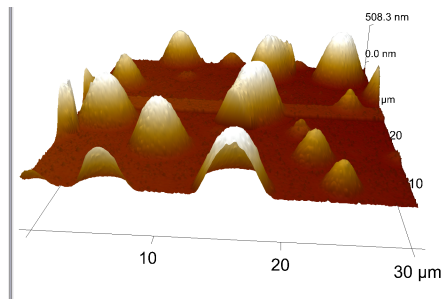Figure 4.15: AFM image of YIG grown at 650 °C after annealing. This films surface is clearly not suitable for a device as all of the YIG material appears to have amassed into columns up to 500 nm high.

4.1.6   Optimal YIG recipe

From these experiments the optimum conditions were determined and a standard recipe for YIG growth drawn up. This is given in table 4.2. Samples made using these condi-

tions have been consistent for a period of around 1 year. The remainder of the results in this section are based on YIG made by the standard recipe with optional acid etching unless otherwise stated. Also GGG was chosen as the standard substrate with the <111> axis pointing out of the plane. Where any differences were found on new samples that deviated from what is expected they were not used for SHMR measurements. Towards the end of the project the sputter rate began to increase considerably and the surface roughness of the samples increased. This is most likely due to the target becoming thinner and so it was replaced with a new one. This new target is yet to produce YIG that exhibits the bulk magnetisation and the reasons for this are still not clear. None of the samples in this thesis are from this new target.

Growth condition	Standard value
Growth rate	0.26 Å/s
Growth atmosphere	95% Ar 5% O_2
Sputter pressure	2.4 mTorr
Annealing temperature	850°C
Annealing atmosphere	Open air
Annealing time	2 hours

Table 4.2: YIG growth parameters adopted for the standard growth process.

4.2 Variation of YIG thickness

4.2.1 Magnetisation properties

VSM measurements were taken on most YIG samples to confirm they are magnetic. The coercive field and the magnetisation are both important quantities to determine. On the samples annealed in a nitrogen atmosphere the YIG is found to have a wide coercive field compared to those annealed in air shown in figure 4.16. The coercive field of these films is wide which is likely to be as a result of poor crystal quantity. The magnetisation is also found to be below the bulk value. This is likely due to the lack of oxygen in the films preventing the super-exchange coupling the iron atoms. If the oxygen is missing in particular regions this could be modelled as a polycrystalline material composed of lots of small regions of epitaxial YIG separated by defects.
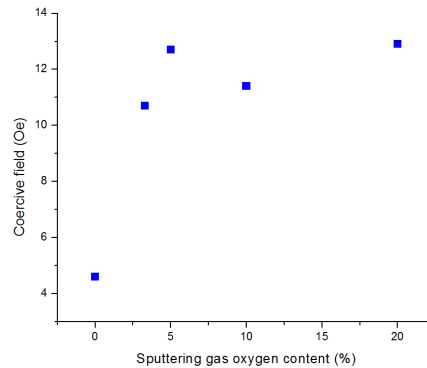
Figure 4.16: Coercive field of YIG as a function of oxygen growth content. Samples were annealed in a nitrogen atmosphere. No oxygen content gives a much lower coercive field indicating a considerable difference in stoichiometry of the as sputtered material.

YIG samples annealed in air are considerably different. The VSM hysteresis loops show that the YIG is very soft. The coercive field is as low as 0.1 Oe indicating high epitaxial crystal structure. Such a narrow loop is at the limits of the field sweep resolution. The coercive field is also shown to change as a function of thickness and it is seen there is only a small increase as the YIG is made thicker at 280 K. In the low temperature region the difference becomes much wider for thin YIG.

As the temperature is decreased the coercive field is found to become larger as shown in figure 4.17. The coercive field in the low temperature region is used to define the minimum field required to saturate the magnetisation when performing transport measurements. Rotating the sample keeping the applied magnetic field in the plane of the film showed little difference depending on orientation. It is possible that there is a hard axis defined in the film. This could be a result of a weak applied field during annealing as the coercive field is comparable to the earths magnetic field or any created by the heating coils of the tube furnace.

The magnetisation is found to approximate to bulk for thick films over 200 nm. Below this thickness the total moment is reduced and this becomes more prominent at low temperatures as seen in figure 4.18. This deviation is an important issue to resolve as it could have serious consequences for the spin current that can be injected into it.
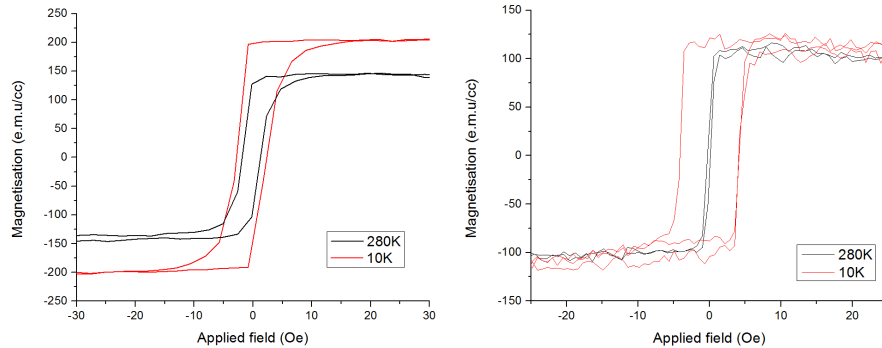
(a) Hysteresis loops on 250 nm thick YIG (b) Hysteresis loops on 45 nm thick YIG

Figure 4.17: Coercive field temperature dependence for YIG showing a clear widening of the coercive field at low temperatures for the two films. The magnetisation increase for the thick film is as expected but the thin film does not show this trend.

Combining this trend with the images of the interface seen by TEM we believe that the source of this reduction of magnetisation is at the YIG/GGG interface. The main reason for this being studied is that the SHMR in platinum has a similar downturn at approximately 100K. This lead to the idea that there could be a connection between them however as will be seen in chapter 5 the YIG thickness does not change the temperature dependence of the SHMR.

The magnetisation has also been found to be below the bulk value on some samples prepared by the standard recipe. towards the end of this work the sputter rate began to become erratic and increasing. The result of this was large surface roughness. To correct for this a new YIG target replaced the old which had become considerably thinner due to the amount of use. Films sputtered from this target have consistently shown reduced magnetisation even on thicker films. The cause of this is yet to be determined with possible explanations being that the stoichiometry of deposition or the quality of the target possible causes. This was measured with a SQUID-VSM as shown in figure 4.19.

GGG paramagnetism made the determination of the out of plane magnetic proper-
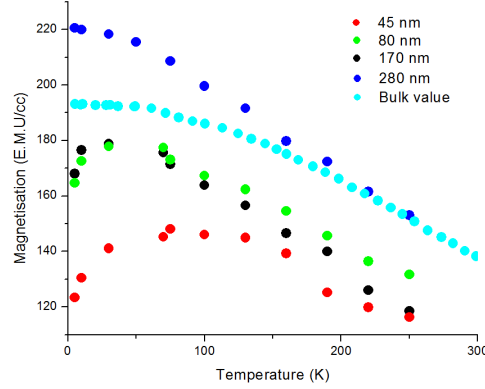
Figure 4.18: Temperature dependence for the saturation magnetisation for different YIG thicknesses. The downturn at low temperatures cash be seen to be related to the film thickness with the thinner films exhibiting the largest deviation from the bulk trend. Bulk value data taken from [132].

ties hard to obtain good data for. The magnetisation of the sample in this orientation takes a linear dependence with applied field the same as the paramagnetism. Separating these two could not be accurately distinguished however this would not be a problem for YAG substrates. As the out of plane saturation field cannot accurately be measured by magnetometry and so is estimated by the demagnetisation factor used in equation 4.1. For a thin film the in-plane factor is 0 and out of the plane is 1. Using the magnetisation of the bulk YIG gives the potential minimum applied field needed. Examples from the literature are shown in figure 4.20.

$$\mathbf{B} = \mu_0(\mathbf{H} - \mathbf{N_d}\mathbf{M}) \tag{4.1}$$

The literature does contain some measurements like this but without a detailed description of how it was accomplished. From these we see that the saturation field is in keeping with our theoretical limit.

Measurements of YIG grown on YAG show a difference to the GGG substrate. The coercive field is much wider despite being annealed in oxygen. From this is likely that the widening of the coercive field is due to defects and not because of reduced oxygen content. If the granular nature of the surface continues into the bulk of the material then this would explain the results. Further TEM investigation on one of these
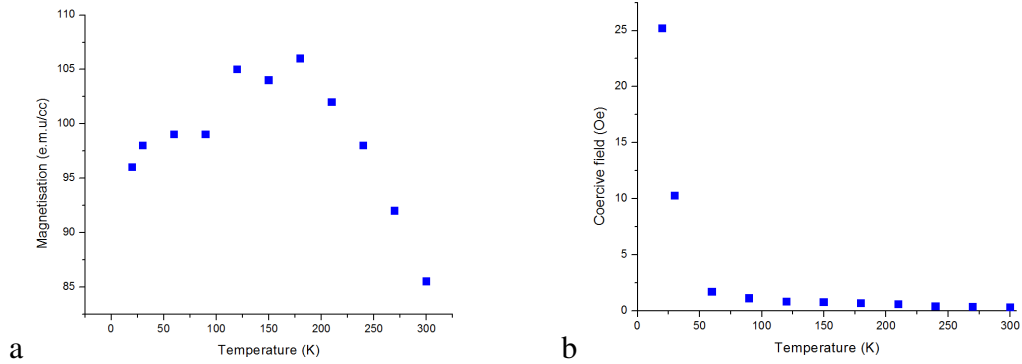
66

Figure 4.19: SQUID VSM measurements of YIG magnetisation at different temperatures with a deviation from the bulk trend at low temperatures **(a)**. Coercive field as a function of temperature widening at lower temperatures as expected **(b)**.
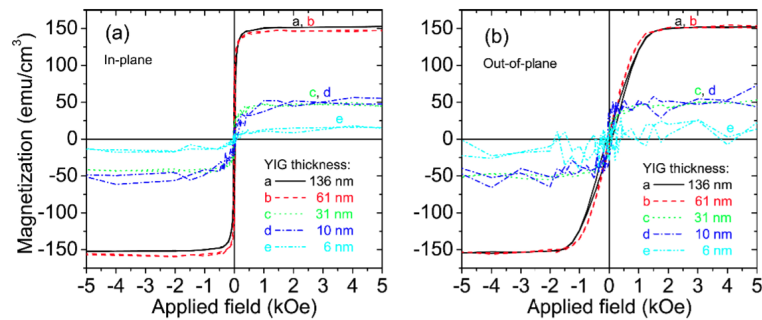

Figure 4.20: Hysteresis loops taken on variable YIG thicknesses. They show a very small coercive field consistent with our data and a deviation from the bulk value on thinner samples. Data taken from [133].

samples could confirm this. The magnetisation is also different. It is below the bulk value that is expected. Its temperature dependence however does not show a downturn in magnetisation at low temperatures.

In conclusion we have shown that the YIG is magnetic with a low coercive field. The saturation point tells us the required magnetic field needed to conduct SHMR experiments. The downturn in magnetisation for thin YIG at low temperatures is not fully understood and is currently being studied in a parallel project. The current belief is that a thin layer at the bottom of gadolinium iron garnet (GdIG) as the gadolinium switches place with the yttrium [134–137]. This would give rise to a thin region at

the substrate interface where the magnetic behaviour does not follow that of YIG and explain the downturn in magnetisation. This is also consistent with the downturn being thickness dependent as a fixed layer at the bottom would have a reduced effect on the total magnetisation of thicker films. However we do not believe that this has any significant impact in the SHMR work in this thesis as this effect happens at the top interface.

4.2.2 Crystal properties

The intensity of the $<444>$ peak from the YIG increases with sample thickness as expected as shown in figure 4.21. Calculated lattice constants are given in table 4.3
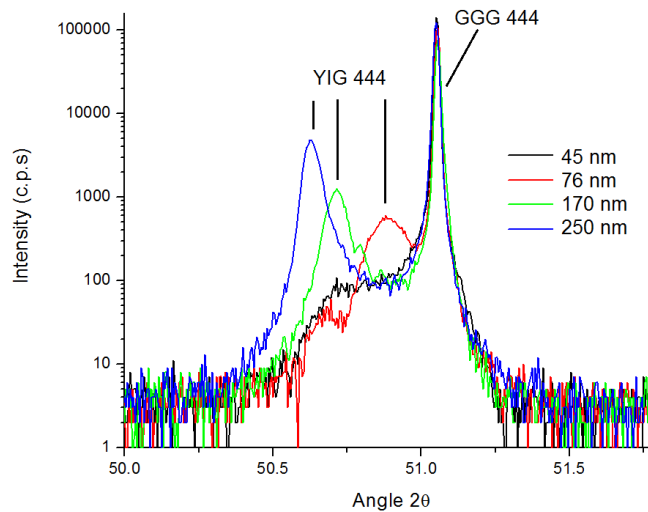
Figure 4.21: High angle XRD scan of YIG films of different thicknesses after annealing. The intensity increases with thickness as expected but the peak is found at lower angles for the thicker films indicating there is a change in the strain.

YIG thickness	Lattice constant
Bulk value	12.376 Å
45 nm	12.447 Å
76 nm	12.423 Å
170 nm	12.461 Å
250 nm	12.466 Å

Table 4.3: Lattice constants for different thicknesses of YIG.

The location of the peaks due to YIG are not as expected from the accepted value of the lattice constant. This indicates a strain on the crystal that varies with YIG thickness. This drift of the peaks to the left implies that the films have strain that is expanding the crystal structure out of the plane. This is also seen in the literature including films that are prepared by LPE indicating strain in the film [87; 88].

The thinner samples also have peaks that are broader than expected and the 76 nm sample appears to have a double peak. This indicates that the YIG structure is different at the interface to the bulk material above it. It does also offer some evidence for a magnetic dead layer that is made from diffusion of the substrate elements across the interface forming an intermediary garnet material. GdIG has a lattice constant of 12.470 Å which could explain the location of the YIG peak being at a lower angle than expected [135; 136]. This peak offset is seen in the literature for sputtered films [138; 139]. As the thickness increases we would however expect the peak to move to a higher angle where it should be for the bulk value. The reason this is not seen remains to be explained. Some individual films also exhibited Laue oscillations. These oscillations indicate that the films are exceptionally smooth and has also been seen in the literature, however these are only seen when the films are grown by off-axis sputtering [139]. Figure 4.22 shows these Laue oscillations on a 75 nm thick YIG film. This explains why only a few individual samples exhibit the Laue oscillations and are likely the result of a misalignment during growth.
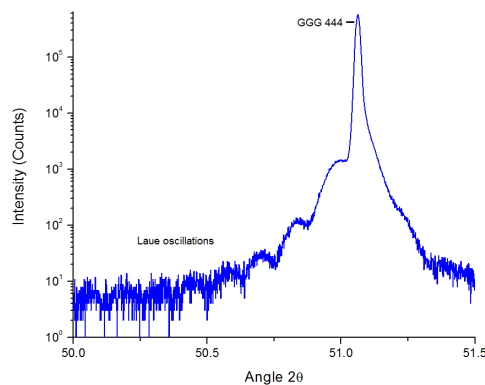

Figure 4.22: High angle XRD scan of 75 nm thick YIG film showing Laue oscillations. These were not seen in most films suggesting this was an abnormally smooth sample.

4.3   Transmission electron microscopy

YIG samples were prepared for TEM by both methods described in chapter 3. These had sheet metal grown on top instead of wires to ensure the metal is found where the sample is made thin enough to be transparent to the electron beam. The YIG structure is shown in a range of bright field images on samples prepared throughout the research project. Each of these images are similar indicating the consistency of the garnet structure. A clear regular pattern of atoms in the YIG matches well with that seen in the substrate layer. This matching is seen in the literature and no large scale defects have been seen on any images taken illustrated in figure 4.23. All of these samples were annealed but some were not subject to acid etching. This etching shows no difference to the crystal structure of the main bulk of the material.
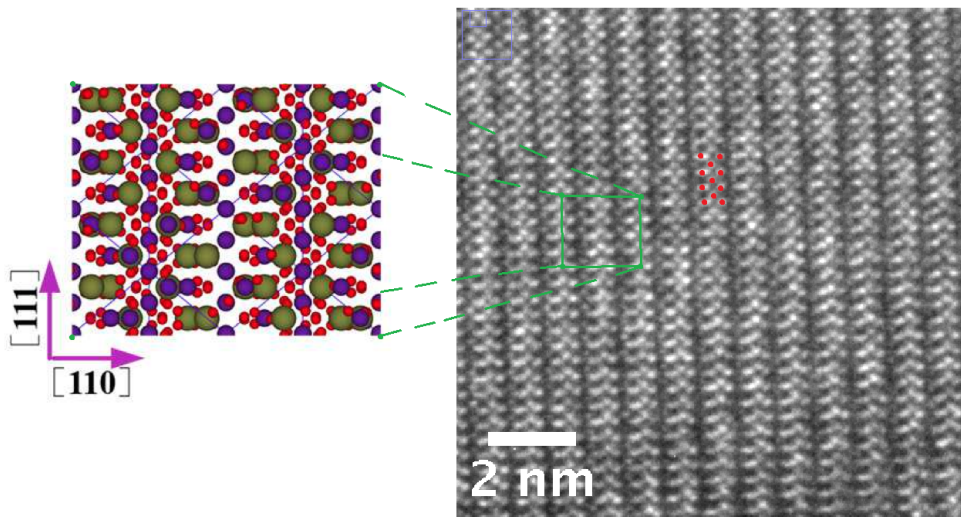
Figure 4.23: Bright field image of YIG structure. The red dots show the signature cross pattern of atoms matching with the known garnet structure seen in the model on the left. Comparative diagram taken from [140]

Figure 4.24 shows the sample where the hole is made during preparation. Surrounding the hole there is a region that has no clear crystal structure indicating damage by argon ions. This effect is substantial and a reason why ion milling the YIG/NM interface was not extensively studied.

Figure 4.24: Bright field image of YIG structure where the hole is made. The ion milling is shown to damage the YIG crystal structure around the edge of the hole.

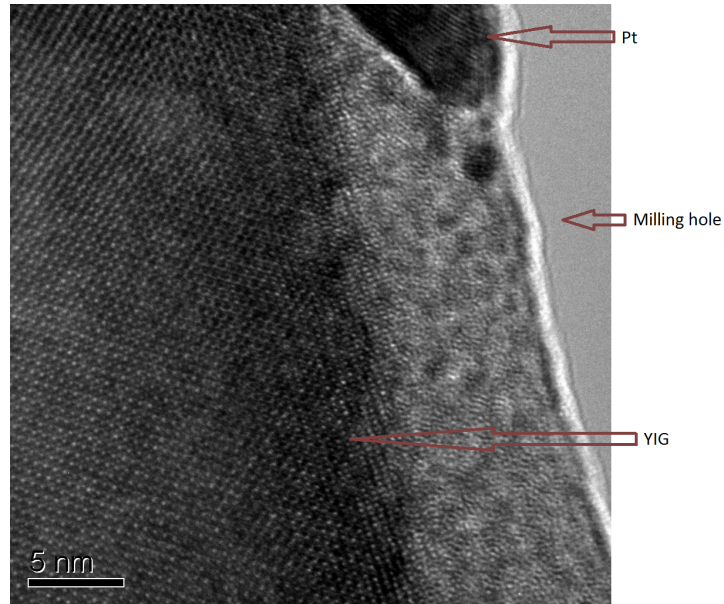### 4.3.1 GGG/YIG interface

A detailed study of the GGG/YIG interface is difficult to do by bright field images as the structure matching makes it difficult to distinguish between the layers at high magnification. This is seen in figure 4.25 with the colour contrast defining the two regions. The blue line indicates the 111 crystal axis. This line is matched by a regular pattern of atoms that crosses the interface without change. High angle annular dark field (HAADF) imaging has a sharp contrast on the material density and so this shows the different regions much better. This is used to focus in on the region so that a bright field image can be taken. Along this interface a series of dark patches are found all along the material shown in figure 4.26 and 4.27. EDX linescans were taken across both the dark and light regions of the interface to map the density of different elements. The line on the HAADF image represents the position shown in the linescan data.

These line scans show that there is a region of approximately 10 nm where the elements from both the YIG and GGG are found to coexist. The resolution is not high enough to say how much diffusion of these atoms is present but it is in keeping with
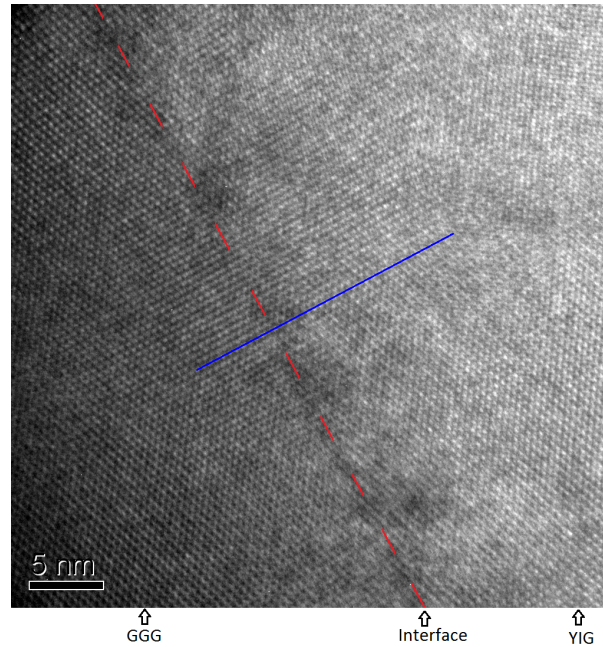
Figure 4.25: Bright field TEM image of GGG/YIG interface marked by the red line that is hard to distinguish under high magnification. The blue line indicates the <111> crystal axis normal to the plane as expected.

the possibility that there is a GdIG layer in-between the other two garnets. Comparison between the light and dark parts of the interface shows no obvious difference and so we believe these could be regions of strained material or voids where there is a lack of material. Further investigation of this part of the YIG still needs to be undertaken in particular a proposal has been made to investigate it by polarised neutron reflectometry (PNR).

4.3.2 YIG/NM interface

The YIG/NM surface is found to be smooth as expected from AFM measurements. Acid etching is shown to have removed some regions of the YIG that have defects in as seen in figure 4.28. The un-etched sample on the right shows regions on the surface where there appears to be atoms missing leaving dark patches. This was not seen on samples subjected to etching such as the image on the left. This shows that the incomplete garnet regions are removed by the etching process leaving only the

Figure 4.26: Data taken across a dark region of the YIG/GGG interface. **(a)** HAADF image showing the line used for the EDX scan that is shown in **(b)** mapping the elements across the interface with an overlapping of the elements from the two regions.
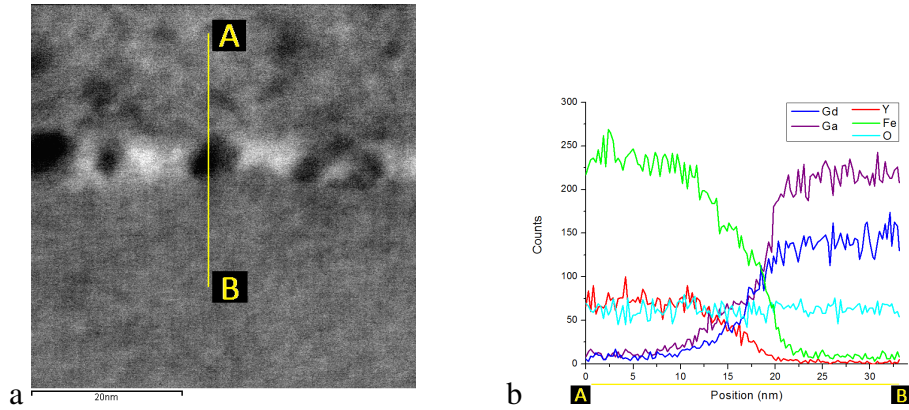

Figure 4.27: Data taken across a bright region of the YIG/GGG interface. **(a)** HAADF image showing the line used for the EDX scan that is shown in **(b)** mapping the elements across the interface with an overlapping of the elements from the two regions.
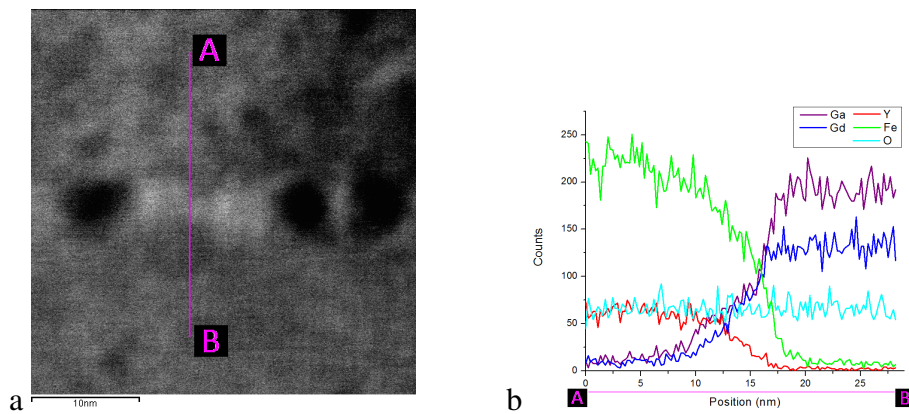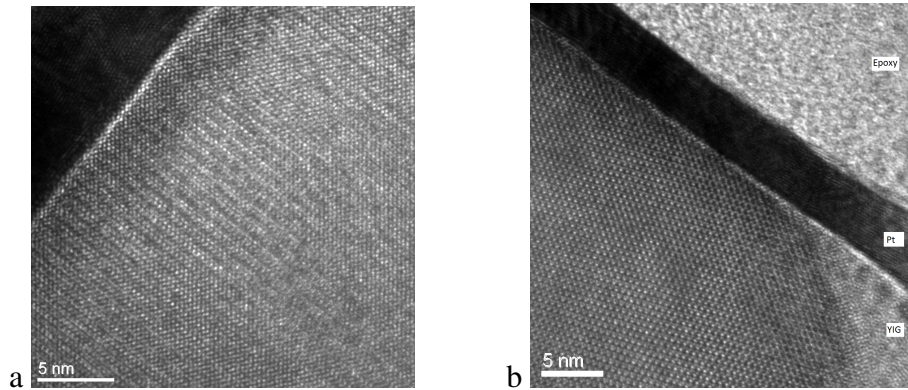
73

complete structure at the interface.

Figure 4.28: Bright field images of the YIG/Pt interface. The etched YIG in (a) maintain the garnet structure at the Pt interface but the un-etched YIG in (b) has dark regions that may have missing atoms.

On some later samples it was found that the etching was not needed to improve the SHMR and the reason can be seen in the bright field images of twin samples in figure 4.29. Here we see identically prepared YIG with one sample etched and the other not. No defects in the crystal can be seen in either sample which supports the idea that the interface between the YIG and metal has to be sharp without any other material between them. The etched sample on the left does however show some surface roughness which we attribute to a particularly aggressive acid treatment. It is not fully understood why this particular batch did not need etching to be successful. One possibility is that the stoichiometry is sufficiently close to the requirement that full crystallisation of the material was possible without any excess of any element that forms a different structure on the top interface.

Across the YIG/NM interface there is some evidence of iron contamination in the tungsten. The HAADF image in figure 4.30 with the tungsten in the white region and the YIG below. The EDX scan across the interface shows a spike in the iron content represented by the green line at the 8 nm position. The tungsten shown by the black line indicates that this is inside the tungsten region. This does need further investigation as the sample can drift in the beam and the exact amount of iron needs to be determined if
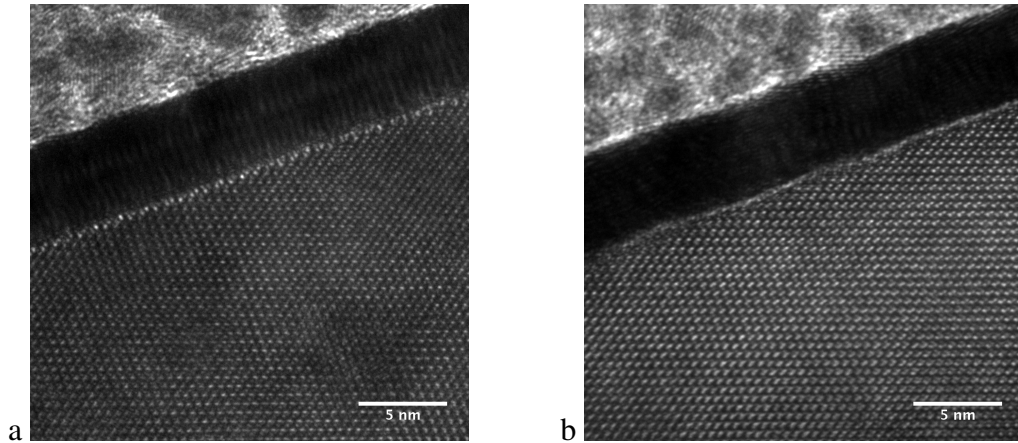
Figure 4.29: Bright field images of YIG/W interface. Here the etched sample, (b), has some surface roughness not present in the un-etched sample (b).

it is present in the platinum. There is no EDX evidence of its presence in the platinum. The scans show the expected decay of the YIG elements being replaced by the tungsten as the interface is approached. The transition is not sudden due to the finite size of the sample area and could explain this iron increase.
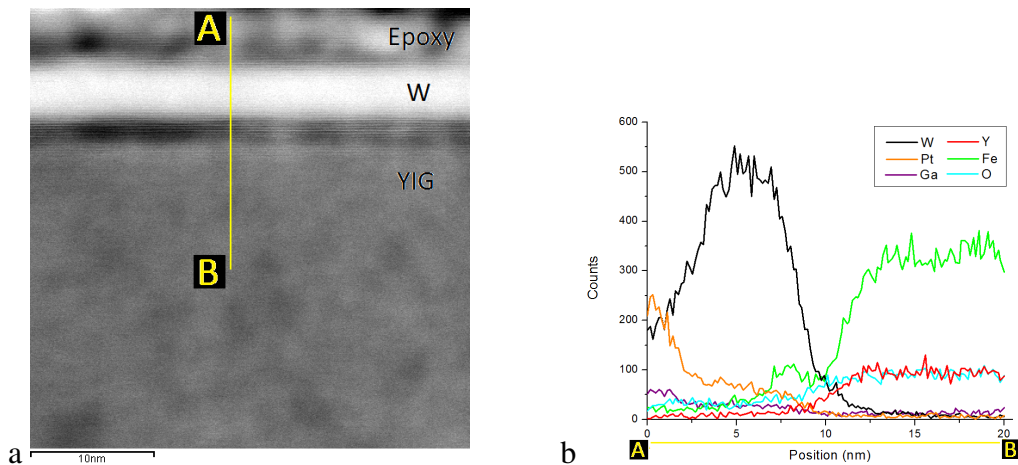
Figure 4.30: HAADF image of YIG/W interface. **(a)** EDX line shown on HAADF image. **(b)** EDX data across interface. We see a small increase of iron content in the tungsten layer suggesting possible contamination.

The location of the elements was studied over a two diminutional area by STEM mapping. In particular this is used to look at the oxygen content as this is fundamental

to the magnetic exchange interaction in the YIG. An example of this is shown in figure 4.31. We see the different metals of the YIG and substrate are as expected. The measurement is insufficient to be able to prove diffusion of the metals between the interface if it is only present in a thin region. It does show no large scale contamination however. The oxygen content between the regions is found to be sufficiently close that the interface cannot be determined. This is as would be expected as the oxygen density in the two garnets should be identical.

(a) HAADF image   (b) Gd   (c) Ga

(d) Y   (e) Fe   (f) O

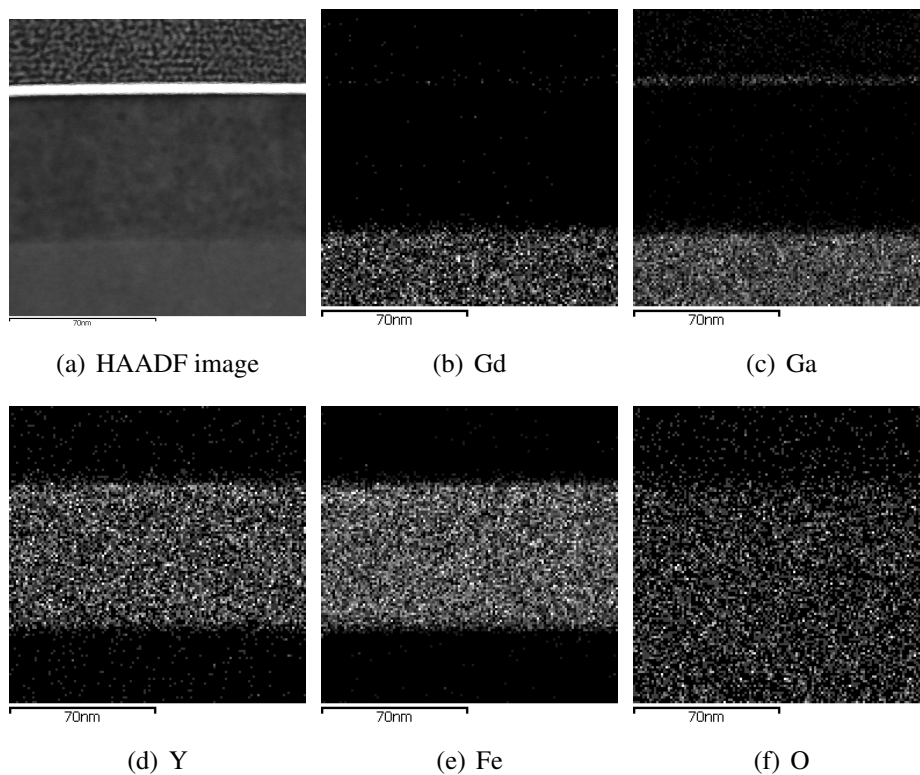Figure 4.31: STEM mapping of the elements on a GGG/YIG/Pt sample. (a) shows the dark field image of the region being scanned and (b)-(f) show the density of the elements. Clear bands can be seen corresponding to the YIG and GGG layers with little diffusion between them.

The acid etching process removes any non-magnetic material from the YIG surface to improve spin mixing conductance. A similar improvement has been shown in the
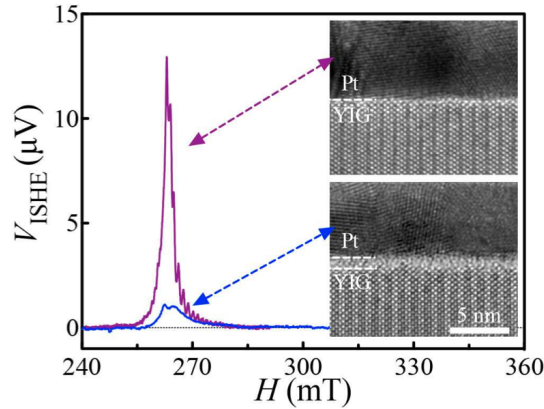
Figure 4.32: Bright field TEM images of YIG/NM interfaces demonstrating the importance to spin mixing conductance. The voltage shown is produced by FMR spin pumping into platinum. Taken from [140].

literature that gives a large increase in the spin mixing conductance as seen in figure 4.32 [140]. The YIG sample was heated *in situ* to promote surface re-crystalisation before the platinum was deposited. This made the crystal structure of the YIG be maintained all the way to the platinum instead of a gap in the untreated sample. The thin band between the YIG and platinum is still present on the TEM images of the etched YIG but is thinner. The crystal structure itself is also in good agreement with our samples and matches the known garnet structure.

The metals themselves do not show any clear structure. The platinum does have some indication for crystallisation but it is not in a consistent order. Faint lines can be seen in the bright field images which are in agreement with an XRD scan on sheet platinum. This showed a small <111> platinum peak. The tungsten is without any structure also as expected indicating that is in an amorphous phase. Resistivity measurements on the tungsten prepared for TEM were all of the amorphous type as well. No TEM measurements were taken on tungsten that behaved like a normal metal. For the tungsten to be in its β phase we would expect to see a porous material that grows in a column nature. As no evidence for this is seen we conclude that the material is amorphous.

4.4   Ferromagnetic resonance

FMR is a standard technique that is used to probe the spin dynamics of a ferromagnetic material. The magnetisation vector of an electrons spin is known to precess around an applied magnetic field at the Larmor frequency [141; 142]. When the magnetic material is subjected to microwave radiation of the same frequency it absorbs energy that allows the electrons to transition to a new energy level that has the opposite spin orientation. This absorption is measured to determine the Larmor frequency and its linewidth. The technique can also be used for spin pumping into a NM that is in contact with the magnetic material. As this is similar to the SHMR where a spin current is injected from one material to the other. As a result it can offer information about the spin mixing conductance at the interface. The YIG recipe used in this research has been used for FMR work by collaborators at the University of Exeter. Examples of the work are shown in figure 4.33.
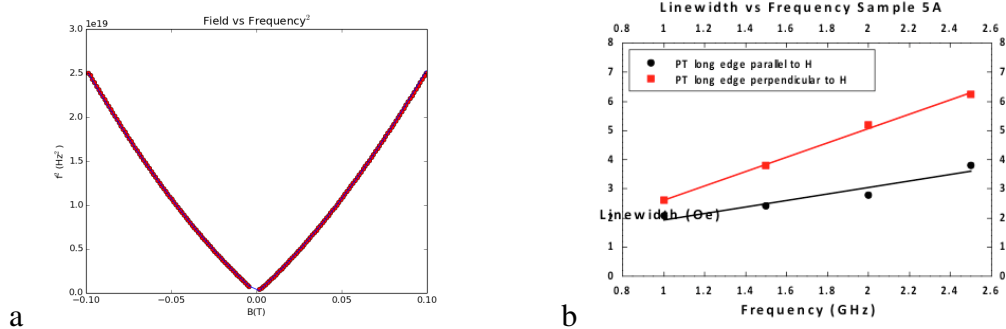
Figure 4.33: **(a)** Frequency vs applied field for 45 nm thick YIG film with a clear fit to the Kittel equation. **(b)** Linewidth of the YIG vs frequency in agreement with the expected values found in the literature.

The Larmor frequency is shown to change with applied magnetic field as expected by the Kittel equation [143]. The linewidth is found to be small reaching as high as 6 Oe for a frequency of 2.5 GHz. Results from the literature show that this is in the expected range of 0.6-10 Oe [144; 145]. The small line width is indicative that the YIG has very low microwave loss and low Gilbert damping which is expected for high quality YIG. The results of these experiments are still to be completed and await publication and so shall not be discussed further in this thesis.

CHAPTER 5

Spin Hall magnetoresistance in platinum

5.1 Resistivity

5.1.1 Growth parameters

Platinum wires were deposited by sputtering using the masking technique described in chapter 4. A power of 9 W and an pressure of 2.4 mTorr yielded a typical growth rate of 1.6±0.1 Å/s. The wires are 200 μm wide and 3.5 mm long. These dimensions are used to convert resistance measurements into resistivity. To ensure accuracy of the conversion factor these wire dimensions were studied and the thickness carefully calibrated. Individual wires on YIG samples where there are multiple thicknesses of platinum is difficult to do by XRR. This is due to the small surface area compared to the footprint of the X-ray beam. Calibration sheet films were grown for each sample batch so an estimate could be calculated. To confirm that this rate is applicable for the wires, a set was studied more closely. Four wires grown simultaneously on silicon substrates were measured by XRR and compared with the sheet film.

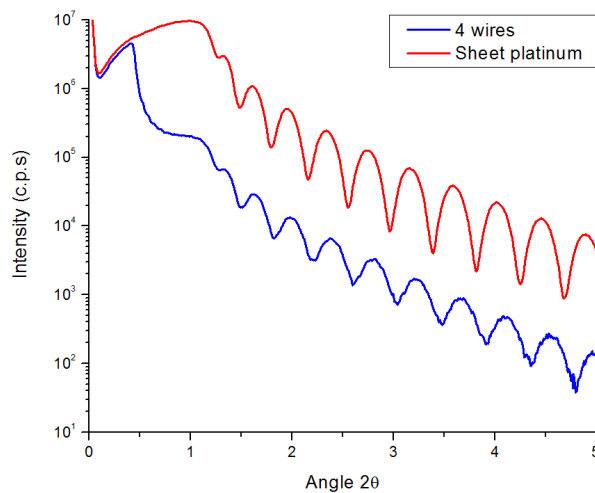Figure 5.1: XRR thickness measurements of platinum wires in comparison to sheet film. The difference in resolution and intensity is due to a smaller surface area of the wires.

These results give thicknesses of 19.5±0.5 nm and 19.1±0.2 nm for the sheet film and four wire samples respectively. The profilometer scan on one of the wires was found to be in agreement with a thickness of 19±1 nm. The profilometer also shows

some minor evidence for the shadowing effect of the mask that reduces the thickness of the wire but only in a narrow region at the edges. Other edge effects can be seen by SEM in figure 5.2. The edge is not perfectly straight as a result of imperfections in the mask shape. One mask was found to have serious indents at some places and so these samples had to be regrown. As a result each wire measured was checked carefully by microscope to ensure a good rectangular wire geometry.
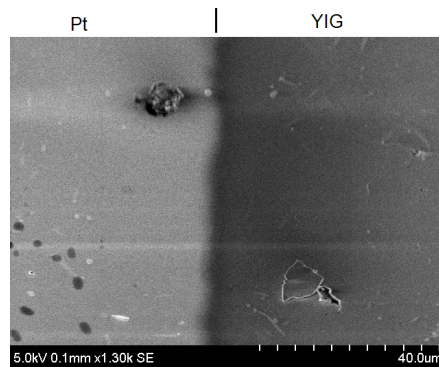
Figure 5.2: SEM image of platinum wire on YIG at 1300 times magnification. The edge of the platinum is not straight and has some rough edges due to imperfections in the mask used during sputtering.

To measure the wire resistance the four probe method is used with a current of 100 μA. This was found to give a good signal to noise ratio without causing sufficient Joule heating to change the wires resistivity. The contacts were made by aluminium wire bonding onto the platinum wire and measuring the length between the inner voltage probe edges with a travelling microscope. This length is then used with the thickness calculation and known width to give the conversion factor to measure the resistivity. The resistance was measured using the average of 10^4 voltage measurements with forward and reverse currents.

Sheet films of platinum on GGG were also used to study the crystal nature by XRD. As the intrinsic mechanism of the spin Hall effect is based on a periodic lattice we expect this to be an important factor in the size of the SHMR. The XRD scan shown in figure 5.3 indicates a peak for the platinum which corresponds to the <111> plane

in the FCC structure as expected. From this data a lattice constant of 3.918±0.002 Å is extracted in comparison with 3.924 Å for the accepted bulk value [146]. The gaussian fit from the insert was used to calculate the FWHM as 0.326°. The scherrer equation is given in 5.1 to calculate the grain size τ.

$$\tau = \frac{K\lambda}{\beta cos\theta} \tag{5.1}$$

The FWHM is given by β, K is a shape factor close to unity, θ is the Bragg angle and λ is the X-ray wavelength. From this a grain size of 25.9 nm is extracted. It is also interesting to note that the platinum appears to be matching with the orientation of the GGG substrate. The lack of any other peaks indicate that this structure is uniform however there could be other undetected peaks due to the low intensity. TEM images also indicate the presence of layers in the platinum parallel to the GGG surface.
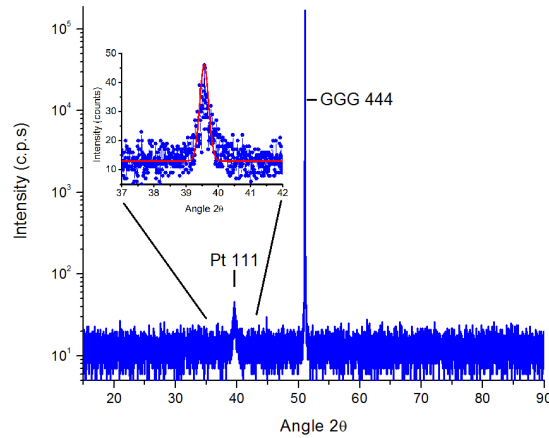
Figure 5.3: XRD scan on 64 nm thick sheet platinum on GGG showing the presence of the <111> peak. Inset shows the detailed platinum peak with a gaussian fit highlighted in red used to calculate grain size.

5.1.2 Thickness dependence

The resistivity of the platinum measured as a function of thickness has shown that the surface scattering plays a dominant role in the thin wires that are used for measuring the SHMR. Several other factors affect the resistivity such as the surface roughness and defects in the platinum structure [147–149]. To minimise this the samples used for

the SHMR study in this section were all done on YIG films prepared by the standard recipe and were found to have low surface roughness. The dominant effect is the surface scattering that is described by the Fuchs-Sondheimer model. This raises the resistivity well above the bulk value of 10.6 $\mu\Omega$cm (at 300 K)[47; 150; 151]. We see a sharp rise in the resistivity of platinum up to an order of magnitude over this bulk value in figure 5.4. The fits to this model yield a bulk resistivity of 53.2$\pm$0.5 and 30.7$\pm$0.5 $\mu\Omega$cm at 297 K and 5 K respectively. As these are both well above the bulk value we can conclude that the platinum is not single crystal but a polycrystalline material with many defects and small grain size. This is in agreement with the TEM images of the platinum where some evidence of structure exists but not of high quality epitaxial order. The platinum peak in figure 5.3 is also weak. The mean free path was calculated to be 3.1$\pm$0.1 and 6.9$\pm$0.1 nm for 297 K and 5 K respectively.
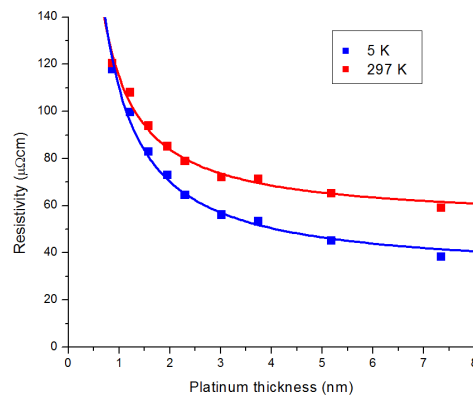
Figure 5.4: Platinum resistivity as a function of thickness. Performed at 297 K and 5 K with fits made to the Fuchs-Sondheimer equation. From these fits the bulk resistivity was calculated.

To ensure a continuous layer of platinum is deposited no samples were made thinner than 0.8 nm. It was found that the resistivity of platinum grown on YIG using YAG as a substrate is less than 2% higher than on GGG. This is attributed to the surface roughness seen in the previous chapter. The resistivity data are shown in figure 5.5

At low temperatures the platinum grown on YIG exhibits an upturn in resistivity that is dependent on thickness. This upturn is found in metals with magnetic impurities
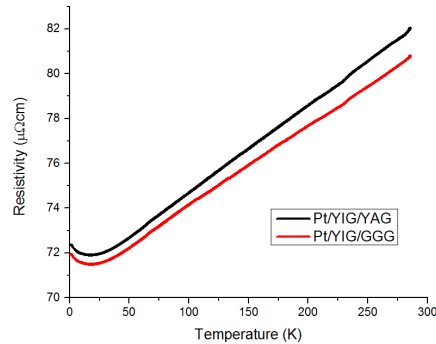
Figure 5.5: Resistivity as a function of temperature for 2 nm platinum on YIG showing the comparison between GGG and YAG substrates. The difference is small indicating the YIG surface roughness do not make a significant contribution to resistivity for these samples.

known as the Kondo effect [152; 153]. The cause of this cannot be an impurity in the platinum target however. For this to be the case the upturn would be independent of thickness. The data in figure 5.6 shows that the upturn increases dramatically as the thickness is reduced. The upturn is plotted against $\ln T$ in figure 5.7 showing a linear trend. The percentage increase between this minimum temperature and at 1.5 K is shown in figure 5.8. The minimum in the resistivity is found at a higher temperature as the thickness is reduced.

(a) 0.86nm Pt.

(b) 3nm Pt
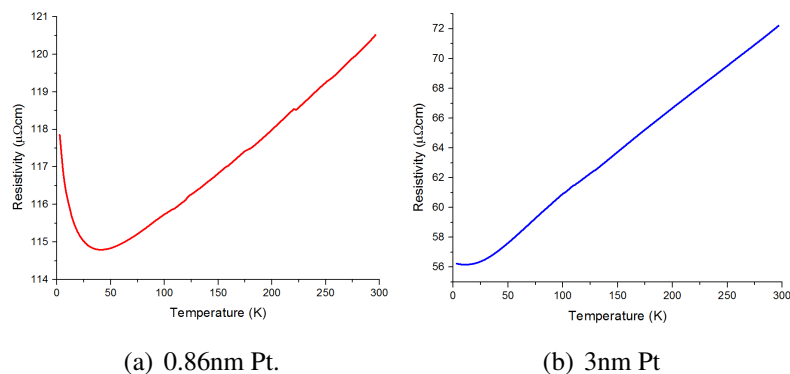
Figure 5.6: Resistivity upturn in platinum grown on YIG demonstrating the thickness dependence. The upturn is found to be much more significant for thinner platinum and starts at a higher temperature.

The implication is that if this is the Kondo effect due to impurities then the impurity must be at the interface with the YIG. This would be explained by iron from the YIG diffusing into the bottom of the platinum. Any loose iron atoms left on the surface after annealing or etching is unlikely as the final cleaning stages should remove this. It could also be evidence of magnetic proximity effect [154]. A thin layer of the platinum becoming magnetic at the interface of the YIG could have a similar effect to iron impurities or there could be atomic diffusion of iron into the platinum.
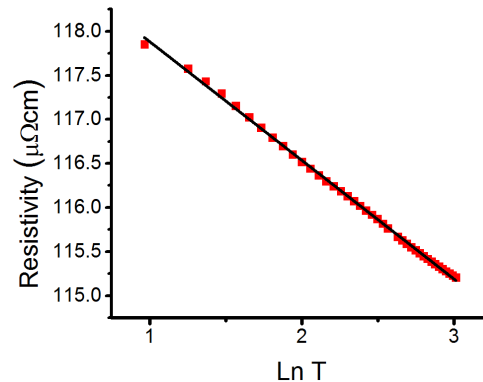

Figure 5.7: Resistivity plotted against Ln T for 0.86 nm Pt in the low temperature region. The linear fit in black that is consistent with both Kondo impurities and localisation effects as possible explanations for the resistivity upturn.

Another possibility can be given by the surface roughness. Despite the interface being very smooth the roughness that does exist becomes significant when the thickness of the platinum approaches 1 nm. Small undulations of the YIG that protrude into the platinum could influence the conduction electrons in a similar manner to a magnetic atom alloyed with the platinum directly. The cause of this upturn is not conclusively proven and so requires further study to determine its origin. The effect of this on the resistivity is only relevant in the low temperature region. A more convincing argument for the resistivity upturn is the localisation effect. This effect is seen in ultra thin films and is caused by electron-electron scattering in a two dimensional system [155; 156]. Figure 5.7 shows a linear trend that demonstrates that the upturn is logarithmic with a gradient of -1.35. This logarithmic relation is consistent for both the Kondo effect

and electron-electron localisation. The thickness dependence of this follows an inverse square relation so the upturn increases as the wire becomes thinner. From figure 5.8 (b) we see this trend matches our experimental data. This is in contrast to the Kondo effect which would be independent of sample thickness unless the magnetic impurities arise from atomic diffusion from the YIG into a thin layer of the platinum.

| (a) | (b) |
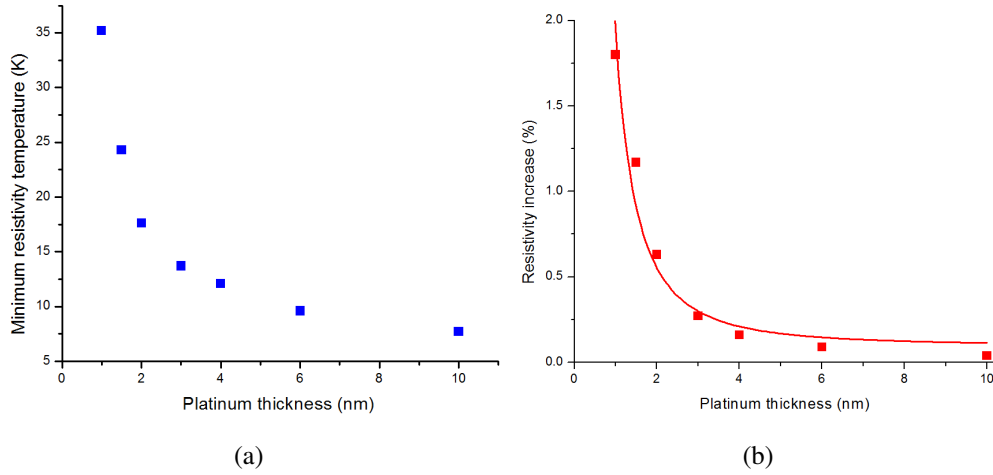
Figure 5.8: Temperature of the minimum resistivity as a function of the platinum thickness (a). Resistivity increase from the minimum value to 1.5 K (b) fit indicates an inverse square dependence.

5.1.3 Temperature dependence

The general shape of the platinum resistivity follows what is expected for a NM above the low temperature Kondo like upturn. This linear temperature dependence was seen in all platinum grown. The change in resistivity over the 1.5-300 K temperature range is shown in figure 5.9. This is relevant to the SHMR as it makes an important fitting parameter. We define the residual resistivity ratio (RRR) as the resistivity at 297 K divided by the minimum resistivity for the individual wires. This represents the resistivity change in the region where NM behaviour is observed that is dominated by electron-phonon scattering.

$$RRR = \frac{R_{297K}}{R_{min}} \tag{5.2}$$
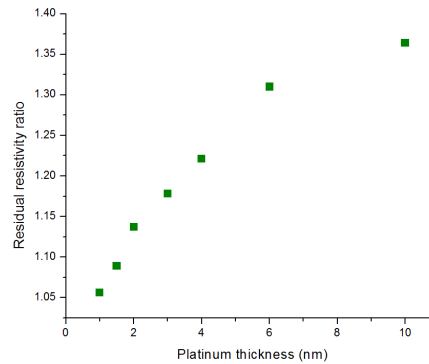
Figure 5.9: Residual resistivity ratio change as a function of platinum thickness. As the thickness decreases the dominant component of resistivity comes from surface scattering which is temperature independent resulting in a small RRR.

As we can see from figure 5.9 the RRR increases with the platinum thickness. The bulk value will not be reached for platinum that still exhibits SHMR that is large enough to be measured. All platinum made on this project followed the correct NM temperature dependence The change in the RRR is small in comparison to the percentage change in the SHMR over the same temperature range. As the resistivity directly contributes to the spin Hall angle in the SHMR equation, for a 10 nm thick wire we would expect a 62% change in spin Hall angle due to resistivity change. Below this thickness the percentage decreases dramatically.

5.2 SHMR properties

5.2.1 Angular rotations

The angular dependence was obtained by measuring resistances with the four probe method. Resistance measurements are taken at regular angular intervals at a stable temperature and a current of 100 μA. Changing the current was found to make no difference to the SHMR. Resistance measurements were taken in 5° steps with a 2 second pause between the sample moving and the next measurement taken. This helps to remove any noise due to the sample movement causing temperature fluctuations during rotation. The measurements were done in excess of 360° and repeated in both clockwise and anti-clockwise direction. The in-plane rotation angle is labelled α, and

the transverse and longitudinal out of plane rotations are given by angles β and γ respectively.
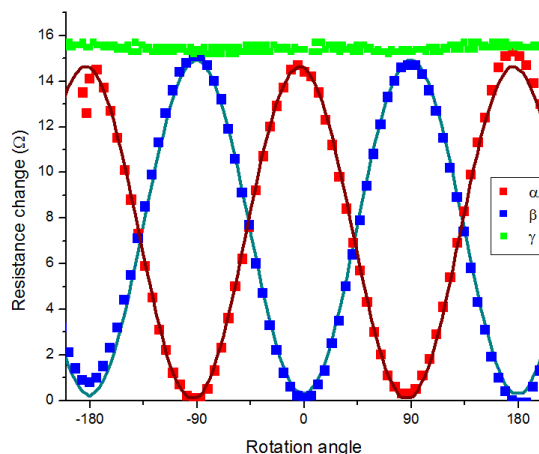
Figure 5.10: Resistance change of 0.86 nm platinum wire as a function of angle at 297 K and 0.1T applied field. The three different geometries show that a change is only measured in-plane and transverse out of the plane orientations.

From this the stability of the temperature could be tested to ensure that the amplitude is due to the SHMR. Samples were mounted in three different orientations. The rotations in two of these fit the $\sin^2$ shape expected by SHMR theory. Typical data for this is shown in 5.10. It can be sent that the resistance change is dependent on which angle that is made between the spin direction and the magnetisation direction as expected by theory. The rotation around γ shows no resistivity change where the angle between current and magnetisation changes. This angular pattern is found to be consistent at all temperatures measured.

The data in the first publication attributed to this work was not done in this way [157]. Field sweeps were used instead to determine the angular dependence which produced the data shown in 5.11. The field sweeps were done along the hard axis of the YIG. The size of the effect in this is much smaller that what is seen in the literature and its temperature dependence will be discussed later. The resistance begins to change at the applied field that corresponds to the saturation field of the YIG. The shape of the

resistance in figure 5.11 is not perfectly matched to the hysteresis loop data which indicates an issue with the magnetisation rotation when using a field sweep. The VSM data in figure 5.12 shows this piece of YIG has an in plane magnetic anisotropy. A basis angular rotation method was used to measure the in-plane SHMR and was found to be in agreement with the magnitude of the effect measured using the field sweeps.
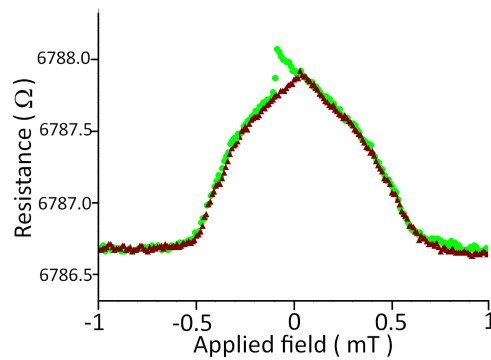
Figure 5.11: Field sweeps done on 2.5 nm platinum wire on 45 nm thick YIG at 250 K. The resistance change is used to estimate the SHMR of the platinum. The unusual shape demonstrates the limited use of field sweeps over angular rotations.
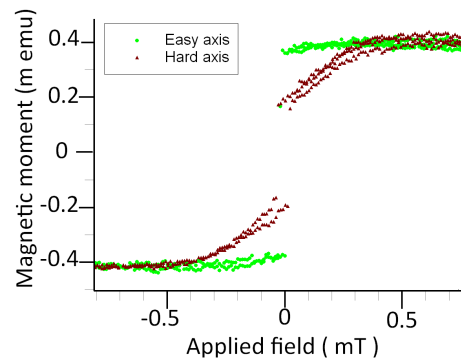
Figure 5.12: VSM data for the hard and easy axis of YIG used in figure 5.11 at 250 K. The saturation field of the loops approximately agree with the applied field that the resistance of the platinum becomes field independent.

The field sweep should reflect half the full rotation as the magnetisation. However the asymmetry in the YIG magnetisation suggests that at a low applied field the magnetisation axis rotates in the plane. The field sweeps were done along the hard axis to

promote this. The same method was applied to measuring the effect out of the plane to confirm the geometrical dependency matches the SHMR. The field sweeps also show that the resistance levels out after the YIG saturation field is exceeded. From this we see no significant effect due to the applied field strength meaning that any other magnetoresistive effects are negligible.
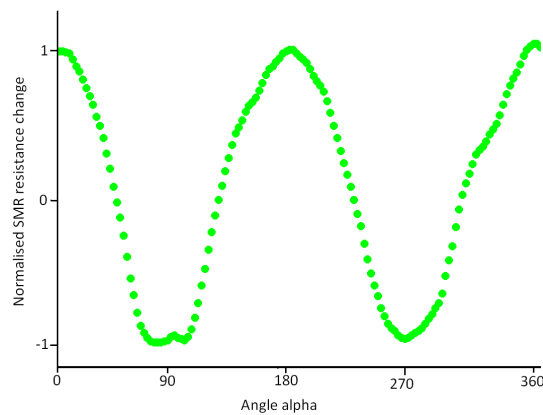
Figure 5.13: Angular rotation measurement on 2.5 nm platinum wire on 45 nm thick YIG at 297 K. The field sweeps were found to produce resistivity changes that match these rotations at room temperature and at 77K.

5.2.2 Field dependence

Metals exhibit magnetoresistance that is dependent on the strength of an applied field [158]. To determine the effect of this the angular rotations were done at a range of applied field strengths to determine how this impacts on the SHMR measurements. A minimum of 0.1 T was found to be the minimum field that will saturate the YIG at all temperatures. From the demagnetising factors the highest field required to saturate bulk YIG out of the plane is 0.27 T. For the out of plane rotations 0.3 T was used and compared with in plane rotations at the same field strength. The rotations were done at 297 K up to 3 T for different thicknesses of platinum. An increase in the height of the SHMR is seen in figure 5.14. As this difference is not due to the SHMR the total resistance change as a function of applied field strength is plotted in figure 5.15. This change is the sum of the SHMR and any other magnetoresistance effects.
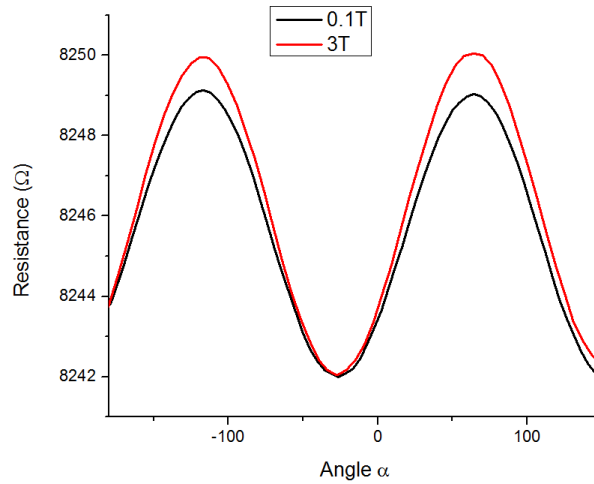
Figure 5.14: Angular in-plane rotations at 297 K on 1.7 nm platinum at 0.1 T and 3 T. As SHMR is field independent the difference between the measurements is due to other magnetoresistive effects.
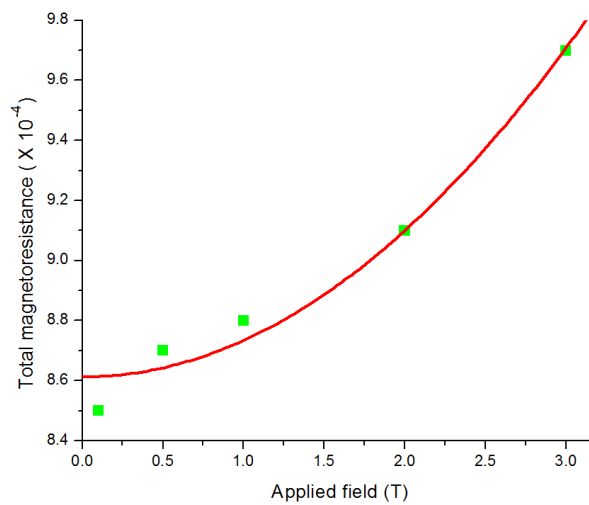
Figure 5.15: Total in-plane MR measured as a function of applied magnetic field. The fit in red assumes a squared field dependence due to other magnetoresistive effects in addition to the SHMR.

In figure 5.15 we see an increase in the total MR measured as the applied field is increased. The data can be fitted assuming a B^2 field dependence consistent with Kohler MR [158]. The SHMR theory does not require any directly applied field in

91

the platinum wire, only that the magnetisation direction of the YIG is saturated in the desired direction. As the intercept is finite we can therefore conclude that the SHMR is not due to any magnetic effects that are based on the strength of an applied field. This additional MR is something that is considered when choosing the applied field for the measurements. For this reason that the lowest possible field is chosen to rotate the YIG magnetisation direction.

5.3 Temperature dependence

5.3.1 YIG thickness dependence

As the SHMR injects a spin current into the YIG it is important to measure the effect on different thicknesses of YIG. If the SHMR is affected by the bulk magnetisation then the downturn would be expected to influence the effect. At low temperatures the magnetisation could be used to explain the downturn of the SHMR. To demonstrate this is not the case a series of YIG thicknesses with a 2 nm platinum wire on each were measured. These were grown and etched together to ensure consistency. The full temperature dependence of the SHMR between 1.5-300 K is given in figure 5.16. At individual temperatures we see a small variation between the different YIG thicknesses however there is no clear pattern. This indicates that above 13 nm the YIG thickness has no clear effect the SHMR value.

The small variations between each sample can be explained by small variations in the YIG surface quality and subtle differences in the platinum grown on each. The resistivity data for these are all similar. In terms of the SHMR theory the variation can be attributed to either the spin Hall angle, the spin mixing conductance or the effective interface area as a result of etching. The consistency of the temperature where the maximum SHMR occurs indicates that the spin diffusion length is not the cause. For the 13 nm sample the difference is greater which could be due to several reasons. The spin current may be saturating or even reflected back from the GGG interface and so suppressing the spin injection. Any GdIG in a different magnetic layer could also give a significantly reduced spin mixing conductance. Finally the YIG could also be etched by the acid enough to have dissolved through to the substrate in places
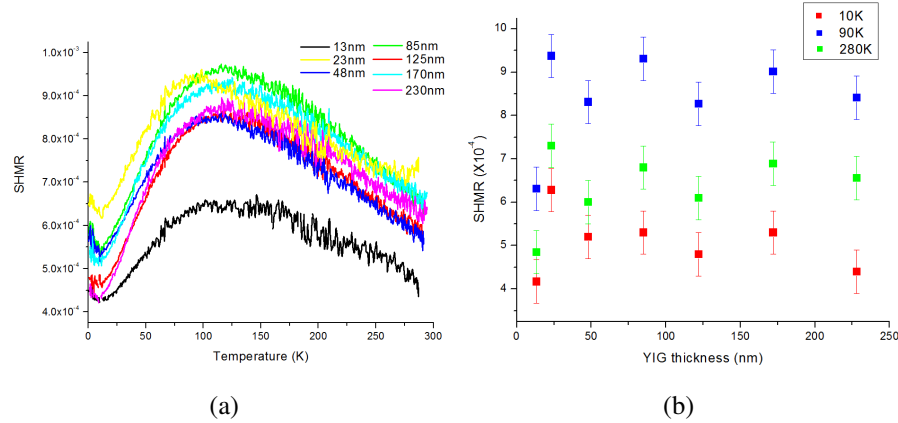
Figure 5.16: SHMR in platinum on different YIG thicknesses that all exhibit the same general shape (a). Values selected at several different temperatures in (b) show no clear pattern based on the YIG thickness above 13 nm.

and so reducing the effective surface area of the YIG/Pt interface. The temperature dependence shows no significant difference above this thickness in the region where the magnetisation experiences a downturn below 100 K. From this we conclude that the SHMR is not affected by the bulk magnetisation. The magnetisation is therefore expected to be bulk like at the surface and that the downturn is due to the bottom layer of the YIG. Beyond a certain thickness this layer does not influence the spin injection at the YIG/NM interface. The VSM measures the total moment from the whole sample. To conclusively prove that the magnetisation at the interface is bulk like will require an alternative measurement technique.

5.3.2 Field sweep temperature dependence

The first temperature dependence was determined from a study on a single 2.5 nm wire. This was an un-etched sample grown on 45 nm YIG film. The field sweeps done at each temperature are combined to give the temperature dependence shown in 5.17. The forward and reverse field sweeps show a close agreement. Here we see the same temperature dependence shape that had been reported in the literature but of a much smaller effect. This we attribute to the fact that the YIG was not properly etched. The fit to the data is done by assuming a constant spin mixing conductance

of 7.57 x 10^{14} $\Omega^{-1}m^{-2}$ and a spin diffusion length that is modelled by equation 5.3 where a and b were constants. The second constant is to put a residual limit on the spin diffusion length at 0 K similar to the mean free path. Fits without this constant were unsuccessful. This is based on the Elliot-Yafet mechanism as described in chapter 2. The spin Hall angle was also assumed to be independent of temperature and found to be 0.044±0.002.
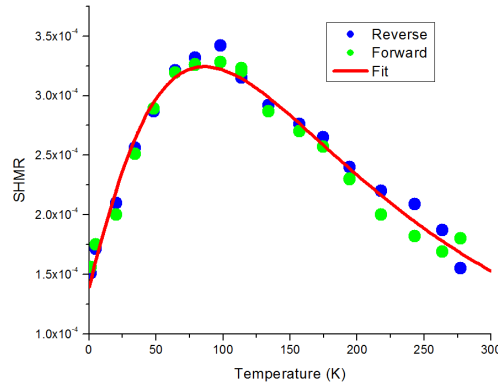
Figure 5.17: SHMR measured by performing field sweeps at different stable temperatures. The fit in red is made using EY spin diffusion mechanism showing a good match to the data across the full temperature range.

$$\lambda = \frac{a}{T + b} \tag{5.3}$$

From this fit we see that the model is in excellent agreement with the data. The fitting parameters are given in figure 5.19. The spin diffusion length is small at high temperatures in comparison to the values initially reported in the literature [154; 159]. Attempts to fit the data with a higher spin diffusion length were unsuccessful. The spin diffusion length also could not be modelled inversely proportional to the resistivity directly as the change over the temperature range is insufficient.

The spin mixing conductance and the spin Hall angle can be altered to produce a different fit. As the spin mixing conductance is reduced the spin Hall angle increases. Taking the extremes by modifying equation 2.27 gives the fits shown in figure 5.19. Here we see fits that are not as close matching with the data but still close enough to be unable to determine the exact value of G. The spin Hall angle we obtained is
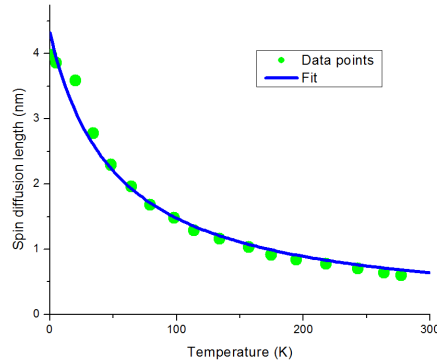
Figure 5.18: Spin diffusion length for platinum calculated from the fitted data. The blue fit is made using equation 5.3 using the optimum fitting parameters.
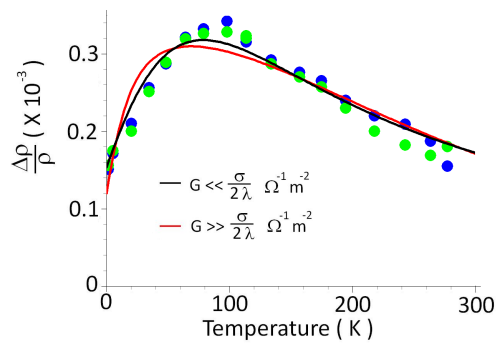
Figure 5.19: Extreme assumptions on the spin mixing conductance used to fit the SHMR. The small change in fit when the extreme limits of spin mixing conductance are used demonstrate the difficulty in extracting an exact value from the data.

considerably smaller than what was reported in the only other study at the time to estimate it which was between 0.075-0.11 [159]. The spin mixing conductance is in general agreement reported as 4×10^{14} $\Omega^{-1}m^{-2}$. The reason for the different spin Hall angle is the SHMR was measured to be much smaller. This was addressed by using acid etching to improve the size of the SHMR and will be discussed later in the chapter.

5.3.3 YIG on YAG

The temperature dependence of the SHMR was also measured on a 2 nm platinum wire made on twin pieces of 45 nm thick YIG grown on YAG and GGG substrates. These

samples were both subjected to acid etching. The resistivity is similar as mentioned previously and the YIG is 45 nm thick and so no difference would be expected. The data in figure 5.20 shows little difference between the two substrates for the size of the SHMR. There is however a move in the location of the maximum, shifted to a higher temperature on the YAG substrate. The reason for this is unclear and so for consistency GGG substrates were used for all other comparisons.
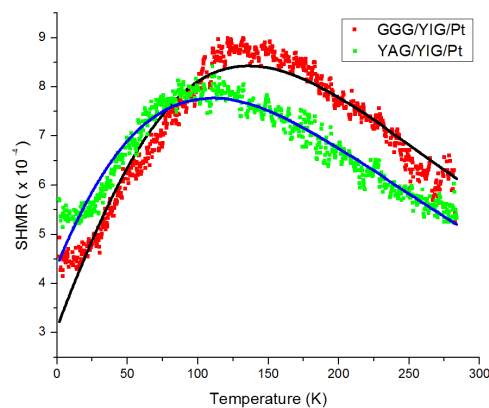
Figure 5.20: SHMR temperature dependence of a 2 nm platinum wire on YIG using YAG (green) and GGG (red) substrates. The shift of the peak towards a lower temperature for YAG substrates is not understood but could be due to surface roughness.

From this we conclude that YAG can be used as a suitable substrate to measure the SHMR. This is despite the differences in the YIG that are seen in comparison to GGG though the increased roughness does need to be considered especially if thicker films are used.

5.3.4 Etching effects

Further studies on platinum were done using the split pair magnet cryostat giving much better data than previously by doing a full rotation of the YIG magnetisation. The etched YIG of different thickness showed an SHMR nearly four times larger that the un-etched YIG in the previous section. This trend was seen on most samples with etched YIG being generally consistent in the size of the effect and un-etched being more variable. This we attribute to the YIG surface differing considerably after the

annealing stage. A single batch of YIG made to compare the etching effect revealed little difference. The temperature dependence is shown in figure 5.21.
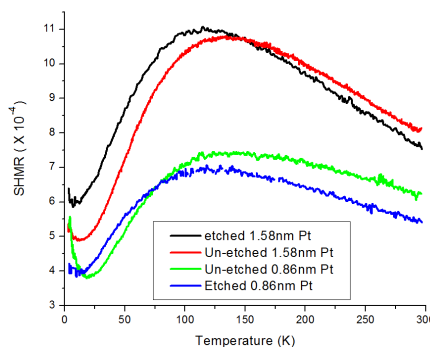
Figure 5.21: Comparison of SHMR temperature dependence on 70 nm etched and un-etched YIG. The peak in SHMR occurs at a slightly lower temperature for etched YIG possibly due to surface roughness.

An additional pair of samples in this batch was used in the TEM experiments seen in chapter 4. From this we see that the crystal structure on both the etched and un-etched samples are good and the main difference is that the etching has increased the surface roughness. The acid treatment on this removed only 2 nm of YIG yet the surface can be seen by TEM from the previous chapter in figure 4.29 to have become rougher. There is an increased upturn in the SHMR at low temperatures for the un-etched samples. The origin of this is not known but could be linked to iron atom contamination at the YIG interface. The small difference between the samples is that the maximum in the SHMR is at a lower temperature for the etched samples. As mentioned the YAG substrates have higher surface roughness and so do the etched samples here indicating that the roughness does make a small difference to the temperature dependence.

5.3.5 Platinum thickness dependence

A full temperature study was conducted on a range of platinum thicknesses. The results of this using the variable temperature method are illustrated in 5.22. These wires show the same basic shape as all previous platinum results. The main difference between

the platinum thicknesses is the size of the SHMR but still carries the same temperature dependence.
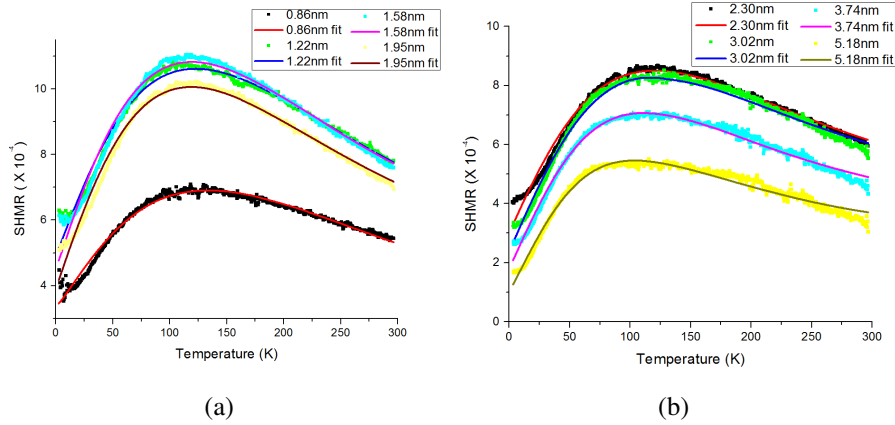
Figure 5.22: SHMR in platinum of different thicknesses and the fitted model based on the Elliot-Yafet mechanism. The solid lines show the fits to each thickness are in excellent agreement with the data with only minor deviations at low temperatures.

When this is plotted for an individual temperature in figure 5.23 we see the peak in SHMR is at approximately 1.2 nm. This has been reported in the literature for platinum and tantalum [160; 161]. An explanation put forward for the SHMR reaching a maximum at a particular thickness is that the spin diffusion length is independent of thickness [159]. The maximum SHMR being present at around 125 K for each thickness contradicts this. The SHMR maximum is given when the spin diffusion length is approximately double the thickness of the platinum.

Taking λ that follows the Elliot-Yafet mechanism, the fixed shape of the SHMR curves dictates that it mush have a value that is dependent on thickness for a given temperature. The fitting parameters used were a spin mixing conductance of 10^{15} $\Omega^{-1}m^{-2}$ that is temperature independent and a spin diffusion length as given by equation 5.3. The spin Hall angle is modelled by the measured resistivity ρ_{xx} and a constant, temperature independent, spin conductivity σ_{xy}. It has been suggested that the
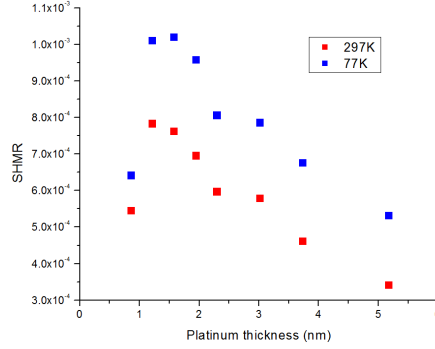
Figure 5.23: SHMR platinum thickness dependence at 297 K (red) and 77 K (blue). As the SHMR has a maximum at approximately 1.3 nm this implies it is not a proximity effect that would increase as thickness reduces.

spin conductivity has a temperature dependence related to the resistivity but this remains to be clearly proved [162]. If this were the case then the spin Hall angle could be roughly temperature independent. As the resistivity change is small over the given temperature range we would expect there to be little difference between the models until the platinum thickness approaches the bulk value.

$$\theta = \sigma_{xy}\rho_{xx} \qquad (5.4)$$

This was done for all the thicknesses and patterns were found for the different fitting parameters. From this we see that the spin diffusion length at a given thickness follows a linear trend with thickness. Part of this we can relate to the resistivity. As the thickness reduces the resistivity increases and from the Elliot-Yafet mechanism we would expect the spin diffusion length to decrease accordingly. This implies that surface scattering is the dominant effect both for change and spin transport. We would expect this to change as the spin diffusion length reaches a maximum value once bulk resistivity is obtained. However this cannot be measured like this as the effect becomes too weak to measure at such thicknesses. This may be possible if a way can be found to amplify the effect by scaling the spin mixing conductance up. The spin conductivity shows a drop that begins to level out towards a fixed value. The spin Hall angle follows the general trend of the resistivity with a correction made by the different spin conductivity.
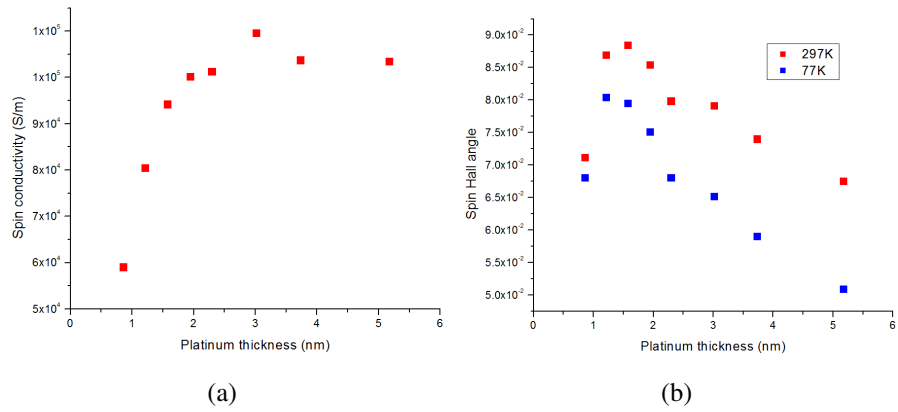
Figure 5.24: Spin Hall conductivity (a), and spin Hall angle calculations determined from the fitted curves in figure 5.23. The spin Hall conductivity becomes thickness independent above 3 nm and the spin Hall angle is then determined by the resistivity thickness dependence.
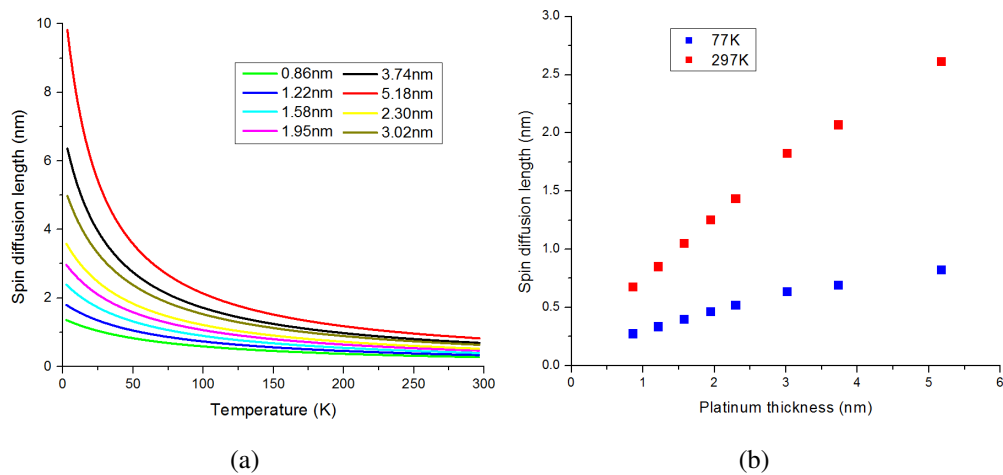
Figure 5.25: Spin diffusion length used in the SHMR fits (a). Shown as a function of thickness for two temperatures that suggests that the spin diffusion length is dependent on the thickness of the platinum similar to the electron mean free path (b).

Other groups have shown similar temperature trends. It was suggested that the spin diffusion length is a constant of 1.5 nm and that the shape is defined by the spin Hall angle changing [159]. The important difference in this data is that the SHMR
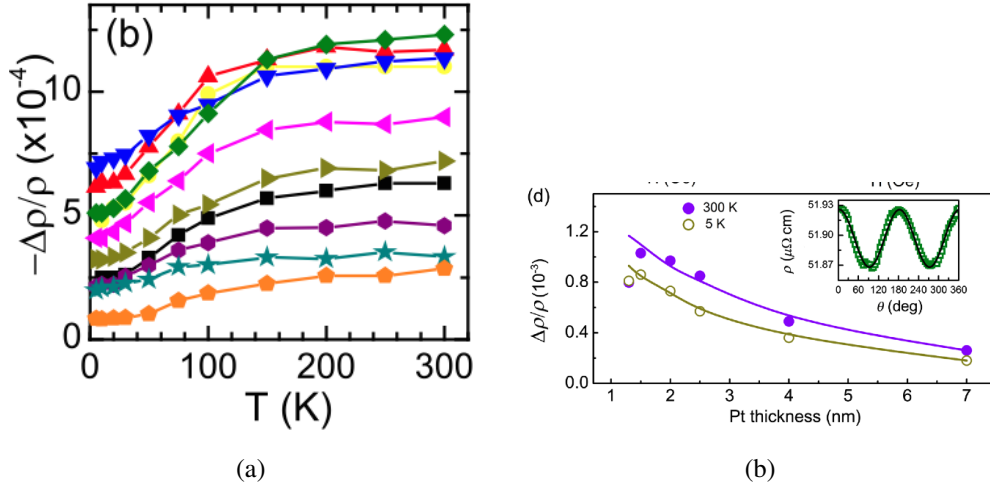
Figure 5.26: Comparative work from the literature that show a different temperature dependence to our results but a similar platinum thickness dependence. Taken from [159] and [154] respectively.

does not increase as the temperature increases from 300 K and only starts to drop at approximately 100 K. This is close to where our maximum is but this difference implies a difference in the platinum. This is possible as it was grown *in situ* by sputtering and without any surface treatment. We modelled the data for a 1.4 nm platinum wire with a fixed spin diffusion length of 1.5 nm and spin mixing conductance of 10^{15} $\Omega^{-1}\text{m}^{-2}$. Using the measured SHMR values and these assumed parameters the spin Hall angle could be determined. The corresponding spin Hall angle and spin conductivity are shown in figure 5.27.

From this the spin Hall angle matches the general shape of the SHMR. This could be a valid explanation however would require a justification of a temperature independent spin diffusion length. This we do not agree with. However the two properties could both be temperature dependent and so with two variables other experiments what depend on these parameters would be needed to determine the individual trends.

The final variable that is assumed but not known is the spin mixing conductance. This can be varied with little effect on the resulting spin diffusion length. It it the

(a)

(b)
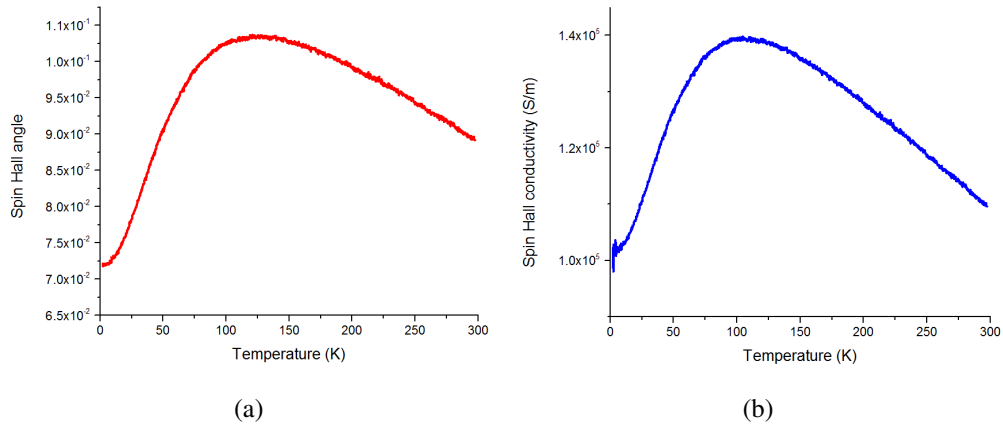
Figure 5.27: SHMR fit with temperature dependent spin Hall angle with a temperature independent spin diffusion length of 1.4 nm. The shape matches that of the SHMR temperature dependence.

product of this and the spin conductivity that multiples to give the scale of the SHMR so increasing one reduces the other. An experiment has been done to improve the spin mixing conductance by using a NiO spacer between the YIG and platinum [163]. The NiO is an insulating antiferromagnet and so spin mixing conductance happened at two interfaces. It has been shown that the spin current can be injected into the NiO and that this is more efficient that into the YIG alone. The spin Hall angle in platinum has been estimated to be between 0.024 and 0.11 [164–166]. This is in agreement with the values we see for our samples. The spin diffusion length is found to range from 0.5-10 nm which is in agreement with our values however the smaller spin diffusion lengths still remain controversial [167–169].

Chien *et al* shows the same SHMR trend as we do and is done in a similar fashion but with LPE grown YIG [154]. This suggests that the sputtering method we have used is as good as the LPE whereas the PLD method used is not the same [159]. We believe that some stage of the process is making a difference either to the platinum or the interface. As no acid treatment is performed by the PLD method this could be a reasonable explanation. The explanation given by Chien *et al* was that it is a magnetic proximity effect. This we do not agree with. As the literature has shown a

copper spacer is able to give a barrier to the proximity effect but the resistivity change is still detected. To examine the possibility of magnetic proximity effect a spacer was used between the platinum and YIG. For this both copper and gold were used. One drawback is that the copper resistivity is more temperature sensitive and so a sufficient temperature stability to conduct angular measurements is harder to achieve. Gold was found to be less of a problem for this. Here we see the same angular dependency but with a reduced size as expected due to the resistivity change only occurring in part of the metal system. Gold is reported to have a spin Hall angle but this is expected to be smaller than platinum and a large spin diffusion length so this should not make a significant contribution [164].

Platinum wires with gold and copper spacers have given a temperature dependence that demonstrates that the effect still works shown in figure 5.28. This is vital as the spacer should eliminate the possibility of the magnetic proximity being present in the platinum. These results show that the gold spacer is the best to replicate the SHMR temperature dependence as the effect is larger with this spacer. This is expected as the resistivity of gold is higher than cooper and so the total resistivity of the wire is dropped by a smaller amount. The copper dilutes the resistivity sufficiently that the effect becomes too small to get clear data by the dynamic temperature method we used. Also the temperature dependence of the copper resistivity is such that the smallest difference in temperature gives a change in the resistivity that is then confused with the SHMR. the temperature difference between the actual sample and the cernox becomes more problematic too.

In conclusion we have shown that the SHMR is present in platinum and that its effect can be explained by the EY mechanism. This gives spin diffusion lengths that are very small down to 0.4 nm. The thickness trend indicates that this small length scale is due to the surface scattering. The spin Hall angle is found to be in the expected range that has been reported in the literature. The variation of this as a function of thickness could help to explain why there is considerable disagreement on the exact value. We also find a minimum YIG thickness that is required to absorb the spin current that is injected from the platinum.
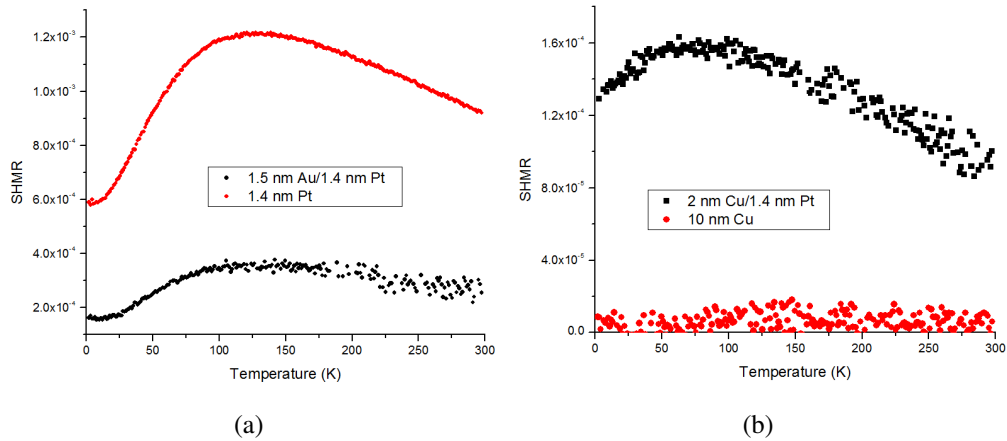
Figure 5.28: SHMR in platinum with spacers of gold and copper which demonstrate the effect is observed with the platinum not in direct contact with the YIG. Copper without platinum shows no SHMR as expected.

5.4 Spin Seebeck effect

Initially the SHMR was detected on YIG/Pt samples whereas SSE was not and so SHMR became the main research area. After the SHMR effect became much larger due to the YIG quality and acid etching the possibility of detecting the SSE was revisited. A crude experiment was done on a YIG/Pt sample to determine if the effect was measurable. The setup for this is shown in 5.29. The temperature gradient was generated by driving a current though a simple wire heater mounted under the hot copper plate. The setup is crude with the temperature gradient determined by changing the current and measuring the resulting difference with two thermocouples.

A temperature difference of approximately 30° C was made across the 8 mm long YIG sample. Two wire bonds on opposite ends on the platinum wire measured the voltage in the transverse direction. An applied magnetic field was then swept parallel to the direction of the thermal gradient. A voltage change is detected as the field is swept from parallel to antiparallel seen in figure 5.30.

104
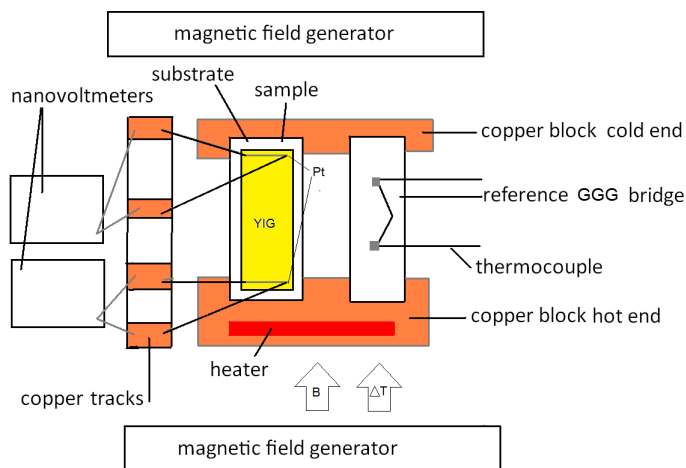
Figure 5.29: Experimental setup to measure the SSE on YIG/Pt sample. The sample is mounted to the copper plates by silver paint with high thermal conductivity to allow a large temperature gradient across a small 8 mm sample.
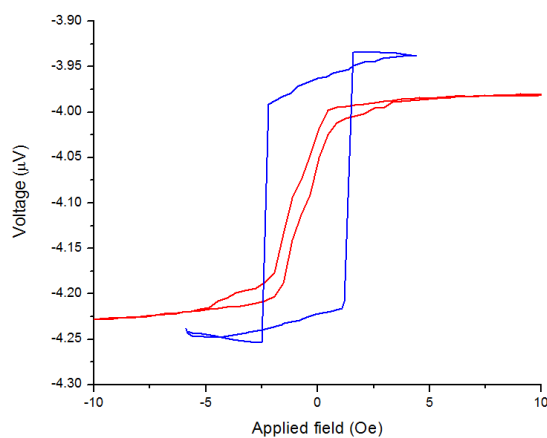
Figure 5.30: Transverse SSE voltage as the applied field is swept parallel to the temperature gradient. The blue curve shows the YIG hysteresis loop measured by VSM. These points coincide demonstrating the connection between the voltage in the platinum and the magnetisation of the YIG.

The magnetisation data shows that the voltage change is coincident with the magnetisation of the YIG. This demonstrates that the voltage change is connected to the YIG and is not due to artefacts like the Nernst effect [170; 171]. It is important to

repeat this experiment with more precise equipment. The SSE has been reported more widely in the longitudinal geometry and a large temperature gradient is needed to get a small voltage. The sample is mounted on the copper plates with silver conductive paint on the bottom of the substrate. This means there could be a small temperature gradient in the vertical direction.

Finally the SHMR was measured with the four probe method with the applied temperature gradient. This was to determine if there was any effect on the size of the SHMR with a spin current already being carried across the YIG/Pt interface. No noticeable change was detected and the experiment was ended to concentrate on the SHMR. Further work on the SSE is being conducted by our collaborators using samples made by the author but results of these are not yet complete.

CHAPTER 6

Spin Hall magnetoresistance in tungsten

6.1 Resistivity

6.1.1 Growth parameters

Tungsten wires were deposited by sputtering using the masking technique described in chapter 4. The wires are 200 μm wide and 3.5 mm long. Different parameters were tested to find the variation with different power and pressure. The pressure was varied between 2.4 and 20 mTorr and the power from 3 to 37 W. From this the optimum conditions were found for tungsten that exhibits SHMR. A power of 3 W and an atmosphere of 4.6 mTorr yielded a typical growth rate of 0.1 Å/s. The increased pressure is used to give the much slower growth rate to allow contaminants in the chamber such as oxygen to be incorporated into the metal. This has been suggested to be an important factor in growing β phase tungsten [172; 173]. It also reduces the heating effect from the plasma. Both of these effects help to promote the high resistivity tungsten with different resistivity temperature dependence. It was found that the growth rate and resistivity was not consistent like the platinum which can be attributed to several effects. At 3W the power could not be lowered any further and sustain a plasma. The temperature of the YIG surface is also believed to be important. The nitrogen shroud used to reduce the water partial pressure also has the effect of cooling the wheel that holds the samples. The wheel used for masks was found to produce the larger and more consistent SHMR which can be attributed to the sample having better thermal contact with the holder. Masks that were adapted to use the sheet film growth wheel demonstrated platinum wires that were identical to the masking wheel but tungsten wires failed to show any SHMR. To confirm the temperature issue a sample was grown in the masking wheel without the spring loaded cap pushing on the back of the sample and providing a strong thermal anchor. This sample yielded a wire that had a resistivity of 4.8 $\mu\Omega$cm in comparison to 288 $\mu\Omega$cm for identical wires with the thermal contact. The low resistivity showed no SHMR effect. The surface mobility of the tungsten atoms when deposited will be higher at warmer temperatures and so help promote the growth of ordered crystal structure. This is in keeping with what is seen with the resistivity.

A further experiment was conducted in an attempt to grow the tungsten in its beta phase. This is done by using off axis sputtering. This had to be improvised as the

sputtering system does not have a suitable mount. This is shown in figure 6.1 and can only be used for sheet material. If a mask is placed over the YIG surface its thickness is sufficient to stop the tungsten atoms having a path to the desired location. The sheet film was then scored into a narrow rectangle and then measured for SHMR. No effect was found and the resistivity was approximated to be 133 $\mu\Omega$cm. Several problems were identified with this method. First the growth rate is hard to measure by XRR as the film deposited has a variable thickness. This is due to the inconsistent distance between the sample and the target. The backing for the sample is also not thermally anchored to the plate. To promote the columnar nature of the beta phase it is desirable to have the sample surface cold so that the atoms have a reduced surface mobility. This locks them into the metastable state whereas heat allows the atoms to move towards the α phase which is a more energetically favourable structure.
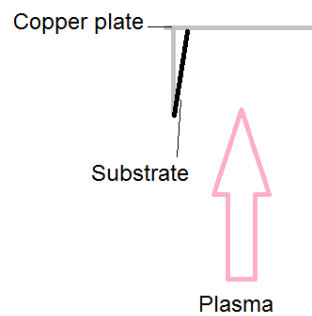
Figure 6.1: Off axis sputtering geometry for making sheet film beta phase tungsten. The mounting is to have metal atoms contacting the substrate at a low angle of incidence to promote the beta phase.

Tungsten in both α and β phases both produce high angle XRD peaks that have been observed in the literature [174]. XRD as well as resistivity measurements are required to distinguish beta phase from amorphous tungsten. We would also expect to see superconductivity at a higher temperature. No evidence was found by XRD for the beta phase or in the TEM images. Figure 6.2 shows no crystal structure evidence by XRD performed on tungsten grown on GGG despite a long count time being used.

There was a problem observed with some of the tungsten samples after deposition. On the thinnest samples of 2 nm or less there was a visible fading of the wires over
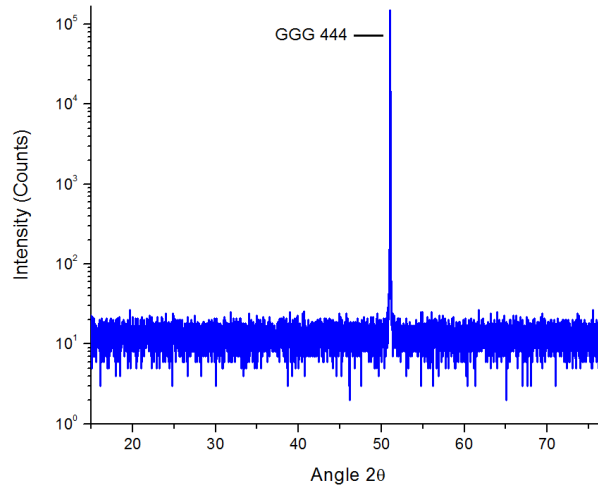
Figure 6.2: XRD scan of 18.6 nm thick tungsten sheet film grown on GGG with 10 second count time. No peaks were observed except for the GGG suggesting that the tungsten has no ordered structure.

time. This became noticeable several days after deposition. As they are individual wires the thickness could not be confirmed to have changed. Closer inspection also revealed that there are cracks and fragments missing on some of these including patches that have faded and others that have not. Resistivity checks showed that the wires had even had the conductivity broken along its length in places. The initial suspicion is that these cracks were caused by a thermal shock as a result of being cooled too quickly in a cryostat. The fading however did still occur on some of the wires without being placed in a cryostat or being subjected to any high temperature changes. This fading looks like it could be due to an oxidation process. As a consequence the tungsten wires were measured as soon as possible after growth. As can be seen from the thickness dependence the resistivity is not necessarily able to indicate if some degree of oxidation has taken place. This could partially explain some of the difficulties and inconsistencies in measuring the SHMR.

6.1.2 Thickness dependence

With the standard growth conditions multiple thicknesses were made as with the platinum. The resistivity as a function of thickness can be seen for several different batches

in figure 6.3.
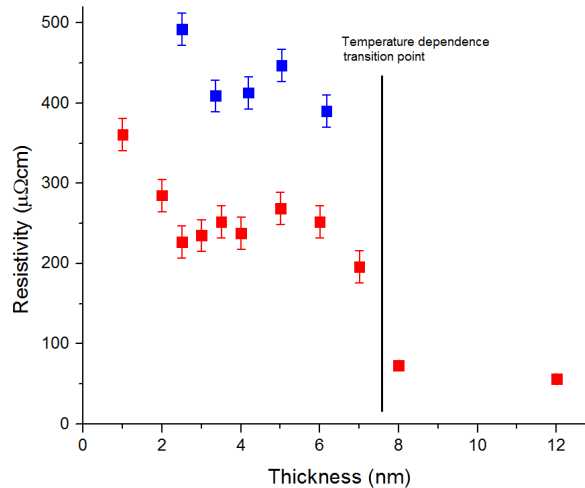
Figure 6.3: Resistivity as a function of tungsten thickness. Samples taken from different batches shown in red and blue. Above 7 nm thick the temperature coefficient of resistivity becomes positive and behaves like a normal metal.

From this it can be seen that there is not the same pattern as for a normal metal. This is due to the resistivity of the material being sufficiently high that the additional surface scattering caused by reducing thickness makes only a small difference. The resistivity does reduce as the thickness is increased but in more complex way. Above 7 nm the resistivity makes a sharp drop as the material begins to exhibit NM temperature characteristics. The spin Hall angle of the tungsten could also be due to skew scattering and the side jump mechanism from any contaminants in the material. Oxygen and nitrogen could be added to the tungsten during growth that contributes to the amorphous high resistivity and account for the variable nature of the resistivity. Between growths the oxygen and nitrogen contents are measured before the argon gas enters the chamber but cannot be monitored after the plasma is lit. The amount of impurities and defects only needs to be small to produce a large spin Hall angle in materials such as $Cu_{99.5}Bi_{0.5}$ [175]. The nitrogen content can also have a considerable effect on the superconductivity of the material by raising the transition temperature. An experiment was done to deliberately add oxygen to the chamber to promote β phase growth. The minimum amount was 0.5 SCCM and tungsten was grown in this atmosphere with the same argon amount. After growth the thickness was found to be 3 times thicker than

expected. The material was also insulating. This indicates that tungsten oxide has been grown instead.

6.1.3 Temperature dependence

The resistivity as a function of temperature for thin tungsten is shown in figure 6.4 (a). Here is is also seen that it deviates from the expected model for a NM. Instead we see a small but rising increase in resistivity as the temperature is lowered. It has also been shown that β phase tungsten undergoes a transition to the α phase after being heated to approximately 400 °C. This was tried and the resistivity returned to its room temperature value further indicating that our films are not metastable β phase.

(a) 3 nm thick
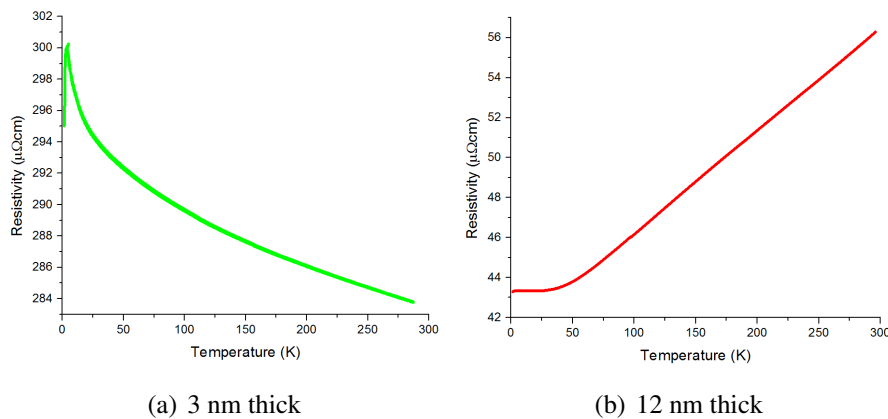
(b) 12 nm thick

Figure 6.4: Resistivity temperature dependence of 3 nm, (a), and 12 nm tungsten wires (b). The resistivity is much lower and has the opposite temperature coefficient of resistivity for wires over 7 nm thickness.

Figure 6.4 shows the temperature dependence of two different thicknesses of tungsten on both sides of a phase transition. For 3 nm tungsten the resistivity increases as it is cooled in comparison to the NM behaviour of the 12 nm wire. In the low temperature region of the thin tungsten there is a sudden drop in resistivity just before the minimum temperature of 1.5 K is reached. This is due to the tungsten approaching its transition temperature for superconductivity. To investigate this properly a different cryostat would be needed to reach the required temperature. The alpha phase is a type I superconductor and has a transition temperature of 15 mK and a critical field of 12 x

10^{-5} T [176; 177]. β phase has been shown to be as high as 4 K [178]. Studies have also shown that amorphous material possesses superconductivity [179–181]. Some of the resistivities also show a mixture of amorphous and NM state. If a current is driven through a metal that is superconducting the effect of the SHMR is unknown. A spin current can be transmitted by magnons without loss of energy but to inject it into the YIG a charge current that does is needed. Superconducting material could eliminate this inefficiency too.

6.2 SHMR properties

6.2.1 Field rotations

The field rotations fit with the $\sin^2$ angular dependence for the in-plane rotations at all temperatures above 10 K as shown in figure 6.5.
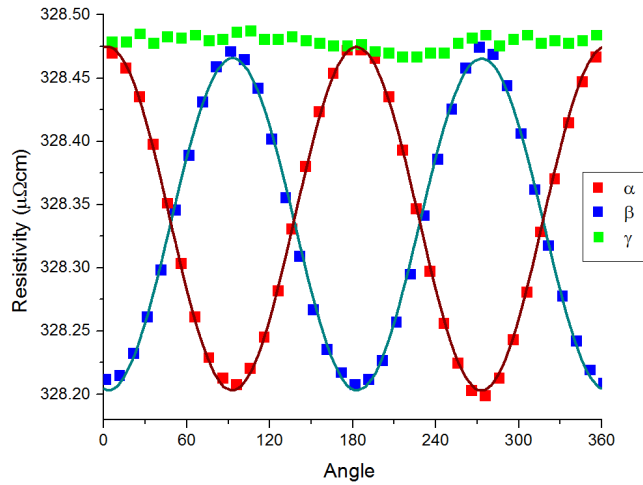
Figure 6.5: Angular dependency of the in-plane SHMR for 3.5 nm thick tungsten at 20 K for all three orientations. The fits show the expected $\sin^2$ trend at the correct angles predicted by SHMR theory.

The in-plane angle is labelled α and the transverse and longitudinal out of plane angles labelled β and γ respectively. At low temperatures the out of plane rotation starts to deviate from the $\sin^2\theta$ relation. Below this there was a large increase in the effect on one sample that is not understood. This effect was shown by angular sweeps

to be different from the SHMR as the $\sin^2 \theta$ fit is broken. Instead there is an additional effect that is much larger and with different angular dependence that is seen in rotations out of the plane.
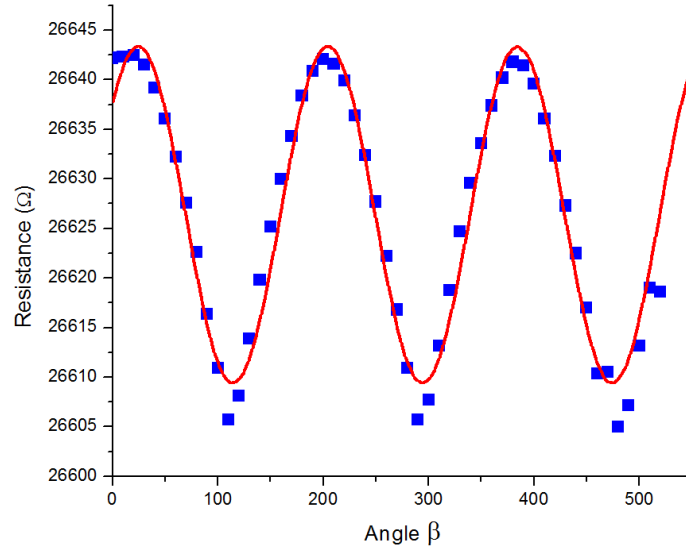
Figure 6.6: Low temperature out of plane transverse rotation of 3.9 nm tungsten wire. Measurement taken at 5 K. The data deviates from the expected pattern given by the red $\sin^2 \theta$ curve.

The deviation from the expected trend suggests a secondary effect with a different angular dependency. To demonstrate the effect field sweeps were taken that highlight the temperature sensitivity of the effect in this region.

These sweeps show a very sharp rise as the temperature approaches 0 K. At 20 K in figure 6.7 (a) we see a steep drop due to the SHMR and a small gradient beyond its saturation. At 1.6 K in (b) the resistivity change of 60 x 10 $^{-4}$ for rotation out of the plane (angle β). The in-plane rotation did not show this increase as will be seen later. This change is nearly an order of magnitude higher than what is expected from the SHMR. As a result of this the data below 5 K is not valid for interpretation of the SHMR fitting parameters. This additional effect was not found to be reproducible and had considerable variation and so its origin is yet to be determined. From the resistivity values of these two sweeps we can see that the resistivity is higher at 1.6
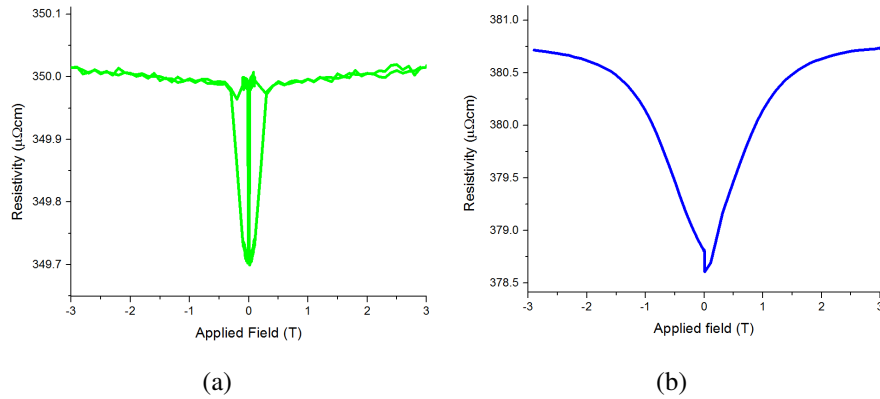
Figure 6.7: Out of the plane field sweeps taken at 20 K, (a), and 1.6 K (b). For the measurement at 1.6 K there is an additional magnetoresistive effect that is much larger than the SHMR making it difficult to measure accurately from field sweeps.

K and so there is no superconducting transition that could be responsible. It was also noted that tungsten did not always produce the SHMR effect on YIG samples that were known to work with platinum wires on the same surface. From this we can deduce that the tungsten growth is the key factor rather than the quality of the interface that is the main factor for platinum.

6.2.2 Thickness dependence

First measurements of the tungsten showed that the SHMR is present as in platinum with the same angular dependence. This was done with the standard SHMR rig at room temperature and 77 K under liquid nitrogen. The in-plane angular dependence was found to match with theory. From this the thickness dependence shown in figure 6.8 is obtained. This data shows a similar shape as a function of thickness with the maximum at approximately 3.5 nm in figure 6.8. This is double the maximum found in the platinum which suggests that the spin diffusion length is larger. Additional samples were tested in the cryostat that confirmed that this thickness dependence is correct and consistent. There are differences between batches however that scale up the effect. This is a problem for comparing samples between batches as the SHMR size does not match as well as the resistivity. Additional samples were tested in the

cryostat that confirmed that this thickness dependence is correct and consistent. There are differences between batches however that scale up the effect. This is a problem for comparing samples between batches as the SHMR size does not match.
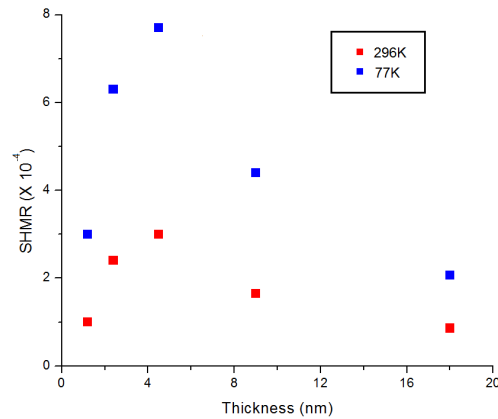
Figure 6.8: SHMR thickness dependence of tungsten at 300 K and 77 K (blue). The SHMR follows a similar thickness dependence as platinum but with a maximum that occurs at a larger thickness of approximately 3.5 nm.
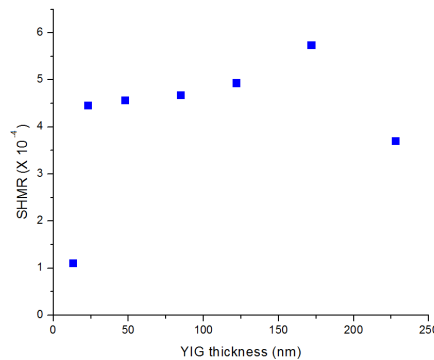
Figure 6.9: SHMR of 3.5 nm tungsten on different thicknesses of YIG. Measurements taken at 297 K. No clear pattern can be identified however the 13 nm YIG film gives a much lower effect which was also seen in platinum. The lower SHMR in the thickest YIG sample s possibly a poor individual sample.

Different YIG thicknesses were also measured with a standard thickness of tungsten. These are the same YIG samples that were used in the previous chapter to mea-

sure the YIG thickness dependence with platinum. The results from this are shown in figure 6.9. Here we see a similar pattern to that which is seen by the platinum indicating that the effect is independent of YIG thickness above 20 nm. This data provides an important test to eliminate the YIG thickness as a source for the inconsistency of the YIG material. Other samples of different YIG thicknesses do show inconsistent SHMR however this we attribute to the tungsten itself and not the YIG thickness.

6.2.3 Field dependence

The rotation measurements were tested as a function of applied magnetic field to determine the contribution due to other MR effects. We see that the SHMR increases with applied magnetic field strength in a pattern similar to the platinum. In plane rotations at 297 K shown in figure 6.10 demonstrate a considerable increase in the SHMR as the field is increased to 3 T.
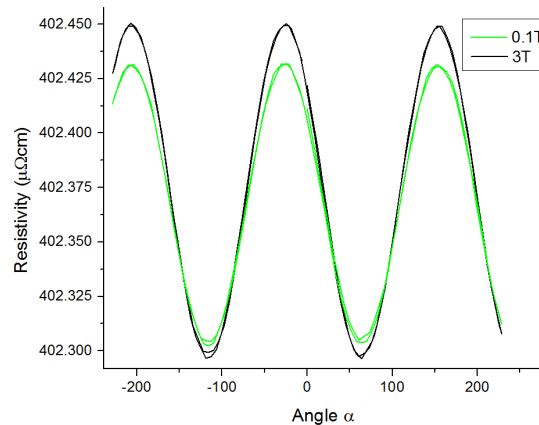
Figure 6.10: SHMR in-plane rotation as a function of applied magnetic field. Done at 297 K. The SHMR should be independent of field strength indicating that the difference here is due to an additional field dependent magnetoresistive effect.

To give a true measure of the SHMR resistivity change this extra effect needs to be considered. This is plotted as a function of applied field in figure 6.11. For platinum the effect could me modelled as Kohler magnetoresistance following a B^2 relationship. For tungsten we see a better fit is found for a linear field dependence. This could be an indicator of weak localisation which is expected in disordered metals [182]. A combination of both effects would be expected that could be confirmed by measurements

at higher applied magnetic fields. The intercept provides the resistivity change that would be seen if the magnetisation of the YIG is rotated without any applied magnetic field to the tungsten and therefore eliminate these other field strength dependent magnetoresistive effects.
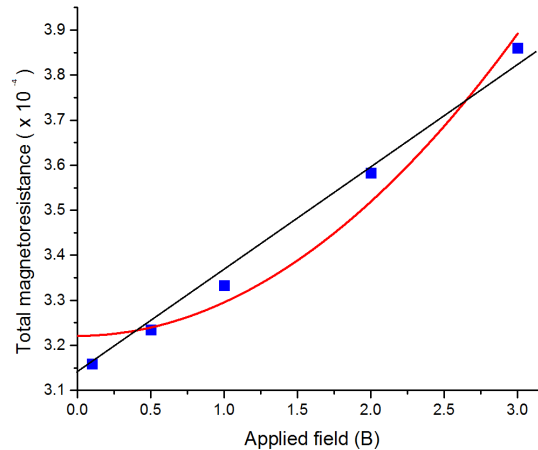
Figure 6.11: Total magnetoresistance measured by in plane rotation on 3 nm tungsten wire as a function of applied magnetic field. The fits are given for Kohler MR, (red), and weak localisation (black). Done at 297 K.

6.3 Temperature dependence

6.3.1 Tungsten SHMR

The full temperature dependence was measured on multiple samples. The general trend is that the SHMR increases linearly as the temperature is lowered. At low temperatures approaching 5 K there is a deviation from this that is not consistent. The first experiments done by taking full rotations at a range of temperatures are shown in figure 6.12. There is a small reduction in the SHMR at the low temperature end. The rotations showed the $\sin^2$ angular dependence for the α and β direction for all the measurements above 2.4 K. Below this temperature the effect increases considerably out of the plane as seen in figure 6.7 This was done on 2 samples of different YIG thickness but a tungsten wire of 3.5 nm thick.
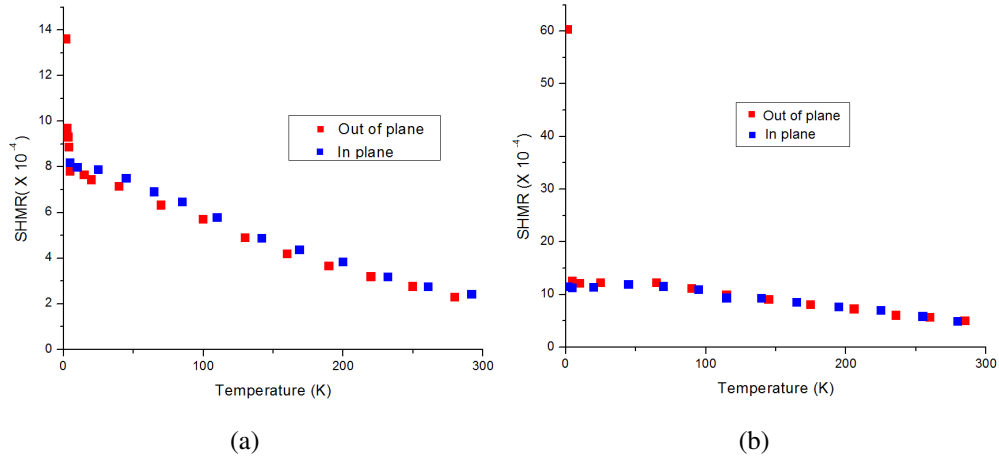
Figure 6.12: SHMR measurements as a function of temperature on 3.5 nm tungsten. Measurements done on 200 nm, (a), and 65 nm, (b), thick YIG films that have been etched both showing a linear trend with temperature.

The difference between the intensity of the SHMR suggests that there is a considerable difference between the two interfaces or the tungsten itself. As the tungsten was grown identically in the same cycle it is unlikely that the tungsten material itself should be different. As has been shown the bulk thickness of the YIG itself should make no difference to the SHMR. From this we attribute this to the top surface of the YIG. If the acid etching did not remove all of the non-garnet like material after annealing on the thicker YIG then this could have reduced the effective surface area of the interface where spin mixing conductance can occur. The rotation was also done out of the plane to confirm the size of the effect given by the red data points. We see a low temperature deviation from the in plane measurements that is consistent with what is measured in figure 6.7. The data fits a simple linear trend until approximately 2.4 K when the effect suddenly increases up to 60 x 10^{-4}. This is not part of the SHMR and this is confirmed by the difference in the angular dependency. This large increase is only present in the out of plane rotations.

The full temperature measurements were done using the dynamic temperature method. This confirms the basic trend given by the angular measurements. Due to the deviation

119

at low temperatures an angular rotation was done after the main scan to confirm that the effects seen in the rotations were not present. This was done at 0.1 T to remove the high field effects and with a current of 50 μA. The SHMR data for different tungsten thicknesses as a function of temperature is shown in figure 6.13. The temperature dependence of the resistivity for these wires is given in figure 6.14. These wires all show the same high resistivity that increases as the temperature is lowered. No superconductivity downturn is observed in any of these wires above the minimum temperature reached of 1.5 K.
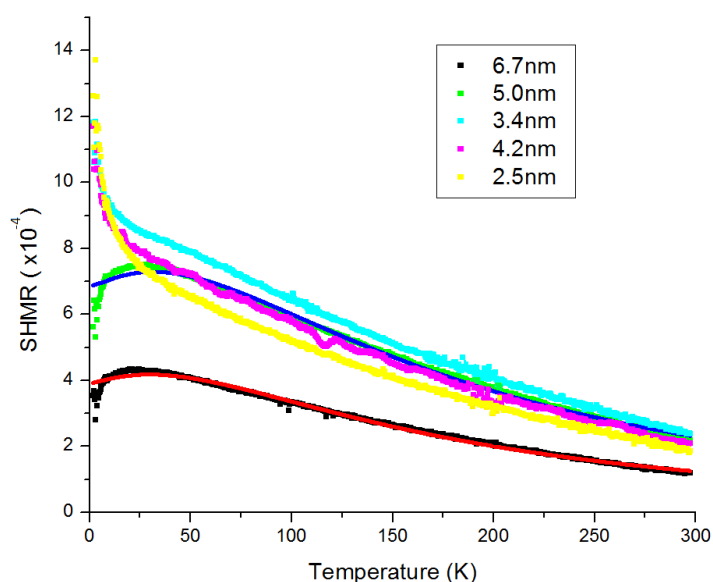
Figure 6.13: Full temperature dependence of the SHMR on different thicknesses of tungsten. Two fits are shown in blue and red for the EY mechanism. The thinner wires could not be fitted due to the upturns in SHMR at the low temperature region being incompatible with our models of spin diffusion length.

The same linear increase as the temperature is lowered is seen but the low temperature region still shows some deviations that cannot be explained with any certainty. The three thinnest tungsten wires show a sharp rise in the SHMR in the low temperature region instead of a flattening out as with most other samples. This makes fitting to the theory impossible as the expected spin diffusion length model does not allow for this. Ignoring this part of the data does not solve the problem as the maximum point
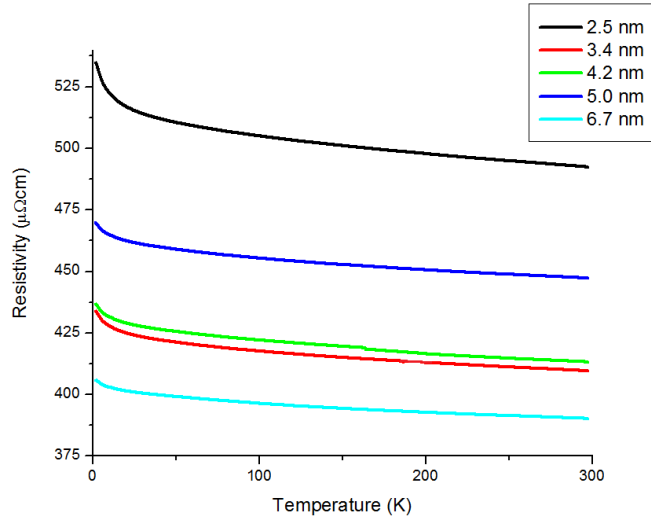
Figure 6.14: Resistivity of different thickness tungsten wires as a function of temperature. The general temperature dependence is consistent but the individual values do not have a progressive trend as a function of thickness.

in the SHMR provides the boundary condition for the spin diffusion length. Without this fixed point a whole range of values can be fitted to the linear part of the data. The cause of this upturn is not understood and is attributed to the inconsistency of the tungsten growth. As can be seen from the resistivity data it cannot be attributed to any superconducting transition. A possible explanation is that the thinner wires contain small regions of β phase tungsten. As this phase is metastable more of the amorphous tungsten could be transitioning into the β phase. This would cause a large increase in the spin Hall angle that would distort the SHMR temperature dependence. Fitting the data using the same parameters as the platinum provide a different spin diffusion length. The resistivity can be approximated to vary as 1/T and so the spin diffusion length is modelled as proportional to temperature. From this the spin diffusion length is linearly dependent on temperature following the Elliot-Yafet mechanism.

The spin Hall angle is smaller than platinum and depends on the thickness of the material. The spin diffusion length is much larger reaching up to 10 nm and above 1 nm for the two wires measured. We would expect this to become smaller for thinner wires however this cannot be proved. The larger spin diffusion length is found in material
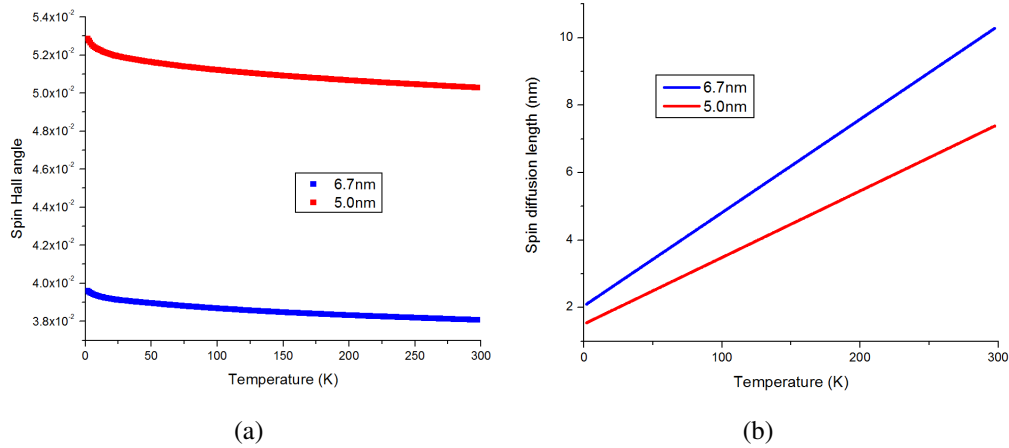
Figure 6.15: Spin Hall angle, (a), and spin diffusion length, (b), fits for 5 nm and 6.7 nm thick tungsten. The spin Hall angle changes very little as the resistivity change is small and the spin diffusion length is found to increase linearly with temperature.

that is of a much higher resistivity that the platinum. As a result more research needs to be done into the tungsten to explain how this is the case. In comparison to the literature the spin Hall angle and spin diffusion length are of the right order of magnitude. The exact values are more problematic due to the different phases. For β phase tungsten the spin Hall angle is given between 0.4 and 0.33 [183; 184]. These are far higher than our results and so we do not believe that we have made β phase tungsten. The spin diffusion length is found to be between 3.5 nm and 0.45 nm at room temperature which is also smaller than ours. For alpha phase tungsten the spin Hall angle is reported to be between 0.0043 and 0.14 [185; 186]. The spin diffusion length is given as 1.5 nm but as the spin Hall angle is small publications often do not quote values for the alpha phase. The measurements for spin Hall effects are often too difficult to make [186; 187]. Amorphous tungsten is not used for spin Hall effects and so there is no clear values given for this material. If there is small regions of β phase tungsten in the predominantly amorphous material then the variation in the SHMR between batches can be understood. The residual oxygen content is believed to influence the formation of β phase tungsten [188–190]. The residual content in the sputtering chamber during growth is small and cannot be measured or controlled during deposition but could provide a means of obtaining a giant spin Hall angle.

6.3.2 Amorphous and normal metal phases

An important difference found in tungsten on one batch gave contrasting resistivity data. Two tungsten wires were grown on YIG of 3.9 nm and 5.5 nm thick. The thinner wire had the same resistivity trend as other thin tungsten wires grown with the standard parameters. The thicker wire behaved like a normal metal shown in figure 6.16. The thicker tungsten wire is of a much lower resistivity and behaves as a NM and so provides a means of testing the EY mechanism in two data sets that should have different spin diffusion length temperature dependence. Also there is a noticeable upturn in the resistivity in the low temperature region of the thicker tungsten wire. The minimum resistance occurs at 37 K which is considerably higher in comparison to the same thickness in platinum.

(a) 3.9 nm thick (b) 5.5 nm thick
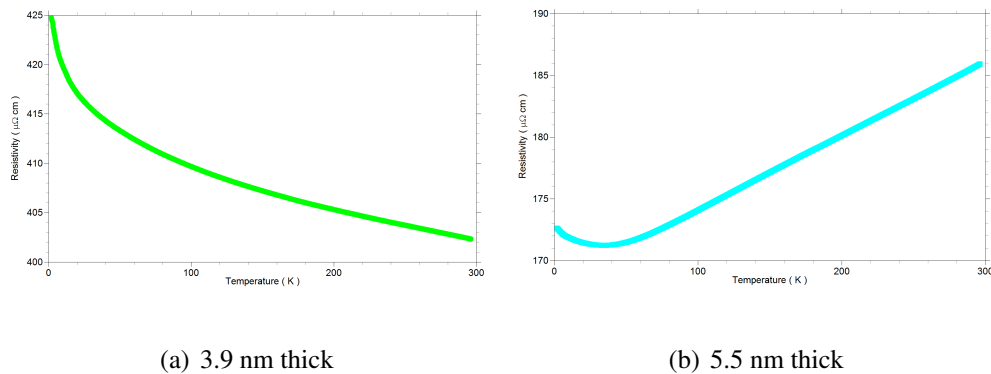
Figure 6.16: Resistivity temperature measurements of two different tungsten wires. Thicknesses of 3.9 nm (a), and 5.5 nm, (b) respectively that have opposite temperature coefficients of resistivity.

The SHMR data shows a slightly different pattern to the previous samples for both wires. The high temperature region shows a linear increase with reducing temperature as before. However there is now a sharper downturn than has been seen previously. This is present in both wires despite the differing resistivity with the thicker wire having the later peak in SHMR. This maximum makes it easier to fit a model as it provides a crucial boundary condition based on the ratio of thickness to spin diffusion length.

The resistivity curves give us the following models for the spin diffusion length for the thinner, equation 6.1, and thicker, equation 6.2 wires.

$$\lambda = \frac{a}{T + b} \tag{6.1}$$

$$\lambda = aT + b \tag{6.2}$$
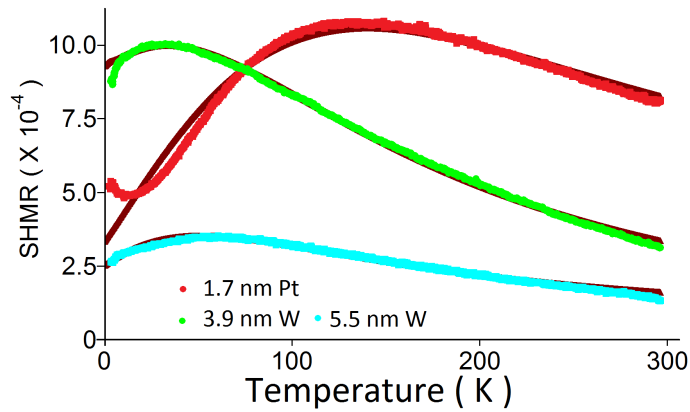
Figure 6.17: SHMR of the tungsten wires and compared to platinum. The fits from the EY mechanism are shown in brown which make a close comparison to the data. The maximum in the tungsten SHMR occurs at a much lower temperature than platinum.

These fits are shown by the brown curves in figure 6.17 and are compared to a platinum wire from the previous chapter. These fits assume a temperature independent spin mixing conductance of 10^{15} $\Omega^{-1}m^{-2}$ and constant spin conductivity. These parameters are given in figure 6.18 and 6.19.

As the change in resistivity is small even compared to platinum over the temperature range measured this alone cannot account for the SHMR change which strongly indicates that the spin Hall angle is not the dominant parameter. The different spin diffusion length fits for similar SHMR dependence do offer an alternative mathematical solution. For NM resistivity behaviour the SHMR can be fitted with a spin diffusion length that is proportional to temperature. The tungsten wires produce similar SHMR
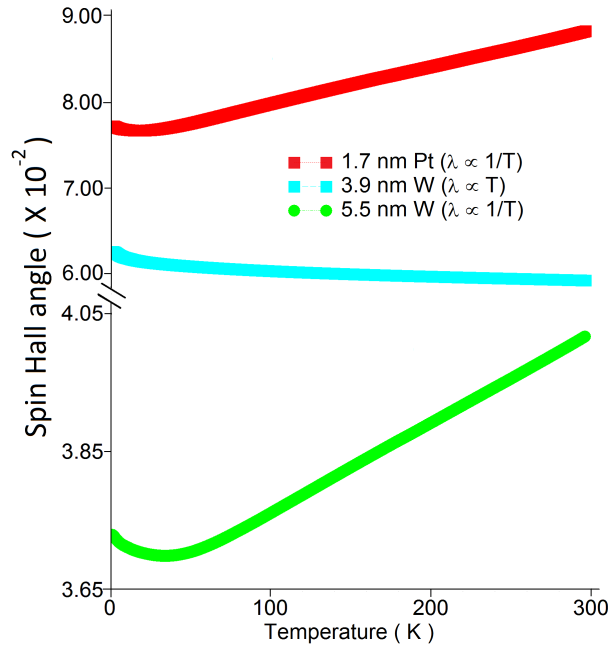
Figure 6.18: Fitted spin Hall angle for tungsten and platinum wires. Trend follows the resistivity temperature dependence for each individual wire with the amorphous tungsten having the larger value.
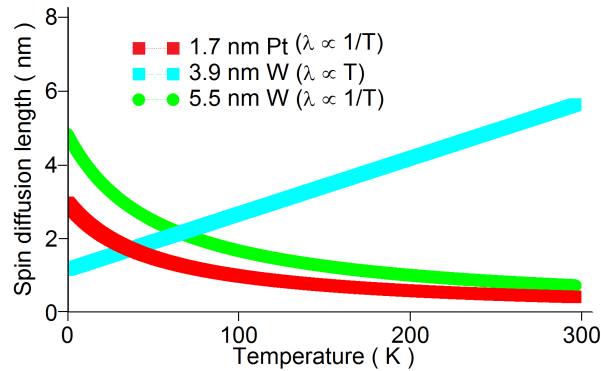
Figure 6.19: Fitted spin diffusion length for tungsten and platinum wires based on EY spin relaxation mechanism. For the thin tungsten wire this results in a linear temperature dependence in contrast to the thicker tungsten that is inversely proportional to temperature.

temperature dependence and so the spin diffusion length trend can be swapped round for the different resistivity. From the formula for spin diffusion length the diffusion

constant still retains the temperature dependence that is defined by the resistivity. To obtain the linear dependence the spin relaxation time would be inversely proportional to the momentum relaxation time to the third power as given by equation 6.3.

$$\tau_{sf} \propto T^{-3} \qquad (6.3)$$

No known mechanism has been proposed that follows this temperature relation and so we discount it. These two wires have demonstrated the high variability of the tungsten and that its growth nature is yet to be fully established. We are satisfied that the SHMR is present in this material and that is is present in both amorphous and NM resistivity material. The NM state in particular needs further study as there were limited number of samples showing this behaviour. In other batches thicker wires were made than those in this section and yet they still produced an amorphous state. This low resistivity tungsten needs to be reproduced to confirm what is seen. It is also likely that it needs to be on a similar thickness so that the SHMR can be measured. A much thicker wire would be expected to form into the alpha phase however the SHMR would be expected to be much smaller.

In conclusion tungsten has been demonstrated for the first time to exhibit SHMR. It has given a new testing round for the SHMR theory to be used to explain the data. We have demonstrated that this can be done with the EY mechanism for a different resistivity temperature dependence. The tungsten is not yet fully understood however and further research is needed to make the samples reproducible. The β phase also remains elusive which if made could become the material of choice for the effect due to its high spin Hall angle and superconductivity properties.

6.4 Other metals

Other metals were also investigated for the SHMR. Tantalum has already been shown to have the effect and this was confirmed in our experiments [161]. The effect is however very small barely making a rotation that could be detected. This is due to a very narrow set of growth parameters needed to grow the tantalum and so was not studied any further. Discussions with one of the authors of this publication revealed

that the conditions required for the tantalum growth were very sensitive. This we believe was the reason for the small size of the effect seen in tantalum as it was not grown correctly. The resistivity was found to be very high and increased with reducing temperature in the same manner as the thin tungsten.

Iridium manganese $Ir_{80}Mn_{20}$ is an antiferromagnet that has a significant spin Hall angle [191]. This material was sputtered from a stochiometric target and the SHMR was measured with the rotation method. This detected a weak effect but smaller than expected shown in figure 6.20. The thickness was suspect as the metal is known to oxidise which explains the high resistivity. An aluminium cap would prevent this but to be thick enough to cover the surface the resistivity would be reduced so that the effect would be too small to measure. A carbon cap was tried but no SHMR was measured on this. The reason for this is unknown as the material was deposited by the same method.
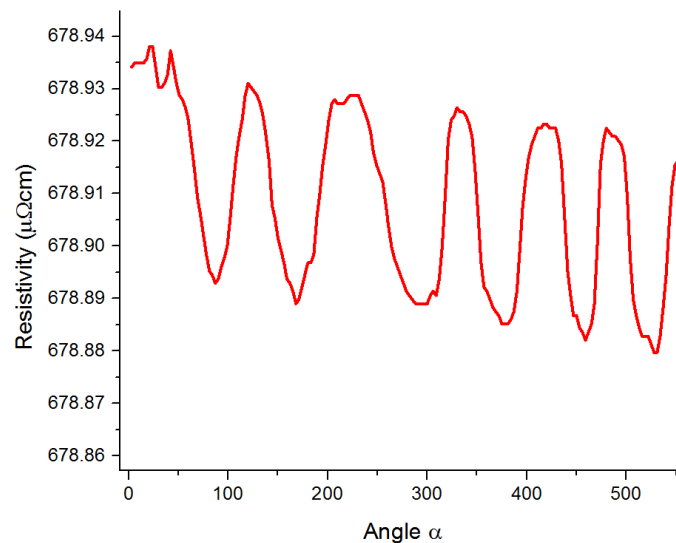
Figure 6.20: SHMR effect detected in IrMn. Measured at room temperature. The data is crude due to the measurement method but does still show an obvious magnetoresistance effect that is dependent on angle.

Copper Bismuth $Cu_{99.5}Bi_{0.5}$ has a large spin Hall angle of 0.26 due to skew scattering [175]. The bismuth is a much heavier element than the copper. The SHMR

can be expected to have a much larger SHMR than platinum due to this larger spin Hall angle. It also is far from the Stoner criteria in comparison to platinum and so the magnetic proximity effect can be discounted completely. Measurements on this material showed no SHMR. The reason for this is unclear and segregation of the bismuth could be the cause. The skew scattering mechanism works when the bismuth atoms are mixed in well with the copper and if the bismuth becomes concentrated the effect will be diminished. This segregation is known to happen at just over room temperature. The material is also not capped and the spin diffusion length is not known. To detect a significant SHMR the thickness needs to be close to this size and for copper the spin diffusion length is known to be in the micron range. The wires studied here we all less than 10 nm. Despite this experiment failing it should be studied further as this will give a much greater confidence to our explanation for the origin of the effect.

CHAPTER 7

Conclusions and future work

7.1 Conclusions

The first key achievement of this work is the YIG growth process. This recipe has been developed to produce a generally consistent set of samples that exhibit all the fundamental properties of high quality YIG. The results demonstrate that this material is able to be used for measuring the same SHMR effect as on that made by LPE. Since our first publication this method has been cited by other groups and the method reproduced for use in other spin research. The work done to improve the YIG growth has therefore been successfully received by the wider scientific community and has aided in spin current research both for the study of SHMR and other effects. As a ferrimagnetic insulator YIG can be used on a much wider range of research beyond SHMR. The YIG has also been requested and used for collaborative work by research groups in Exeter, Cambridge and Regensburg for use in FMR, spin torque and spin wave propagation experiments. Improvements to making it by a standard method that can be replicated in most condensed matter laboratories will help to scale up and reduce the costs of this research.

The SHMR has been reproduced and is found to be in general agreement with what is found in the literature for platinum. Valuable lessons have been learned about the important criteria that needs to be met in order to produce the best devices for this effect. The temperature and thickness data have given a test of the SHMR theory with different models for the spin relaxation. From this the spin diffusion length and spin Hall angle has been estimated and linked to the thickness and resistivity of the platinum. Some questions do still need to be resolved such as the possibility of magnetic proximity effect. Our experiments using a spacer do suggest however that this is not the case and that the magnetoresistance is not due to a proximity effect.

The SHMR has also been demonstrated for the first time in tungsten. This is found to be of a similar magnitude to platinum but with a different temperature dependence. The difference in the temperature dependence gives a new test of the theory as it needs to be consistent for both metals. The further use of different metals that have different transport properties will be the most logical way to unravel the full nature of the effect. By gathering as much data from this we can be more confident in the models we

have used to depict the spin properties. Adding tungsten to what is known forms one piece of this puzzle that remains to be decisively proved. What we can conclude is that the model adopted for platinum can be used to explain the effect in tungsten. Inconsistencies in the tungsten SHMR still need to be resolved however, this can be linked to a similar inconsistency in the tungsten growth itself that affects its basic transport properties.

Although only touched on briefly in this work the SSE has also been demonstrated to work in the same samples as for SHMR. This effect is now being studied in further detail by our collaborators.

7.2 Future work

The YIG process has potential for refinement. There are other experiments that can be done to examine the stoichiometry in further detail. This could include XPS and high resolution STEM mapping. The magnetisation properties need to be investigated further. The downturn in thin films is not fully explained. We believe that there is diffusion of the substrate and YIG elements across the interface. It needs to be determined if this is the case and to what extent. Which elements are mixing and how far do they penetrate through the neighbouring material. High resolution STEM mapping may be able to see finer details of the chemical composition across the interface. To investigate the magnetic properties of the bottom layer of the YIG films a more sensitive magnetometry method is needed as it cannot be done by simply taking measurements of the bulk sample. We presently have an application to probe this magnetic "dead" layer using polarised neutron reflectometry (PNR). We suspect that this layer is caused by a GdIG layer this material is also now being intentionally grown for comparison. The YIG/NM interface can also be investigated and refined. AFM can be used for chemical analysis [192]. The YIG surface has also been demonstrated to be improved by heating before the platinum deposition [140].

The growth process can also be improved if the annealing and etching can be replaced. The annealing stage can be done *in-situ* that could speed up sample production further. The deposition can even be done with a high substrate temperature that may

make films that are epitaxial as grown. The issue would be the oxygen content of the films as high temperatures in an oxygen atmosphere can cause oxidation of the sputtering chamber components if in sufficient concentration. Atmospheric pressure air could not be used in conjunction with sputtering. Acid etching is the most uncontrolled part of the recipe and also the most dangerous to perform. Being able to eliminate this step altogether would be ideal. As we have seen some thin YIG films have been found to have the same spin mixing conductance as untreated films but this is not consistent between batches. Alternative cleaning steps should be investigated to give the same interface quality. These include ion milling and plasma oxidation.

The SHMR is not sufficient on its own to prove the value and temperature dependence of the key parameters. There are too many unknowns and so the same devices need to be used in other experiments that have a different relation to spin diffusion length, spin Hall angle and spin mixing conductance. This would include FMR and SSE. FMR experiments are currently underway both in our research group and with collaborators. A comparison of these related effects could give a better indication of which parameters are the dominate factor as a function of temperature.

As platinum is well established to exhibit SHMR with a similar temperature dependence further studies need to be undertaken to explain some of the more subtle differences. This could be due to the quality of the platinum crystal structure. The spin Hall angle could therefore be affected by this and so the platinum could be made by different methods on the same YIG material and compare the differences. To probe the structure will be problematic as the wires have to be thin to give a large effect but gives very little material to work with. XRD for example needs a sufficient amount of material to produce intensity above the background level. High resolution TEM dark field imaging can be used to show differences in diffraction patterns from the material.

In tungsten the nature of the material is of much greater interest as this has much bigger implications for the spin diffusion length model. Refinement and better understanding of the growth process would hopefully answer some of these questions. In particular the substrate temperature during the tungsten growth should be monitored.

If the sample is cold during deposition this would favour freezing defects into the tungsten whereas heat helps the atoms to form into an ordered structure. This is due to the atomic mobility on the surface as it is deposited. This temperature needs to be both measured and controlled. Currently the temperature is lowered by the presence of the liquid nitrogen shroud and heated by the plasma when the sample moves over the sputter gun. Other proposals have suggested that the residual oxygen and other gas content in the growth atmosphere may play a part in the tungsten growth. This would require finer control over flow rates than our current systems. The oxygen is also believed to be important in the formation of beta phase tungsten. If this can be achieved then the SHMR could become a much larger effect to an order of magnitude higher than platinum. Combined with efforts to improve the spin mixing conductance the effect could find use in practical devices. This beta phase is going to require considerable work to master. If successful it would also reduce the costs both of research and applications as tungsten is relatively cheap in comparison to the heavy precious metals.

REFERENCES

[1] T. H. Flowers, "The design of colossus," *IEEE Ann. Hist. Comput.*, vol. 5, pp. 239–252, Jul 1983.

[2] S. McKay, *The secret life of Bletchley Park : the history of the wartime codebreaking centre by the men and women who were there*. London: Aurum, 2010.

[3] M. Johnson and R. H. Silsbee, "Interfacial charge-spin coupling: Injection and detection of spin magnetization in metals," *Phys. Rev. Lett.*, vol. 55, p. 1790, Oct. 1985.

[4] M. N. Baibich, J. M. Broto, A. Fert, F. N. Van Dau, F. Petroff, P. Etienne, G. Creuzet, A. Friederich, and J. Chazelas, "Giant magnetoresistance of (001)fe/(001)cr magnetic superlattices," *Phys. Rev. Lett.*, vol. 61, p. 2472, Nov 1988.

[5] G. Binasch, P. Grünberg, F. Saurenbach, and W. Zinn, "Enhanced magnetoresistance in layered magnetic structures with antiferromagnetic interlayer exchange," *Phys. Rev. B*, vol. 39, p. 4828, Mar 1989.

[6] S. Maekawa, S. Valenzuela, E. Saitoh, and T. Kimura, *Spin Current*. Series on Semiconductor Science and Technology, OUP Oxford, 2012.

[7] Z. An, F. Q. Liu, Y. Lin, and C. Liu, "The universal definition of spin current," *Nature*, vol. 2, p. 388, May 2012.

[8] J. Shi, P. Zhang, D. Xiao, and Q. Niu, "Proper definition of spin current in spin-orbit coupled systems," *Phys. Rev. Lett.*, vol. 96, p. 076604, Feb 2006.

[9] S. Wolf, A. Chtchelkanova, and D. Treger, "Spintronics - a retrospective and perspective," *IBM. J. Res. Dev*, vol. 50, pp. 101–110, Jan 2006.

[10] B. Wang, J. Wang, J. Wang, and D. Y. Xing, "Spin current carried by magnons," *Phys. Rev. B*, vol. 69, p. 174403, May 2004.

[11] S. M. Rezende, R. L. Rodríguez-Suárez, R. O. Cunha, A. R. Rodrigues, F. L. A. Machado, G. A. Fonseca Guerra, J. C. Lopez Ortiz, and A. Azevedo, "Magnon spin-current theory for the longitudinal spin-seebeck effect," *Phys. Rev. B*, vol. 89, p. 014416, Jan 2014.

[12] S. Rezende, R. Rodríguez-Suárez, R. Cunha, J. L. Ortiz, and A. Azevedo, "Bulk magnon spin current theory for the longitudinal spin seebeck effect," *J. Magn. Magn. Mater.*, vol. 400, pp. 171–177, 2015.

[13] H. Kurebayashi, O. Dzyapko, V. E. Demidov, D. Fang, A. J. Ferguson, and S. O. Demokritov, "Controlled enhancement of spin-current emission by three-magnon splitting," *Nat Mater*, vol. 10, pp. 660–664, Sept 2011.

[14] S. O. Demokritov, V. E. Demidov, O. Dzyapko, G. A. Melkov, A. A. Serga, B. Hillebrands, and A. N. Slavin, "Bose-einstein condensation of quasi-equilibrium magnons at room temperature under pumping," *Nature*, vol. 443, pp. 430–433, Sept 2006.

[15] R. White, *Quantum Theory of Magnetism: Magnetic Properties of Materials*. Springer Series in Solid-State Sciences, Springer, 2007.

[16] M. Getzlaff, *Fundamentals of Magnetism*. Springer Berlin Heidelberg, 2007.

[17] Y. Tserkovnyak, A. Brataas, and G. E. W. Bauer, "Enhanced gilbert damping in thin ferromagnetic films," *Phys. Rev. Lett.*, vol. 88, p. 117601, Feb 2002.

[18] Y. Kajiwara, K. Harii, S. Takahashi, J. Ohe, K. Uchida, M. Mizuguchi, H. Umezawa, H. Kawai, K. Ando, K. Takanashi, S. Maekawa, and E. Saitoh, "Transmission of electrical signals by spin-wave interconversion in a magnetic insulator," *Nature*, vol. 464, pp. 262–266, Mar 2010.

[19] C. W. Sandweg, Y. Kajiwara, A. V. Chumak, A. A. Serga, V. I. Vasyuchka, M. B. Jungfleisch, E. Saitoh, and B. Hillebrands, "Spin pumping by parametrically excited exchange magnons," *Phys. Rev. Lett.*, vol. 106, p. 216601, May 2011.

[20] D. Ralph and M. Stiles, "Spin transfer torques," *J. Magn. Magn. Mater.*, vol. 320, pp. 1190 – 1216, December 2008.

[21] K. Ando, S. Fujita, J. Ito, S. Yuasa, Y. Suzuki, Y. Nakatani, T. Miyazaki, and H. Yoda, "Spin-transfer torque magnetoresistive random-access memory technologies for normally off computing," *J. Appl. Phys.*, vol. 115, no. 17, 2014.

[22] S. Mangin, D. Ravelosona, J. A. Katine, M. J. Carey, B. D. Terris, and E. E. Fullerton, "Current-induced magnetization reversal in nanopillars with perpendicular anisotropy," *Nat Mater*, vol. 5, pp. 210–215, Mar 2006.

[23] Y. P. Kalmykov, W. T. Coffey, S. V. Titov, J. E. Wegrowe, and D. Byrne, "Spin-torque effects in thermally assisted magnetization reversal: Method of statistical moments," *Phys. Rev. B*, vol. 88, p. 144406, Oct 2013.

[24] E. Tsymbal and I. Zutic, *Handbook of Spin Transport and Magnetism.* CRC Press, 2011.

[25] J. E. Hirsch, "Spin Hall Effect," *Phys. Rev. Lett.*, vol. 83, p. 1834, Aug. 1999.

[26] J. Sinova, S. O. Valenzuela, J. Wunderlich, C. H. Back, and T. Jungwirth, "Spin Hall effects," *Rev. Mod. Phys.*, vol. 87, pp. 1213–1260, Oct. 2015.

[27] T. Moorsom, M. Wheeler, M. Taukeer Khan, F. Al Maapos;Mari, G. Burnell, B. J. Hickey, V. Lazarov, D. Gilks, and O. Cespedes, "Effects of spin doping and spin injection in the luminescence and vibrational spectrum of c60," *Appl. Phys. Lett.*, vol. 105, no. 2, 2014.

[28] S. Majumdar and H. S. Majumdar, "On the origin of decay of spin current with temperature in organic spintronic devices," *Org. Electron*, vol. 13, no. 11, pp. 2653 – 2658, 2012.

[29] F. Al Ma'Mari, M. Wheeler, E. Kendric, G. Burnell, B. Hickey, T. Moorsom, and O. Cespedes, "Direct measurement of spin polarization in ferromagnetic-c60 interfaces using point-contact andreev reflection," *IEEE Trans. Magn.*, vol. 50, pp. 1–4, Nov 2014.

[30] Z. Vardeny, *Organic Spintronics*. CRC Press, 2010.

[31] T. Moorsom, M. Wheeler, T. Mohd Khan, F. Al Ma'Mari, C. Kinane, S. Langridge, D. Ciudad, A. Bedoya-Pinto, L. Hueso, G. Teobaldi, V. K. Lazarov, D. Gilks, G. Burnell, B. J. Hickey, and O. Cespedes, "Spin-polarized electron transfer in ferromagnet/c_{60} interfaces," *Phys. Rev. B*, vol. 90, p. 125311, Sep 2014.

[32] S. Watanabe, K. Ando, K. Kang, S. Mooser, Y. Vaynzof, H. Kurebayashi, E. Saitoh, and H. Sirringhaus, "Polaron spin current transport in organic semiconductors," *Nat Phys*, vol. 10, pp. 308–313, Apr 2014.

[33] G. E. W. Bauer, E. Saitoh, and B. J. van Wees, "Spin caloritronics," *Nat Mater*, vol. 11, pp. 391–399, May 2012.

[34] H. Frota and A. Ghosh, "Spin caloritronics in graphene," *Solid State Commun*, vol. 191, pp. 30 – 34, Nov 2014.

[35] H. Adachi, K.-i. Uchida, E. Saitoh, and S. Maekawa, "Theory of the spin Seebeck effect," *Rep. Prog. Phys.*, vol. 76, p. 036501, Mar. 2013.

[36] C. M. Jaworski, J. Yang, S. Mack, D. D. Awschalom, J. P. Heremans, and R. C. Myers, "Observation of the spin-seebeck effect in a ferromagnetic semiconductor," *Nat Mater*, vol. 9, pp. 898–903, Nov 2010.

[37] K. Uchida, J. Xiao, H. Adachi, J. Ohe, S. Takahashi, J. Ieda, T. Ota, Y. Kajiwara, H. Umezawa, H. Kawai, G. E. W. Bauer, S. Maekawa, and E. Saitoh, "Spin seebeck insulator," *Nat Mater*, vol. 9, pp. 894–897, Nov 2010.

[38] A. Kehlberger, U. Ritzmann, D. Hinzke, E.-J. Guo, J. Cramer, G. Jakob, M. C. Onbasli, D. H. Kim, C. A. Ross, M. B. Jungfleisch, B. Hillebrands, U. Nowak, and M. Kläui, "Length scale of the spin seebeck effect," *Phys. Rev. Lett.*, vol. 115, p. 096602, Aug 2015.

[39] K. Uchida, T. Ota, K. Harii, S. Takahashi, S. Maekawa, Y. Fujikawa, and E. Saitoh, "Spin-seebeck effects in films," *Solid State Commun*, vol. 150, no. 11–12, pp. 524 – 528, 2010.

[40] H. Nakayama, M. Althammer, Y.-T. Chen, K. Uchida, Y. Kajiwara, D. Kikuchi, T. Ohtani, S. Geprägs, M. Opel, S. Takahashi, R. Gross, G. E. W. Bauer, S. T. B. Goennenwein, and E. Saitoh, "Spin hall magnetoresistance induced by a nonequilibrium proximity effect," *Phys. Rev. Lett.*, vol. 110, p. 206601, May 2013.

[41] Y.-T. Chen, S. Takahashi, H. Nakayama, M. Althammer, S. T. B. Goennenwein, E. Saitoh, and G. E. W. Bauer, "Theory of spin hall magnetoresistance (smr) and related phenomena," *J. Phys. Condens. Matter*, vol. 28, no. 10, p. 103004, 2016.

[42] C. O. Avci, K. Garello, A. Ghosh, M. Gabureac, S. F. Alvarado, and P. Gambardella, "Unidirectional spin hall magnetoresistance in ferromagnet/normal metal bilayers," *Nat Phys*, vol. 11, pp. 570–575, July 2015.

[43] R. Iguchi, K. Sato, D. Hirobe, S. Daimon, and E. Saitoh, "Effect of spin hall magnetoresistance on spin pumping measurements in insulating magnet/metal systems," *Appl. Phys. Express*, vol. 7, p. 013003, Dec 2014.

[44] S. Wang, L. Zou, X. Zhang, J. Cai, S. Wang, B. Shen, and J. Sun, "Spin seebeck effect and spin hall magnetoresistance at high temperatures for a pt/yttrium iron garnet hybrid structure," *Nanoscale*, vol. 7, pp. 17812–17819, 2015.

[45] M. Althammer, S. Meyer, H. Nakayama, M. Schreier, S. Altmannshofer, M. Weiler, H. Huebl, S. Geprägs, M. Opel, R. Gross, D. Meier, C. Klewe, T. Kuschel, J.-M. Schmalhorst, G. Reiss, L. Shen, A. Gupta, Y.-T. Chen, G. E. W. Bauer, E. Saitoh, and S. T. B. Goennenwein, "Quantitative study of the spin hall magnetoresistance in ferromagnetic insulator/normal metal hybrids," *Phys. Rev. B*, vol. 87, p. 224401, Jun 2013.

[46] J. H. Han, Y. Y. Wang, Q. H. Yang, G. Y. Wang, F. Pan, and C. Song, "Spin hall magnetoresistance in nb/y3fe5o12 hybrids," *Phys. Status Solidi Rapid Res. Lett.*, vol. 9, no. 6, pp. 371–374, 2015.

[47] K. Fuchs, "The conductivity of thin metallic films according to the electron theory of metals," *Math. Proc. Cambridge.*, vol. 34, pp. 100–108, Jan 1938.

[48] M. Sanquer, R. Tourbot, and B. Boucher, "Correlation between high- and low-temperature conductivities in high resistive disordered metals," *EPL*, vol. 7, p. 635, Jul 1988.

[49] I. Grant and W. Phillips, *Electromagnetism.* Manchester Physics Series, Wiley, 1991.

[50] I. Žutić, J. Fabian, and S. Das Sarma, "Spintronics: Fundamentals and applications," *Rev. Mod. Phys.*, vol. 76, pp. 323–410, Apr 2004.

[51] R. J. Elliott, "Theory of the effect of spin-orbit coupling on magnetic resonance in some semiconductors," *Phys. Rev.*, vol. 96, pp. 266–279, Oct 1954.

[52] Y. Yafet and V. Jaccarino, "Nuclear spin relaxation in transition metals; core polarization," *Phys. Rev.*, vol. 133, p. 1630, Mar 1964.

[53] P. Boross, B. Dóra, A. Kiss, and F. Simon, "A unified theory of spin-relaxation due to spin-orbit coupling in metals and semiconductors," *Sci. Rep.*, vol. 3, p. 3233, Nov. 2013.

[54] M. I. D'Yakonov and V. I. Perel', "Possibility of Orienting Electron Spins with Current," *J. Exp. Theor. Phys.*, vol. 13, p. 467, June 1971.

[55] M. I. Dyakonov and V. I. Perel, "Current-induced spin orientation of electrons in semiconductors," *Phys. Lett. A.*, vol. 35, pp. 459–460, July 1971.

[56] G. L. Bir, A. G. Aronov, and G. E. Pikus, "Spin relaxation of electrons due to scattering by holes," *J. Exp. Theor. Phys.*, vol. 42, p. 705, 1976.

[57] A. W. Overhauser, "Polarization of nuclei in metals," *Phys. Rev.*, vol. 92, pp. 411–415, Oct 1953.

[58] M. C. Onbasli, A. Kehlberger, D. H. Kim, G. Jakob, M. Kläui, A. V. Chumak, B. Hillebrands, and C. A. Ross, "Pulsed laser deposition of epitaxial yttrium iron garnet films with low gilbert damping and bulk-like magnetization," *APL Mater.*, vol. 2, Oct 2014.

[59] H. Chang, P. Li, W. Zhang, T. Liu, A. Hoffmann, L. Deng, and M. Wu, "Nanometer-thick yttrium iron garnet films with extremely low damping," *IEEE Magn. Lett.*, vol. 5, pp. 1–4, Sept 2014.

[60] Y. Kajiwara, K. Harii, S. Takahashi, J. Ohe, K. Uchida, M. Mizuguchi, H. Umezawa, H. Kawai, K. Ando, K. Takanashi, S. Maekawa, and E. Saitoh, "Transmission of electrical signals by spin-wave interconversion in a magnetic insulator," *Nature*, vol. 464, pp. 262–266, 03 2010.

[61] M. Zwierzycki, Y. Tserkovnyak, P. J. Kelly, A. Brataas, and G. E. W. Bauer, "First-principles study of magnetization relaxation enhancement and spin transfer in thin magnetic films," *Phys. Rev. B*, vol. 71, p. 064420, Feb 2005.

[62] Y.-T. Chen, S. Takahashi, H. Nakayama, M. Althammer, S. T. B. Goennenwein, E. Saitoh, and G. E. W. Bauer, "Theory of spin hall magnetoresistance," *Phys. Rev. B*, vol. 87, p. 144411, Apr 2013.

[63] S. R. Boona, R. C. Myers, and J. P. Heremans, "Spin caloritronics," *Energy Environ. Sci.*, vol. 7, pp. 885–910, 2014.

[64] J. Wunderlich, B. Kaestner, J. Sinova, and T. Jungwirth, "Experimental observation of the spin-hall effect in a two-dimensional spin-orbit coupled semiconductor system," *Phys. Rev. Lett.*, vol. 94, p. 047204, Feb 2005.

[65] Y. K. Kato, R. C. Myers, A. C. Gossard, and D. D. Awschalom, "Observation of the spin hall effect in semiconductors," *Science*, vol. 306, no. 5703, pp. 1910–1913, 2004.

[66] N. A. Sinitsyn, "TOPICAL REVIEW: Semiclassical theories of the anomalous Hall effect," *J. Phys. Condens. Matter*, vol. 20, p. 023201, Jan. 2008.

[67] S. Murakami, N. Nagaosa, and S.-C. Zhang, "Dissipationless quantum spin current at room temperature," *Science*, vol. 301, no. 5638, pp. 1348–1351, 2003.

[68] J. Sinova, D. Culcer, Q. Niu, N. A. Sinitsyn, T. Jungwirth, and A. H. MacDonald, "Universal intrinsic spin hall effect," *Phys. Rev. Lett.*, vol. 92, p. 126603, Mar 2004.

[69] J. Smit, "The spontaneous hall effect in ferromagnetics ii," *Physica*, vol. 24, pp. 39–51, Jan 1958.

[70] C. Herschbach, D. V. Fedorov, I. Mertig, M. Gradhand, K. Chadova, H. Ebert, and D. Ködderitzsch, "Insight into the skew-scattering mechanism of the spin hall effect: Potential scattering versus spin-orbit scattering," *Phys. Rev. B*, vol. 88, p. 205102, Nov 2013.

[71] Y. Niimi, Y. Kawanishi, D. H. Wei, C. Deranlot, H. X. Yang, M. Chshiev, T. Valet, A. Fert, and Y. Otani, "Giant spin hall effect induced by skew scattering from bismuth impurities inside thin film cubi alloys," *Phys. Rev. Lett.*, vol. 109, p. 156602, Oct 2012.

[72] M. Gradhand, D. V. Fedorov, P. Zahn, and I. Mertig, "Skew scattering mechanism by an ab initio approach: Extrinsic spin hall effect in noble metals," in *Trends in Magnetism*, vol. 168 of *Solid State Phenomena*, pp. 27–30, Trans Tech Publications, 1 2011.

[73] J. S. Lim, D. Sánchez, and R. López, "Spin-current noise from fluctuation relations," in *AIP Conf. Proc.*, vol. 1566 of *American Institute of Physics Conference Series*, pp. 363–364, Dec. 2013.

[74] S. Hoffman, K. Sato, and Y. Tserkovnyak, "Landau-lifshitz theory of the longitudinal spin seebeck effect," *Phys. Rev. B*, vol. 88, p. 064408, Aug 2013.

[75] S. Maekawa, "Magnons, Spin Current and Spin Seebeck Effect," in *APS*, Feb. 2012.

[76] K. Uchida, S. Takahashi, K. Harii, J. Ieda, W. Koshibae, K. Ando, S. Maekawa, and E. Saitoh, "Observation of the spin seebeck effect," *Nature*, vol. 455, pp. 778–781, October 2008.

[77] S. Geller, "Crystal chemistry of the garnets*," *Z. Kristallogr.*, vol. 125, pp. 1–47, Dec. 1967.

[78] E. Joyce, *The technique of furniture making*. City: Batsford, 1987.

[79] P. W. Anderson, "Antiferromagnetism. theory of superexchange interaction," *Phys. Rev.*, vol. 79, pp. 350–356, Jul 1950.

[80] E. Koch, "Exchange mechanisms," http://www.cond-mat.de/events/correl12/manuscripts/koch.pdf.

[81] H. Wang, C. Du, P. C. Hammel, and F. Yang, "Strain-tunable magnetocrystalline anisotropy in epitaxial $Y_3fe_5o_{12}$ thin films," *Phys. Rev. B*, vol. 89, p. 134404, Apr 2014.

[82] H. Arend and J. Hulliger, *Crystal Growth in Science and Technology*. Springer US, 2012.

[83] F. Miller, A. Vandome, and M. John, *Czochralski Process*. VDM Publishing, 2010.

[84] R. F. Bryan, "Handbook of crystal growth. vol. 3: Thin films and epitaxy," *J. Appl. Crystallogr.*, vol. 30, p. 419, Jun 1997.

[85] S. Kostić, Z. Ž. Lazarević, V. Radojević, A. Milutinović, M. Romčević, N. Ž. Romčević, and A. Valčić, "Study of structural and optical properties of yag and nd:yag single crystals," *Materials Research Bulletin*, vol. 63, pp. 80–87, 3 2015.

[86] H. Nelson, "Liquid-phase epitaxy—its role in crystal growth technology," *J. Crys. Growth.*, vol. 27, pp. 1–5, Dec 1974.

[87] W. Tolksdorf, H. Dammann, E. Pross, B. Strocka, H. J. Tolle, and P. Willich, "Growth of yttrium iron garnet multi-layers by liquid phase epitaxy for single mode magneto-optic waveguides," *J. Crys. Growth.*, vol. 83, pp. 15–22, May 1987.

[88] T. Aichele, A. Lorenz, R. Hergt, and P. Görnert, "Garnet layers prepared by liquid phase epitaxy for microwave and magneto-optical applications – a review," *Cryst. Res. Technol.*, vol. 38, pp. 575–587, July 2003.

[89] R. Behrisch and W. Eckstein, *Sputtering by Particle Bombardment: Experiments and Computer Calculations from Threshold to MeV Energies*. Springer Berlin Heidelberg, 2007.

[90] J. A. Thornton, "Magnetron sputtering: basic physics and application to cylindrical magnetrons," *J. Vac. Sci. Technol. A.*, vol. 15, p. 171, Mar. 1978.

[91] N. Porter, *Magnetoresistance in n-type Silicon*. PhD thesis, School of Physics and Astronomy, University of Leeds, September 2010.

[92] M. B. Jungfleisch, V. Lauer, R. Neb, A. V. Chumak, and B. Hillebrands, "Improvement of the yttrium iron garnet/platinum interface for spin pumping-based applications," *Appl. Phys. Lett.*, vol. 103, p. 022411, July 2013.

[93] T. Tashiro, S. Matsuura, A. Nomura, S. Watanabe, K. Kang, H. Sirringhaus, and K. Ando, "Spin-current emission governed by nonlinear spin dynamics," *Sci. Rep.*, vol. 5, p. 15158, Oct 2015.

[94] M. Agrawal, *Thermally Driven Magnon Transport in the Magnetic Insulator Yttrium Iron Garnet*. 2014.

[95] S. T. B. Goennenwein, R. Schlitz, M. Pernpeintner, K. Ganzhorn, M. Althammer, R. Gross, and H. Huebl, "Non-local magnetoresistance in YIG/Pt nanostructures," *Appl. Phys. Lett.*, vol. 107, p. 172405, Oct. 2015.

[96] J. Als-Nielsen and D. McMorrow, *Elements of Modern X-ray Physics*. Wiley, 2001.

[97] M. M. Woolfson, *An Introduction to X-ray Crystallography*. Cambridge University Press, 1997.

[98] N. Stribeck, *X-Ray Scattering of Soft Matter*. Springer Berlin Heidelberg, 2007.

[99] N. W. Ashcroft and N. D. Mermin, *Solid state physics*. Saunders College, 1976.

[100] J. R. Hook and H. E. Hall, *Solid State Physics*. Wiley, 1995.

[101] D. Jiles, *Introduction to Magnetism and Magnetic Materials, Second Edition*. Taylor & Francis, 1998.

[102] S. Foner, "Versatile and Sensitive Vibrating-Sample Magnetometer," *Rev. Sci. Instrum.*, vol. 30, pp. 548–557, July 1959.

[103] D. O. Smith, "Development of a vibrating coil magnetometer," *Rev. Sci. Instrum.*, vol. 27, pp. 261–268, January 1956.

[104] H. Czichos, T. Saito, and L. Smith, *Springer Handbook of Materials Measurement Methods*. Springer Handbook of Materials Measurement Methods, Springer Berlin Heidelberg, 2007.

[105] J. Clarke and A. Braginski, *The SQUID Handbook: Applications of SQUIDs and SQUID Systems*. Wiley, 2006.

[106] J. C. Yang, M. W. Small, R. V. Grieshaber, and R. G. Nuzzo, "Recent developments and applications of electron microscopy to heterogeneous catalysis," *Chem. Soc. Rev.*, vol. 41, pp. 8179–8194, 2012.

[107] P. W. Hawkes, *Advances in Imaging and Electron Physics*. No. v. 116, Elsevier Science, 2001.

[108] R. Erni, M. D. Rossell, C. Kisielowski, and U. Dahmen, "Atomic-Resolution Imaging with a Sub-50-pm Electron Probe," *Phys. Rev. Lett.*, vol. 102, p. 096101, Mar. 2009.

[109] R. Egerton, *Physical Principles of Electron Microscopy: An Introduction to TEM, SEM, and AEM*. Springer US, 2011.

[110] E. Jensen, *Transmission Electron Microscope System*. https://www.overleaf.com/4161593xkdkdx/12255384/.

[111] S. J. Pennycook, P. D. Nellist, and P. Nellist, *The Principles of STEM Imaging*, pp. 91–115. Springer New York, 2011.

[112] M.-W. Chu, S. C. Liou, C.-P. Chang, F.-S. Choa, and C. H. Chen, "Emergent chemical mapping at atomic-column resolution by energy-dispersive x-ray spectroscopy in an aberration-corrected electron microscope," *Phys. Rev. Lett.*, vol. 104, p. 196101, May 2010.

[113] B. Bhushan and H. Hölscher, *AFM, Tapping Mode*, pp. 99–99. Springer Netherlands, 2012.

[114] G. Binnig, C. F. Quate, and C. Gerber, "Atomic force microscope," *Phys. Rev. Lett.*, vol. 56, pp. 930–933, Mar 1986.

[115] F. Giessibl, "Advances in atomic force microscopy," *Rev. Mod. Phys.*, vol. 75, pp. 949–983, July 2003.

[116] R. W. Carpick and M. Salmeron, "Scratching the surface: Fundamental investigations of tribology with atomic force microscopy," *Chem. Rev.*, vol. 97, pp. 1163–1194, 06 1997.

[117] W. Zhang, "https://web.njit.edu/ wzhang81/,"

[118] F. M. Smits, "Measurement of sheet resistivities with the four-point probe," *Bell Syst. Tech. J.*, vol. 37, pp. 711–718, May 1958.

[119] P. Van Zant, *Microchip Fabrication, 5th Ed.* Electronic engineering, Mcgraw-hill, 2004.

[120] J. Ekin, *Experimental Techniques for Low-Temperature Measurements : Cryostat Design, Material Properties and Superconductor Critical-Current Testing: Cryostat Design, Material Properties and Superconductor Critical-Current Testing*. OUP Oxford, 2006.

[121] V. Al'tov, *Stabilization of Superconducting Magnetic Systems*. Exlog Series of Petroleum Geology and Engineering Handbooks, Springer US, 2013.

[122] M.-B. Park and N.-H. Cho, "Structural and magnetic characteristics of yttrium iron garnet (yig, ce : Yig) films prepared by {RF} magnetron sputter techniques," *J. Magn. Magn. Mater.*, vol. 231, pp. 253 – 264, Jun 2001.

[123] J. Lustikova, Y. Shiomi, Z. Qiu, T. Kikkawa, R. Iguchi, K. Uchida, and E. Saitoh, "Spin current generation from sputtered y3fe5o12 films," *J. App. Phys.*, vol. 116, Oct 2014.

[124] K.-i. Uchida, T. Kikkawa, A. Miura, J. Shiomi, and E. Saitoh, "Quantitative temperature dependence of longitudinal spin seebeck effect at high temperatures," *Phys. Rev. X*, vol. 4, p. 041023, Nov 2014.

[125] J. F. Dillon, "Ferrimagnetic resonance in rare-earth-doped yttrium iron garnet. iii. linewidth," *Phys. Rev.*, vol. 127, p. 1495, Sept 1962.

[126] A. Sposito, S. A. Gregory, P. A. J. de Groot, and R. W. Eason, "Combinatorial pulsed laser deposition of doped yttrium iron garnet films on yttrium aluminium garnet," *J. Appl. Phys.*, vol. 115, Feb 2014.

[127] L. A. Belov, S. M. Smolskiy, and V. N. Kochemasov, *Handbook of RF, Microwave, and Millimeter-wave Components*. Artech House, 2012.

[128] S. Geller, "The crystal structure and ferrimagnetism of yttrium-iron garnet, Y3Fe2(FeO4)3," *J. Phys. Chem. Solids.*, vol. 3, pp. 30–36, Jan 1957.

[129] N. Kumar, S. Prasad, D. Misra, N. Venkataramani, M. Bohra, and R. Krishnan, "The influence of substrate temperature and annealing on the properties of pulsed laser-deposited {YIG} films on fused quartz substrate," *J. Magn. Magn. Mater.*, vol. 320, pp. 2233 – 2236, Sept 2008.

[130] H. Buhay, J. Adam, M. Daniel, N. Doyle, M. Driver, G. Eldridge, M. Hanes, R. Messham, and M. Sopira, "Thick yttrium-iron-garnet (yig) films produced by pulsed laser deposition (pld) for integration applications," *IEEE Trans. Magn.*, vol. 31, pp. 3832–3834, Nov 1995.

[131] A. Block, P. Dulal, B. Stadler, and N. Seaton, "Growth parameters of fully crystallized yig, bi:yig, and ce:yig films with high faraday rotations," *IEEE Photon. J.*, vol. 6, pp. 1–8, Feb 2014.

[132] K. Enke, J.Fleischauer, W. Gunsser, P. Hansen, and S. Nomura, *Numerical Data and functional Relationships in Science and Technology*, vol. 12. Springer Berlin Heidelberg, 1978.

[133] T. Goto, M. C. Onbaşli, and C. A. Ross, "Magneto-optical properties of cerium substituted yttrium iron garnet films with reduced thermal budget for monolithic photonic integrated circuits," *Opt. Express*, vol. 20, pp. 28507–28517, Dec 2012.

[134] B. F. Stein, "Growth and some magnetic properties of gdig films," *J. App. Phys.*, vol. 42, pp. 2336–2344, July 1971.

[135] B. F. Stein, "Magnetic properties of gdig films grown by chemical vapor deposition," *J. Appl. Phys.*, vol. 41, pp. 1262–1264, Dec 1970.

[136] J. Ostorero, H. Gall, M. Guillot, and A. Barlet, "The influence of ionic migration on the magnetic properties of GdIG:Al single crystals," *IEEE Trans. Magn.*, vol. 23, pp. 1789–1794, Mar. 1987.

[137] P. B. A. Fechine, E. N. Silva, A. S. de Menezes, J. Derov, J. W. Stewart, A. J. Drehman, I. F. Vasconcelos, A. P. Ayala, L. P. Cardoso, and A. S. B. Sombra, "Synthesis, structure and vibrational properties of $GdIG_X$:YIG_{1-X} ferrimagnetic ceramic composite," *J. Phys. Chem. Solids*, vol. 70, pp. 202–209, Jan. 2009.

[138] Rambilas and D. Bahadur, "Characterization of rf-sputtered garnet films," *Bull. Mater. Sci.*, vol. 9, pp. 349–353, Nov 1987.

[139] H. L. Wang, C. H. Du, Y. Pu, R. Adur, P. C. Hammel, and F. Y. Yang, "Large spin pumping from epitaxial yig thin films to pt and w layers," *Phys. Rev. B*, vol. 88, p. 100406, Sept. 2013.

[140] Z. Qiu, K. Ando, K. Uchida, Y. Kajiwara, R. Takahashi, H. Nakayama, T. An, Y. Fujikawa, and E. Saitoh, "Spin mixing conductance at a well-controlled platinum/yttrium iron garnet interface," *Appl. Phys. Lett.*, vol. 103, August 2013.

[141] S. Vonsovskii, *Ferromagnetic Resonance: The Phenomenon of Resonant Absorption of a High-Frequency Magnetic Field in Ferromagnetic Substances*. International series of monographs on solid state physics, Elsevier Science, 2013.

[142] C. Kittel, "On the theory of ferromagnetic resonance absorption," *Phys. Rev.*, vol. 73, pp. 155–161, Jan 1948.

[143] J. H. Van Vleck, "Concerning the theory of ferromagnetic resonance absorption," *Phys. Rev.*, vol. 78, pp. 266–274, May 1950.

[144] R. C. LeCraw, E. G. Spencer, and C. S. Porter, "Ferromagnetic resonance line width in yttrium iron garnet single crystals," *Phys. Rev.*, vol. 110, pp. 1311–1313, Jun 1958.

[145] I. I. Syvorotka, I. M. Syvorotka, and S. Ubizskii, "Thick epitaxial yig films with narrow fmr linewidth," in *Oxide Materials for Electronic Engineering (OMEE), 2012 IEEE International Conference on*, pp. 264–265, Sept 2012.

[146] I. N. Leontyev, A. B. Kuriganova, N. G. Leontyev, L. Hennet, A. Rakhmatullin, N. V. Smirnova, and V. Dmitriev, "Size dependence of the lattice parameters of carbon supported platinum nanoparticles: X-ray diffraction analysis and theoretical considerations," *RSC Adv.*, vol. 4, pp. 35959–35965, August 2014.

[147] H. Hoffmann and J. Vancea, "Critical assessment of thickness-dependent conductivity of thin metal films," *Thin Solid Films*, vol. 85, pp. 147–167, Nov 1981.

[148] C. R. Tellier, A. J. Tosser, and C. Boutrit, "The mayadas-shatzkes conduction model treated as a fuchs-sondheimer model," *Thin Solid Films*, vol. 44, pp. 201–208, Jul 1977.

[149] P. Wissmann and H. Finzel, *Electrical Resistivity of Thin Metal Films*. No. no. 223 in Electrical resistivity of thin metal films, Springer, 2007.

[150] E. H. Sondheimer, "The mean free path of electrons in metals," *Adv. Phys.*, vol. 1, pp. 1–42, Jan 1952.

[151] C. R. Pichard, M. Bedda, V. I. Vatamanyuk, A. J. Tosser, and C. R. Tellier, "Alternative analytical forms of the fuchs-sondheimer function," *J. Mater. Sci.*, vol. 20, no. 11, p. 4185, 1985.

[152] J. Kondo, "Resistance minimum in dilute magnetic alloys," *Progr. Theor. Exp. Phys.*, vol. 32, pp. 37–49, Mar 1964.

[153] J. Kondo, "Effect of Ordinary Scattering on Exchange Scattering from Magnetic Impurity in Metals," *Phys. Rev.*, vol. 169, pp. 437–440, May 1968.

[154] Y. M. Lu, Y. Choi, C. M. Ortega, X. M. Cheng, J. W. Cai, S. Y. Huang, L. Sun, and C. L. Chien, "Pt magnetic polarization on yig and magnetotransport characteristics," *Phys. Rev. Lett.*, vol. 110, p. 147207, Apr 2013.

[155] V. Bogomolov, E. Kolla, and Y. Kumzerov, "One-dimensional effects in low-temperature conductivity of ultrathin metallic filaments," *Solid State Commun*, vol. 46, pp. 383 – 384, May 1983.

[156] B. Kramer and A. MacKinnon, "Localization: theory and experiment," *Rep. Prog. Phys.*, vol. 56, p. 1469, Dec 1993.

[157] S. R. Marmion, M. Ali, M. McLaren, D. A. Williams, and B. J. Hickey, "Temperature dependence of spin hall magnetoresistance in thin yig/pt films," *Phys. Rev. B*, vol. 89, p. 220404, Jun 2014.

[158] A. Pippard, *Magnetoresistance in Metals*. Cambridge Studies in Low Temperature Physics, Cambridge University Press, 1989.

[159] S. Meyer, M. Althammer, S. Geprägs, M. Opel, R. Gross, and S. T. B. Goennenwein, "Temperature dependent spin transport properties of platinum inferred from spin Hall magnetoresistance measurements," *Appl. Phys. Lett.*, vol. 104, p. 242411, June 2014.

[160] N. Vlietstra, J. Shan, B. J. van Wees, M. Isasa, F. Casanova, and J. Ben Youssef, "Simultaneous detection of the spin-hall magnetoresistance and the spin-seebeck effect in platinum and tantalum on yttrium iron garnet," *Phys. Rev. B*, vol. 90, p. 174436, Nov 2014.

[161] C. Hahn, G. de Loubens, O. Klein, M. Viret, V. V. Naletov, and J. Ben Youssef, "Comparative measurements of inverse spin hall effects and magnetoresistance in yig/pt and yig/ta," *Phys. Rev. B*, vol. 87, p. 174417, May 2013.

[162] L. Vila, T. Kimura, and Y. Otani, "Evolution of the spin hall effect in pt nanowires: Size and temperature effects," *Phys. Rev. Lett.*, vol. 99, p. 226604, Nov 2007.

[163] C. Hahn, G. de Loubens, V. V. Naletov, J. Ben Youssef, O. Klein, and M. Viret, "Conduction of spin currents through insulating antiferromagnetic oxides," *EPL*, vol. 108, p. 57005, Dec. 2014.

[164] M. Isasa, E. Villamor, L. E. Hueso, M. Gradhand, and F. Casanova, "Temperature dependence of spin diffusion length and spin hall angle in au and pt," *Phys. Rev. B*, vol. 91, p. 024402, Jan 2015.

[165] M. Obstbaum, M. Härtinger, H. G. Bauer, T. Meier, F. Swientek, C. H. Back, and G. Woltersdorf, "Inverse spin hall effect in $ni_{81}fe_{19}$/normal-metal bilayers," *Phys. Rev. B*, vol. 89, p. 060407, Feb 2014.

[166] W. Zhang, V. Vlaminck, J. E. Pearson, R. Divan, S. D. Bader, and A. Hoffmann, "Determination of the pt spin diffusion length by spin-pumping and spin hall effect," *Appl. Phys. Lett.*, vol. 103, Dec 2013.

[167] K. Ando, S. Takahashi, K. Harii, K. Sasage, J. Ieda, S. Maekawa, and E. Saitoh, "Electric manipulation of spin relaxation using the spin hall effect," *Phys. Rev. Lett.*, vol. 101, p. 036601, Jul 2008.

[168] A. Azevedo, L. H. Vilela-Leão, R. L. Rodríguez-Suárez, A. F. Lacerda Santos, and S. M. Rezende, "Spin pumping and anisotropic magnetoresistance voltages in magnetic bilayers: Theory and experiment," *Phys. Rev. B*, vol. 83, p. 144402, Apr 2011.

[169] C. T. Boone, H. T. Nembach, J. M. Shaw, and T. J. Silva, "Spin transport parameters in metallic multilayers determined by ferromagnetic resonance measurements of spin-pumping," *J. Appl. Phys.*, vol. 113, April 2013.

[170] S. H. Wang, L. K. Zou, J. W. Cai, B. G. Shen, and J. R. Sun, "Transverse thermoelectric effects in platinum strips on permalloy films," *Phys. Rev. B*, vol. 88, p. 214304, Dec 2013.

[171] K.-D. Lee, D.-J. Kim, H. Yeon Lee, S.-H. Kim, J.-H. Lee, K.-M. Lee, J.-R. Jeong, K.-S. Lee, H.-S. Song, J.-W. Sohn, S.-C. Shin, and B.-G. Park, "Thermoelectric signal enhancement by reconciling the spin seebeck and anoma-

lous nernst effects in ferromagnet/non-magnet multilayers," *Sci. Rep.*, vol. 5, p. 10249, May 2015.

[172] K. Salamon, O. Milat, N. Radić, P. Dubček, M. Jerčinović, and S. Bernstorff, "Structure and morphology of magnetron sputtered w films studied by x-ray methods," *J. Phys. D: Appl. Phys.*, vol. 46, p. 095304, Feb 2013.

[173] I. A. Weerasekera, S. I. Shah, D. V. Baxter, and K. M. Unruh, "Structure and stability of sputter deposited beta-tungsten thin films," *Appl. Phys. Lett.*, vol. 64, pp. 3231–3233, June 1994.

[174] I. Djerdj, A. Tonejc, A. Tonejc, and N. Radić, "Xrd line profile analysis of tungsten thin films," vol. 80, pp. 151 – 158, 2005.

[175] Y. Niimi, Y. Kawanishi, D. H. Wei, C. Deranlot, H. X. Yang, M. Chshiev, T. Valet, A. Fert, and Y. Otani, "Giant spin hall effect induced by skew scattering from bismuth impurities inside thin film cubi alloys," *Phys. Rev. Lett.*, vol. 109, p. 156602, Oct 2012.

[176] R. D. Fowler, B. T. Matthias, L. B. Asprey, H. H. Hill, J. D. G. Lindsay, C. E. Olsen, and R. W. White, "Superconductivity of protactinium," *Phys. Rev. Lett.*, vol. 15, p. 860, Nov 1965.

[177] E. Kaxiras, *Atomic and electronic structure of solids*. Cambridge, UK New York: Cambridge University Press, 2003.

[178] A. Lita, D. Rosenberg, S. Nam, A. Miller, D. Balzar, L. Kaatz, and R. Schwall, "Tuning of tungsten thin film superconducting transition temperature for fabrication of photon number resolving detectors," *IEEE Trans. Appl. Supercond.*, vol. 15, pp. 3528–3531, June 2005.

[179] R. T. Johnson, O. E. Vilches, J. C. Wheatley, and S. Gygax, "Superconductivity of tungsten," *Phys. Rev. Lett.*, vol. 16, p. 101, Jan 1966.

[180] Y. Sun, J. Wang, W. Zhao, M. Tian, M. Singh, and M. H. W. Chan, "Voltage-current properties of superconducting amorphous tungsten nanostrips," *Sci. Rep.*, vol. 3, p. 2307, July 2013.

[181] E. Majkova, S. Luby, M. Jergel, H. V. Löhneysen, C. Strunk, and B. George, "Superconductivity and critical fields in amorphous tungsten/silicon multilayers," *Phys. Status. Solidi. A*, vol. 145, no. 2, pp. 509–519, 1994.

[182] D. E. Beutler and N. Giordano, "Localization and electron-electron interaction effects in thin bi wires and films," *Phys. Rev. B*, vol. 38, pp. 8–19, Jul 1988.

[183] Q. Hao and G. Xiao, "Giant spin hall effect and switching induced by spin-transfer torque in a $W/co_{40}fe_{40}b_{20}/MgO$ structure with perpendicular magnetic anisotropy," *Phys. Rev. Appl.*, vol. 3, p. 034009, Mar 2015.

[184] C.-F. Pai, L. Liu, Y. Li, H. W. Tseng, D. C. Ralph, and R. A. Buhrman, "Spin transfer torque devices utilizing the giant spin Hall effect of tungsten," *Appl. Phys. Lett.*, vol. 101, p. 122404, Sept. 2012.

[185] H. L. Wang, C. H. Du, Y. Pu, R. Adur, P. C. Hammel, and F. Y. Yang, "Scaling of spin hall angle in 3d, 4d, and 5d metals from $y_3fe_5o_{12}$/metal spin pumping," *Phys. Rev. Lett.*, vol. 112, p. 197201, May 2014.

[186] D. Qu, S. Y. Huang, B. F. Miao, S. X. Huang, and C. L. Chien, "Self-consistent determination of spin hall angles in selected $5d$ metals by thermal spin injection," *Phys. Rev. B*, vol. 89, p. 140407, Apr 2014.

[187] J. Liu, T. Ohkubo, S. Mitani, K. Hono, and M. Hayashi, "Correlation between the spin Hall angle and the structural phases of early 5d transition metals," *Appl. Phys. Lett.*, vol. 107, p. 232408, Dec. 2015.

[188] A. Jayanthinarasimham, M. Medikonda, A. Matsubayashi, P. Khare, H. Chong, R. Matyi, A. Diebold, and V. Labella, "Growth of β-Tungsten Films Towards a Giant Spin Hall Effect Logic Device," in *APS*, Mar. 2015.

[189] N. Radić, A. Tonejc, J. Ivkov, P. Dubček, S. Bernstorff, and Z. Medunić, "Sputter-deposited amorphous-like tungsten," *Surf. Coat. Technol.*, vol. 180–181, pp. 66–70, Mar 2004.

[190] D. Dellasega, G. Merlo, C. Conti, C. E. Bottani, and M. Passoni, "Nanostructured and amorphous-like tungsten films grown by pulsed laser deposition," *J. Appl. Phys.*, vol. 112, October 2012.

[191] J. B. S. Mendes, R. O. Cunha, O. Alves Santos, P. R. T. Ribeiro, F. L. A. Machado, R. L. Rodríguez-Suárez, A. Azevedo, and S. M. Rezende, "Large inverse spin hall effect in the antiferromagnetic metal $ir_{20}mn_{80}$," *Phys. Rev. B*, vol. 89, p. 140406, Apr 2014.

[192] Y. Sugimoto, P. Pou, M. Abe, P. Jelinek, R. Perez, S. Morita, and O. Custance, "Chemical identification of individual surface atoms by atomic force microscopy," *Nature*, vol. 446, pp. 64–67, Mar 2007.